NASA TN D-1509

TECHNICAL NOTE

D-1509

PROPELLER SLIPSTREAM EFFECTS AS DETERMINED FROM WING PRESSURE DISTRIBUTION ON A LARGE-SCALE SIX-PROPELLER VTOL MODEL AT STATIC THRUST

By Matthew M. Winston and Robert J. Huston

Langley Research Center
Langley Station, Hampton, Va.

NATIONAL AERONAUTICS AND SPACE ADMINISTRATION
WASHINGTON

December 1962

NATIONAL AERONAUTICS AND SPACE ADMINISTRATION

TECHNICAL NOTE D-1509

PROPELLER SLIPSTREAM EFFECTS AS DETERMINED FROM WING PRESSURE DISTRIBUTION ON A LARGE-SCALE SIX-PROPELLER VTOL MODEL AT STATIC THRUST

By Matthew M. Winston and Robert J. Huston

SUMMARY

During static-thrust tests of a large-scale general research model having a tilting wing and double-slotted flaps, static-pressure measurements were made on a wing segment behind one propeller to survey the effects of the slipstream. For the conditions of highest slipstream energy, the hovering end point of aerodynamic parameters for aircraft having vertical and short take-off and landing capability (V/STOL), the effect of the slipstream on the tilt-wing configuration (zero flap deflection) was a 6° spanwise variation in effective angle of attack in a span of slightly less than 1 propeller diameter. Effective changes in camber on the tilt-wing configuration as a result of slipstream rotation, the radial velocity gradient, and the resultant spanwise flow were negative and had a maximum magnitude of less than 2-percent chord. For the deflected-slipstream configuration (double-slotted flaps deflected), effects important to the hovering performance were found, including a 40-percent spanwise variation in effective thrust recovery and a 20° spanwise variation in effective thrust turning.

INTRODUCTION

Propeller slipstreams have been studied throughout the history of aviation, and the problems associated with the slipstream for conventional aircraft have been adequately defined and/or solved. (For example, see ref. 1.) The evolution of the VTOL aircraft, however, has introduced a broader range of parameters than had previously been investigated for conventional aircraft. One change has been to extend the free-stream velocity range to zero, where, unlike a hovering helicopter rotor, the VTOL propeller produces a slipstream of relatively high energy. A number of theoretical studies have been made on the effects of a high-energy slipstream at low forward speeds (for example, see refs. 2, 3, 4, and 5), and some limited experimental results have been obtained at low forward speeds (refs. 3, 5, and 6). Missing from these results is a sample of the propeller-slipstream effects at zero forward speed. Such a sample is important as an end point in the aerodynamic parameters for VTOL aircraft, where the effects of the

high-energy slipstream are at a maximum, and for determining the significance of the effects of the slipstream on hovering characteristics.

During studies with a large-scale V/STOL model at static thrust (ref. 7), measurements of the chordwise and spanwise pressure distribution were made on a wing segment behind one propeller. This paper presents a sample of these results and an analysis of the effect of the slipstream on the force distribution. The local flow effects due to the slipstream are considered herein to result in a spanwise variation in angle of attack and camber. For a highly flapped wing, the local slipstream effects can also be considered as a lateral variation in the thrust-recovery factor. No attempt was made to determine the entire spanwise force distribution including wing-tip and fuselage effects. However, the data presented are adequate as a sample of the general nature of the effects of the slipstream on a wing at static thrust.

COEFFICIENTS AND SYMBOLS

The force and moment conventions employed are shown in figure 1.

b propeller-blade chord, ft

C wing chord forces, including thrust, lb

C_m wing-pitching-moment coefficient about wing quarter chord, $\frac{\text{Pitching moment}}{qSc}$

c wing chord, ft unless otherwise noted

c_c vector summation of section-chord-force coefficients for wing and flap, resolved parallel to basic-wing-chord plane

$c_{c,w}, c_{c,f}$ section-chord-force coefficients for wing and flap, respectively, $\int_{(t/c)_{min}}^{(t/c)_{max}} \frac{\Delta P_b - \Delta P_a}{q_s} d\frac{t}{c}$

c_m section-pitching-moment coefficient about wing quarter chord, $\int_{(x/c)_{min}}^{(x/c)_{max}} \frac{\Delta P_l - \Delta P_u}{q_s}\left(0.25 - \frac{x}{c}\right)d\frac{x}{c} - \int_{(t/c)_{min}}^{(t/c)_{max}} \frac{\Delta P_b - \Delta P_a}{q_s}\left(\frac{t}{c}\right)d\frac{t}{c}$

c_n vector summation of section-normal-force coefficients for wing and flap, resolved normal to basic-wing-chord plane

$c_{n,w}, c_{n,f}$ section-normal-force coefficients for wing and flap, respectively, $\int_{(x/c)_{min}}^{(x/c)_{max}} \frac{\Delta P_l - \Delta P_u}{q_s} d\frac{x}{c}$

D	propeller diameter, ft
F	resultant force, $\sqrt{C^2 + N^2}$, lb
h	propeller-blade thickness, ft
i_w	wing incidence angle, angle between wing chord line and ground, deg
N	wing normal forces
ΔP	static-differential pressure, $p - p_a$, lb/sq ft
p	local static pressure, lb/sq ft
p_a	atmospheric pressure, lb/sq ft
q	free-stream dynamic pressure, $\frac{\rho V^2}{2}$, lb/sq ft
q_s	slipstream dynamic pressure, $q + \frac{T}{6\pi R^2}$, lb/sq ft
R	radius to propeller tip, ft
r	radius to any propeller-blade section, ft
S	wing area, sq ft
T	total propeller thrust, including body drag (longitudinal force with wing and flaps undeflected), lb
t	perpendicular distance from undeflected-wing chord line to any point on wing or flap surface, positive upward, ft
V	free-stream velocity, ft/sec
x	any distance from wing leading edge parallel to chord line of undeflected wing, ft
y	any distance from center of rotation of propeller along wing span, positive in region of upward slipstream flow, ft
z	distance from ground to wing pivot, ft
α	free-stream angle of attack measured from wing chord line, deg
δ_f	flap deflection, deg
θ	thrust turning angle, inclination of resultant-force vector from propeller-thrust axis

ρ mass density of air, slugs/cu ft

Subscripts:

a ahead of airfoil maximum ordinates

b aft of airfoil maximum ordinates

l airfoil lower surface

max maximum

min minimum

u airfoil upper surface

30 30-percent-chord flap

55 55-percent-chord flap

MODEL, TESTS, AND METHODS

Basic dimensions of the model are shown in figure 2, and photographs of the model are shown in figure 3. Locations of the pressure orifices are given in figure 4. The wing has a rectangular planform, a span of 35 feet, a chord length of 4.375 feet, and an NACA 63_2A215 airfoil section. A pivot at the 35-percent-chord station permits rotation of the wing to incidence angles from 0° to 90°. The wing is equipped with double-slotted flaps (55- and 30-percent wing chord) which are manually adjustable in 10° increments. The propellers have four solid aluminum blades with manually adjustable pitch. Propeller diameter is 5 feet, and the blade pitch at the 0.75 radius was set at 16.3° for all tests. Propeller-blade-form curves are presented in figure 5. The right center propeller, behind which the orifices are located, rotates clockwise as viewed from the front. (See fig. 2.) A more detailed description of the model and static-thrust test program is given in reference 7.

Pressure distributions for the wing without propellers were obtained from measurements in the Langley full-scale tunnel at a dynamic pressure of approximately 16 lb/sq ft and at a Reynolds number based on wing chord of 3.22×10^6. Wing geometry was the same as for the static tests of reference 7.

In both static and wind-tunnel tests, pressures were indicated on a fluid manometer and were photographically recorded. The data from these records were reduced to pressure coefficients which, in turn, were plotted and integrated to obtain force and moment coefficients.

PRESENTATION OF DATA

Wing-pressure-distribution data for a propeller disk loading of 29.7 lb/sq ft, which were tabulated in reference 7, are shown in figures 6 to 21. In these figures, the ratio of static pressure to slipstream dynamic pressure is plotted against the airfoil chord and thickness to obtain the normal- and chord-force distributions, respectively. The arrows in the center sketch of these figures indicate the row of orifices from which a given distribution was obtained. Pressure distributions for the wing without propellers (full-scale-tunnel tests) are presented in figure 22 for a range of angles of attack. Pressure distributions from the data with propellers off were plotted for four spanwise stations but, since close agreement of integrated forces and moments between stations was indicated, only the pressure distributions of a representative station are presented. Due to uncertainties in the region of the nacelle, portions of the curves in figures 23(b) to 28 are shown by dashed lines.

The results of this investigation are presented in the following figures:

	Figure
Pressure distributions in slipstream flow	6 to 21
Pressure distributions in uniform flow	22
Section-normal-force and moment variations for wing	23
Spanwise force variations with flaps neutral	24, 25
Spanwise force variations with varying i_w and $\delta_{f,55}$. $\delta_{f,30} = 38.6^\circ$	26
Summary of turning effectiveness of wing section behind propeller	27 to 29

DISCUSSION

Effective Angle of Attack and Camber

In order to obtain a measure of the relative magnitudes of the slipstream effects on the effective angle of attack and camber, the pressure characteristics of the wing (propellers removed) obtained from unpublished wind-tunnel pressure data (fig. 22) were compared with the pressure characteristics obtained in the slipstream from the present test. The method of analysis applied to the data is included in appendix A. The analysis does not account for the effects of the nacelles; however, a qualitative idea of how the nacelle affects the spanwise loading may be obtained from reference 8.

Results from the wind-tunnel tests are shown in figure 23(a) as the variation of c_n and c_m with α for the wing without propellers. The pitching-moment values measured with a strain-gage beam are included with the integrated pressure data to indicate the agreement obtained from the two different measurement methods. The spanwise variation of c_n and c_m behind the propeller in the slipstream for

a comparable wing configuration at static thrust is given in figure 23(b). Data for wing incidence angles of 0° and 90° are included to show the small effect of large variations in wing attitude on the force and moments for the tilt-wing configuration. From the appended method of analysis and the data included in figure 23, the effective angles of attack and effective camber changes have been calculated for four spanwise wing sections. The results of these calculations are summarized in the following table: .

Basic tilt wing $(\delta_{f,55}$ and $\delta_{f,30} = 0^\circ)$		
$\frac{y}{R}$	Effective angle of attack, deg	Effective camber change, percent chord
-0.867	-3.2	-1.3
-.267	-3.4	-.3
.267	.6	-1.5
.750	2.8	-1.8

The results given in the preceding table indicate the relative magnitudes and nature of the slipstream effects on the wing of the test model. The effective angle-of-attack variation was about 6° in a span of slightly less than 1 propeller diameter, and the camber change was negative at every spanwise station. It should be noted that the effective changes in camber as a result of slipstream rotation, the radial velocity gradient, and the resultant spanwise flow were of the order of magnitude of the geometric camber (1.5 percent). (Note also p. 28 of ref. 9.) This is in contrast to the results of reference 6, wherein the maximum spanwise variation in effective camber is of the same order of magnitude as in this test but varies from positive increments on wing sections behind the upgoing blade to negative increments on the wing section behind the downgoing blade. It is believed that the difference in effect of slipstream on effective camber in this investigation and in reference 6 is primarily due to the vertical position of the propeller with respect to the wing. In reference 6, the propeller was installed on the wing chord line in contrast to the below-the-wing propeller center line of the present investigation.

The magnitudes of the slipstream effects are also believed to depend upon several other factors such as propeller-blade pitch, longitudinal propeller location, mode of propeller rotation, lateral spacing of propellers, and other design changes that are sometimes associated with changes in disk loading. The present results, however, are believed adequate to show that the order of magnitude of the effective camber changes is small compared to the effect of flap deflection. Similarly, the present results are believed to provide a basis for judging the order of magnitude of effective angle-of-attack variation which must be dealt with in VTOL designs of this general class.

Thrust Recovery and Turning

Tilt-wing configuration.- The spanwise-force distributions on the wing behind the propeller for four different wing attitudes and with flaps neutral are given in figure 24. The wing incidence angle had only a small effect on the magnitude and distribution of forces at the upper ground height ($z/D = 2.4$), and, for the conditions investigated, only at a wing incidence angle of 0° was there an appreciable difference in magnitude at the lower ground height ($z/D = 1.0$). This difference was due to ground proximity effects, which are further illustrated in figure 25.

The data of figure 24 are repeated in figure 25 to show the effect of ground proximity for the four wing attitudes. For wing incidence angles of 56°, 75°, and 90°, favorable ground effect was observed. At a wing incidence angle of 0°, however, the effect of ground proximity was detrimental. Reference to the pressure distributions of figures 6 and 14 reveals that this result is primarily due to more negative pressure coefficients on the lower wing surface at the lower ground height than for the upper height; the result was a "suck down" effect similar to the effect observed for the jet and buried-fan configurations of reference 10.

Deflected-slipstream configurations.- Spanwise force distributions for several flapped configurations having vertical take-off and landing capability, that is, vertical resultant force, are given in figure 26. The results shown indicate larger forces at the upper ground height than at the lower ground height. In addition, greater decreases in wing incidence angles were afforded by a given increment in flap deflection while a vertical resultant was maintained. These results are indicative of increased flap effectiveness at model positions away from the ground.

Evaluation of deflected-slipstream configurations in hovering is made principally through comparisons of thrust recovery and thrust turning angles. Because thrust recovery factor F/T and thrust turning angle θ are normally and more conveniently obtained from force measurements, as in reference 7, it was necessary to devise a method of obtaining comparable results from pressure data. The development of this method is covered in appendix B.

Figure 27 gives the turning effectiveness of wing sections behind the propeller. Spanwise variations in effective thrust recovery and effective turning were the result of slipstream flow at both model heights above the ground. At the upper ground height, there was approximately a 40-percent variation in effective thrust recovery over the span segment behind the propeller. A variation of 20° in effective thrust turning angle occurred simultaneously. These values were about twice as large as the variations at the lower height; the difference is due partially to losses in flap effectiveness because of changes in the flow near the ground. These large changes in thrust recovery and turning with ground height may be the source of unstable moments for a VTOL aircraft that is upset in roll while hovering near the ground.

The spanwise variations in thrust recovery and turning, due to spanwise angle-of-attack variations, agree with the results of references 11 and 12, wherein results indicated that increased turning was obtained by lowering the thrust axis below the wing-chord plane. A wing design utilizing a leading-edge slat with spanwise variable incidence to give a more uniform load distribution and with an optimum thrust-axis angle may more fully realize the potential of the deflected-slipstream VTOL aircraft than have previous designs.

Figure 28 gives a comparison of the turning effectiveness of the wing segment, based on its mean loading, to the turning effectiveness of the entire model. Good agreement between pressure and force data was obtained for the upper model position considering the unknown effects of the wing tips and fuselage. The differences at the lower height are believed to be due to the separation of ground effect into two components for a hovering VTOL aircraft. The first component, a favorable ground effect on propeller thrust, resulted in an apparent increase in thrust recovery. (See definition of propeller thrust in the section entitled "Symbols.") The second component, an unfavorable ground effect on wing pressures, resulted in decreased turning angles.

The effects of wing attitude and ground proximity on turning effectiveness for a deflected-slipstream configuration having constant 55- and 30-percent-chord flap deflection are shown in figure 29. These effects are generally the same as those previously discussed for the unflapped wing in figures 24 and 25.

CONCLUSIONS

An analysis has been made of static-pressure measurements on the wing and flaps of a vertical take-off and landing model to determine the effect of the propeller slipstream on the load distribution at zero free-stream velocity. The results are as follows:

1. For a tilt-wing airplane configuration (zero flap deflection) in a hovering position, the spanwise variation in effective angle of attack for wing sections in the slipstream was about 6° in a span of slightly less than 1 propeller diameter. Effective changes in camber as a result of slipstream rotation, the radial velocity gradient, and the resultant spanwise flow were negative and had a maximum magnitude of less than 2-percent chord.

2. For a deflected-slipstream configuration at static thrust, the slipstream caused a 40-percent spanwise variation in effective thrust recovery and a 20° spanwise variation in effective thrust turning, with the model at the greatest height from the ground. A substantial variation in turning was also obtained at the low ground position, but the spanwise variation in effective thrust recovery was only about half of that found for the upper height.

3. For the deflected-slipstream configuration, hovering in the presence of the ground resulted in increased effective thrust recovery due to a favorable

ground effect on propeller thrust and decreased effective thrust turning due to a lowering of wing and flap pressure forces near the ground.

Langley Research Center,
National Aeronautics and Space Administration,
Langley Station, Hampton, Va., August 29, 1962.

APPENDIX A

EFFECTIVE ANGLE OF ATTACK AND CAMBER

With the use of cambered airfoil theory (see ref. 13, pp. 97 and 98), the quarter-chord pitching moment c_m and the angle of zero lift $\alpha_{o,s}$ can be found if the airfoil camber is specified. Conversely, to obtain the magnitude of the slipstream induced effects from a measured quarter-chord pitching moment, the effective airfoil-section camber and angle of zero lift can be determined from

$$c_m = -\pi\frac{f}{c} \tag{A1}$$

and

$$\alpha_{o,s} = -2\frac{f}{c} \tag{A2}$$

where f is the height of camber, c is the airfoil chord, and $\alpha_{o,s}$ is in radians. If it is assumed that the variation of airfoil normal force with angle of attack (measured from the zero-lift angle) has the same slope for a wing section in nonuniform slipstream flow as in uniform flow, the following relationship can be written for a constant normal-force coefficient:

$$\alpha - \alpha_o = \alpha_e - \alpha_{o,s} \tag{A3}$$

where α is the free-stream angle of attack measured from the wing chord line; α_o is the angle of zero lift of the airfoil section in free-stream flow measured from α; α_e is the effective angle of attack of the airfoil section in slipstream flow measured from $\alpha_{o,s}$; and $\alpha_{o,s}$ is the angle of zero lift in the slipstream flow. With the variation of c_n with α and the value of α_o known from wind-tunnel tests, the effective camber and effective angle of attack in slipstream flow are obtainable from equations (A1), (A2), and (A3). It should be noted as shown in reference 5 that the airfoil lift-curve slope is affected by the vertical position of the wing in a two-dimensional slipstream; however, any change in the slope of the normal-force curve will be reflected in the effective angle of attack.

APPENDIX B

EFFECTIVE-THRUST-RECOVERY FACTOR

An effective-thrust-recovery factor can be obtained by dividing the vector sum of the resultant section pressure force and the mean thrust per unit propeller diameter by the mean thrust per unit propeller diameter. The normal- and chord-force components of this effective-thrust-recovery factor may be expressed as

$$\text{Normal loading per unit thrust loading} = \frac{c_n q_s c}{T/6D} \tag{B1}$$

$$\text{Chord loading per unit thrust loading} = \frac{\frac{T}{6D} + c_c q_s c}{T/6D} \tag{B2}$$

Equations (B1) and (B2) may be simplified to

$$\text{Normal loading per unit thrust loading} = \frac{Dc}{\pi R^2} c_n \tag{B3}$$

$$\text{Chord loading per unit thrust loading} = 1 + \frac{Dc}{\pi R^2} c_c \tag{B4}$$

If it is assumed that the mean resultant pressure force is typical of the load on the wing behind all six propellers (ignoring wing-tip and fuselage effects), the ratios of normal force to thrust and chord force to thrust can be expressed as

$$\frac{N}{T} = \frac{Dc}{\pi R^2} \left(\frac{\int_{y/R=-0.867}^{y/R=0.750} c_n \, d\frac{y}{R}}{\int_{y/R=-0.867}^{y/r=0.750} d\frac{y}{R}} \right) \tag{B5}$$

and

$$\frac{C}{T} = 1 + \frac{Dc}{\pi R^2} \left(\frac{\int_{y/R=-0.867}^{y/R=0.750} c_c \, d\frac{y}{R}}{\int_{y/R=-0.867}^{y/R=0.750} d\frac{y}{R}} \right) \tag{B6}$$

The effective-thrust-recovery factor can be obtained from equations (B5) and (B6) and expressed as

$$\frac{F}{T} = \sqrt{\left(\frac{C}{T}\right)^2 + \left(\frac{N}{T}\right)^2} \tag{B7}$$

REFERENCES

1. Koning, C.: Influence of the Propeller on Other Parts of the Airplane Structure. Vol. IV of Aerodynamic Theory, div. M, W. F. Durand, ed., Julius Springer (Berlin), 1935, pp. 361-430.

2. Rethorst, Scott, Royce, Winston, and Wu, T. Yao-tsu: Lift Characteristics of Wings Extending Through Propeller Slipstreams. Rep. No. 1 (Contract No. Nonr 2388(00)), Vehicle Res. Corp. (Pasadena, Calif.), Sept. 1958.

3. Snedeker, Richard S.: Experimental Determination of Spanwise Lift Effects on a Wing of Infinite Aspect Ratio Spanning a Circular Jet. Rep. No. 525 (Contracts Nonr 1858(14) and Nonr 1858(01)), Dept. Aero. Eng., Princeton Univ., Feb. 1961.

4. Kirby, Robert H.: Aerodynamic Characteristics of Propeller-Driven VTOL Aircraft. NASA TN D-730, 1961.

5. Vidal, R. J.: The Influence of Two-Dimensional Stream Shear on Airfoil Maximum Lift. Paper No. 61-120-1814, Inst. Aerospace Sci., June 1961.

6. Currie, M. M., and Dunsby, J. A.: Pressure Distribution and Force Measurements on a VTOL Tilting Wing-Propeller Model - Part II: Analysis of Results. Rep. LR-284 (N.R.C. No. 5918), Nat. Res. Council of Canada (Ottawa), June 1960.

7. Huston, Robert J., and Winston, Matthew M.: Data from a Static-Thrust Investigation of a Large-Scale General Research VTOL-STOL Model in Ground Effect. NASA TN D-397, 1960.

8. Robinson, Russell G., and Herrnstein, William H., Jr.: Wing-Nacelle-Propeller Interference for Wings of Various Spans. Force and Pressure-Distribution Tests. NACA Rep. 569, 1936.

9. Abbott, Ira H., and Von Doenhoff, Albert E.: Theory of Wing Sections. McGraw-Hill Book Co., Inc., 1949.

10. Spreemann, Kenneth P.: Induced Interference Effects on Jet and Buried-Fan VTOL Configurations in Transition. NASA TN D-731, 1961.

11. Kuhn, Richard E.: Investigation of the Effects of Ground Proximity and Propeller Position on the Effectiveness of a Wing With Large-Chord Slotted Flaps in Redirecting Propeller Slipstreams Downward for Vertical Take-Off. NACA TN 3629, 1956.

12. Kuhn, Richard E., and Draper, John W.: Investigation of Effectiveness of Large-Chord Slotted Flaps in Deflecting Propeller Slipstreams Downward for Vertical Take-Off and Low-Speed Flight. NACA TN 3364, 1955.

13. Pope, Alan: Basic Wing and Airfoil Theory. McGraw-Hill Book Co., Inc., 1951.

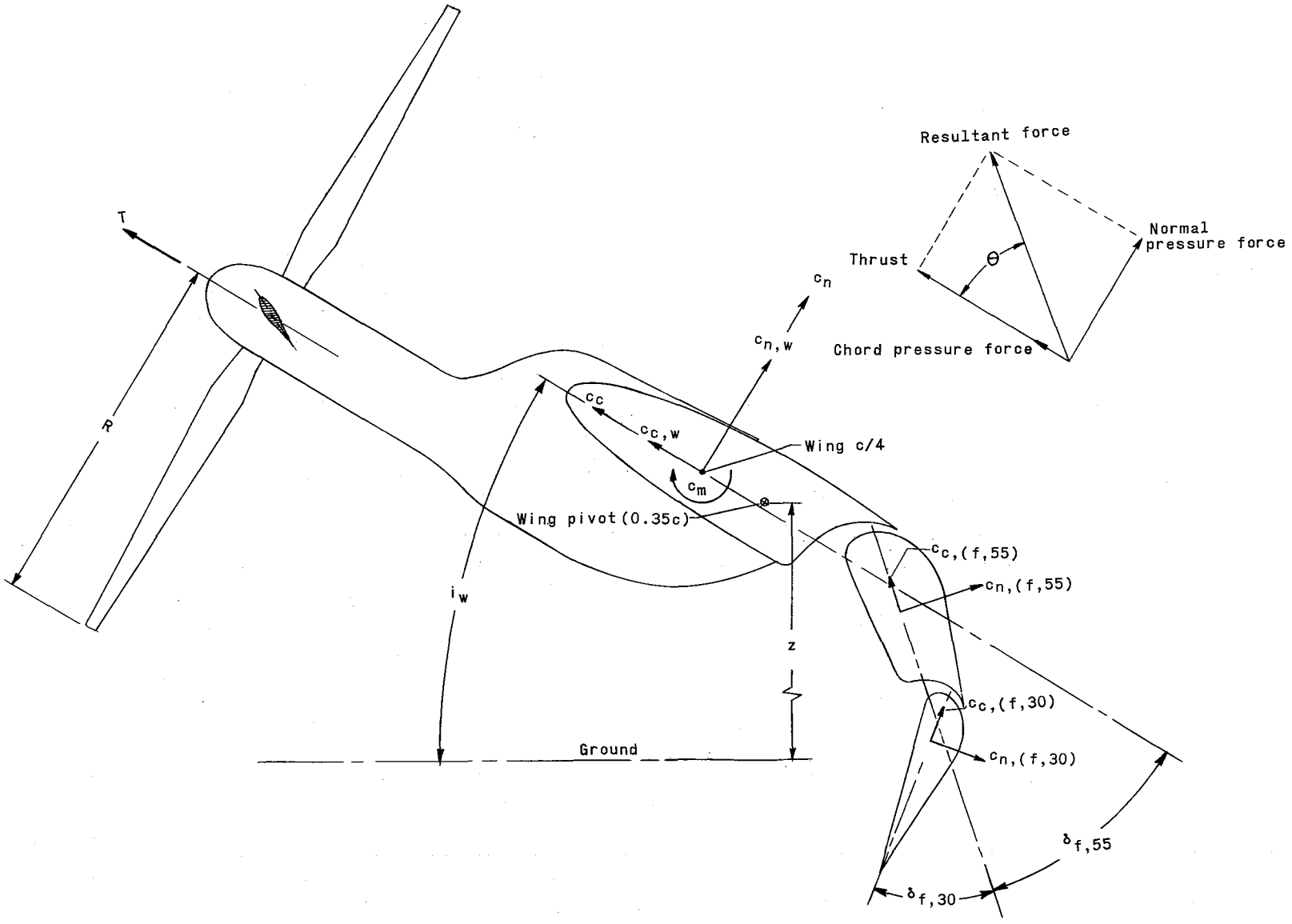

(a) Forces, moments, and angles.

Figure 1.- Conventions used to define positive senses of forces, moments, angles, and pressure.

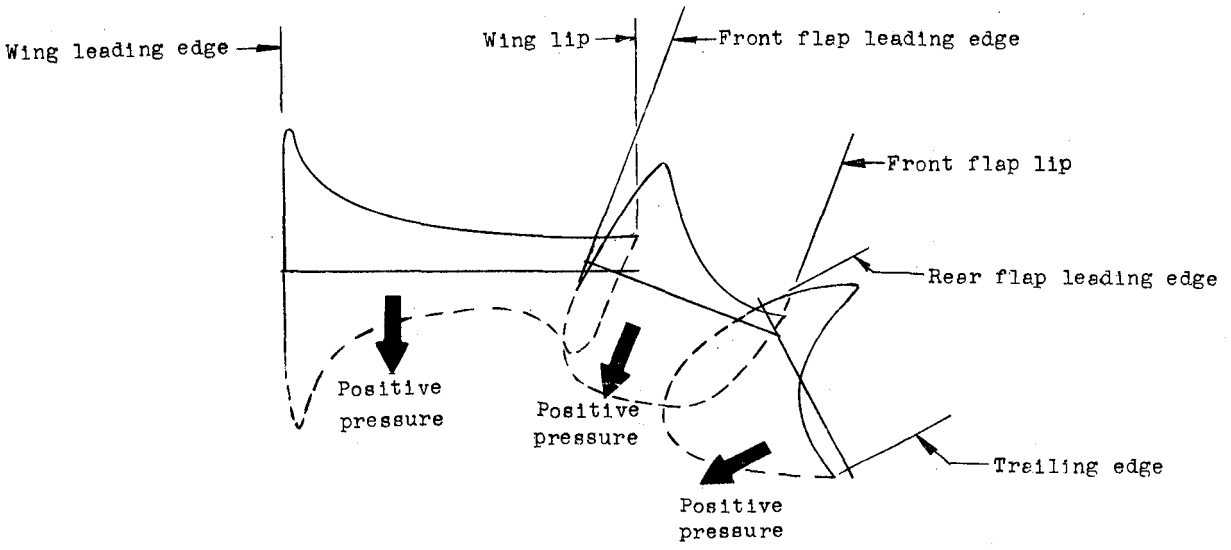

Normal pressure distribution

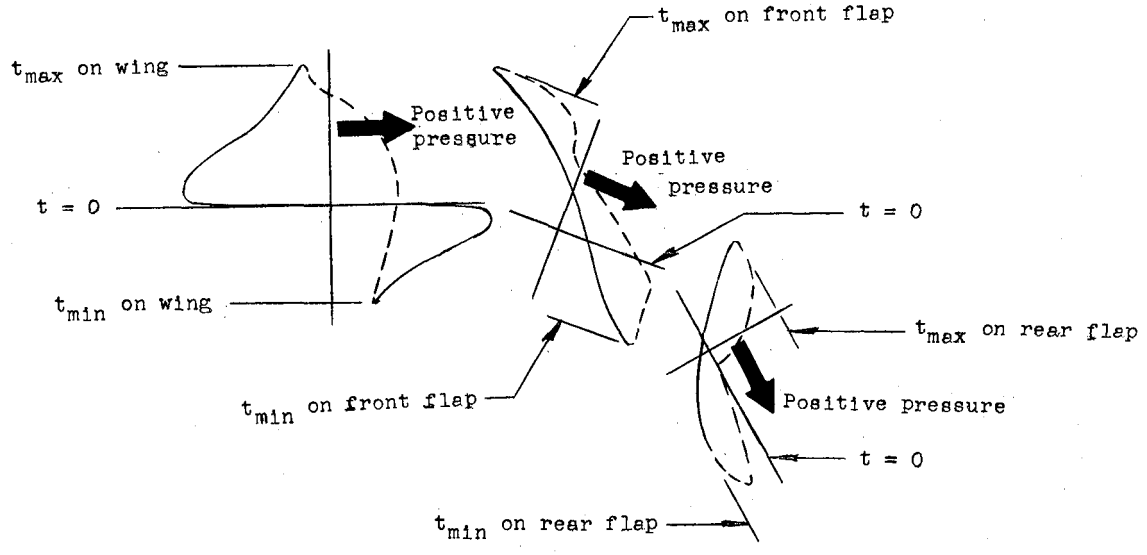

Chord pressure distribution

(b) Chordwise-pressure-distribution plots.

Figure 1.- Concluded.

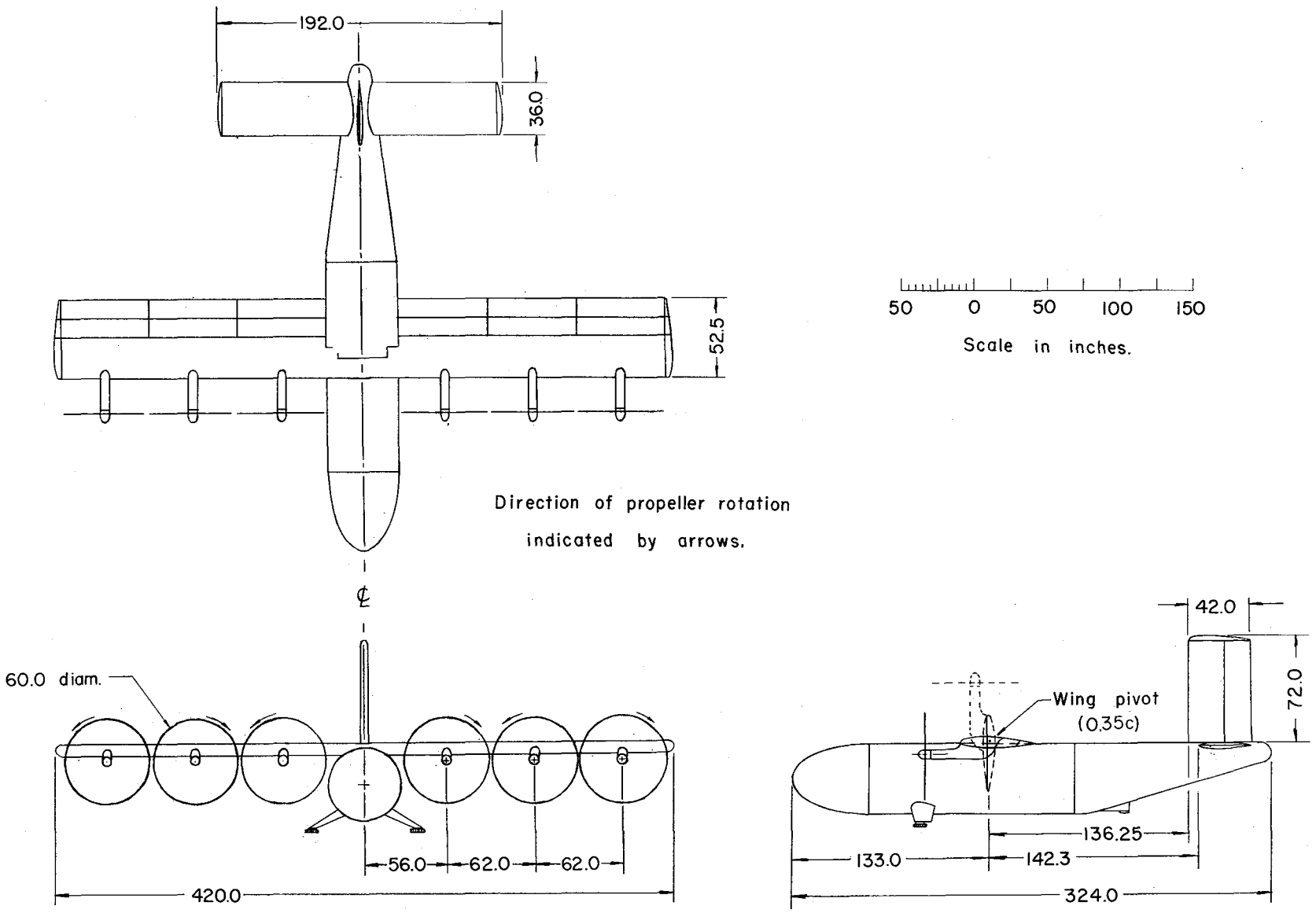

Figure 2.- Three-view sketch of model. All dimensions are in inches.

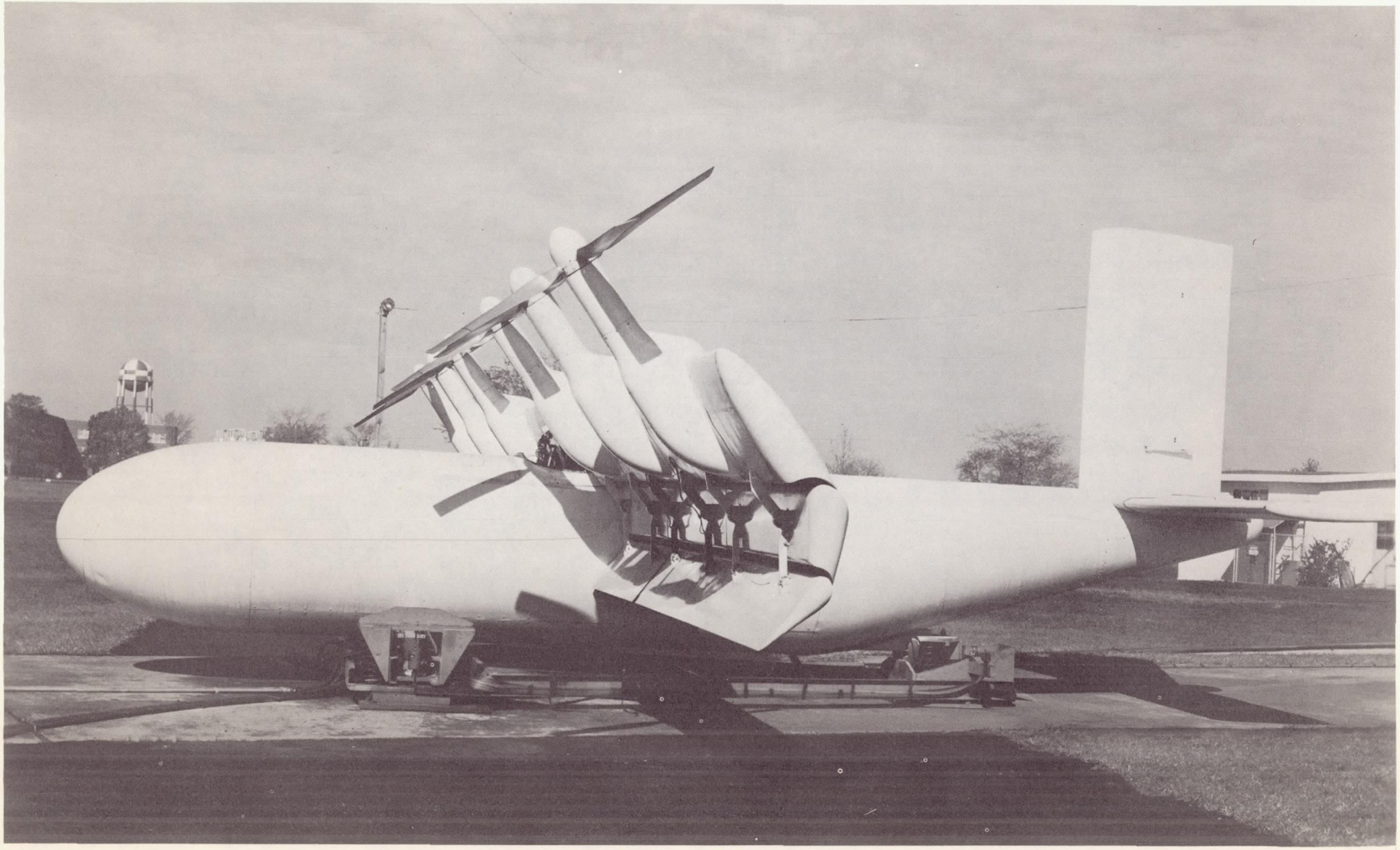

(a) Deflected-slipstream configuration. z/D = 1.0. L-59-7989

Figure 3.- Photographs of model on test stand.

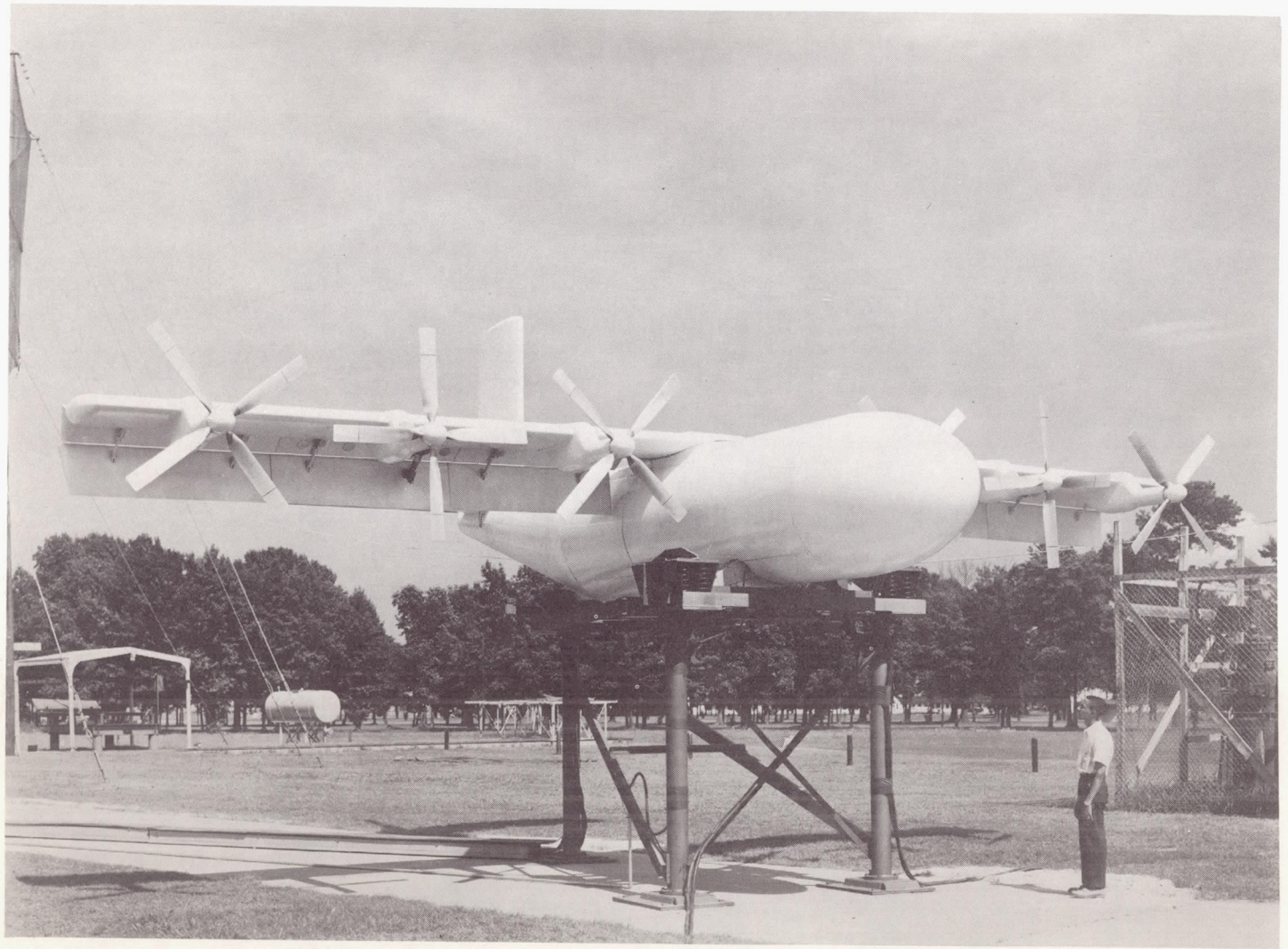

(b) Configuration with wing in horizontal position. z/D = 2.4. L-59-4897

Figure 3.- Continued.

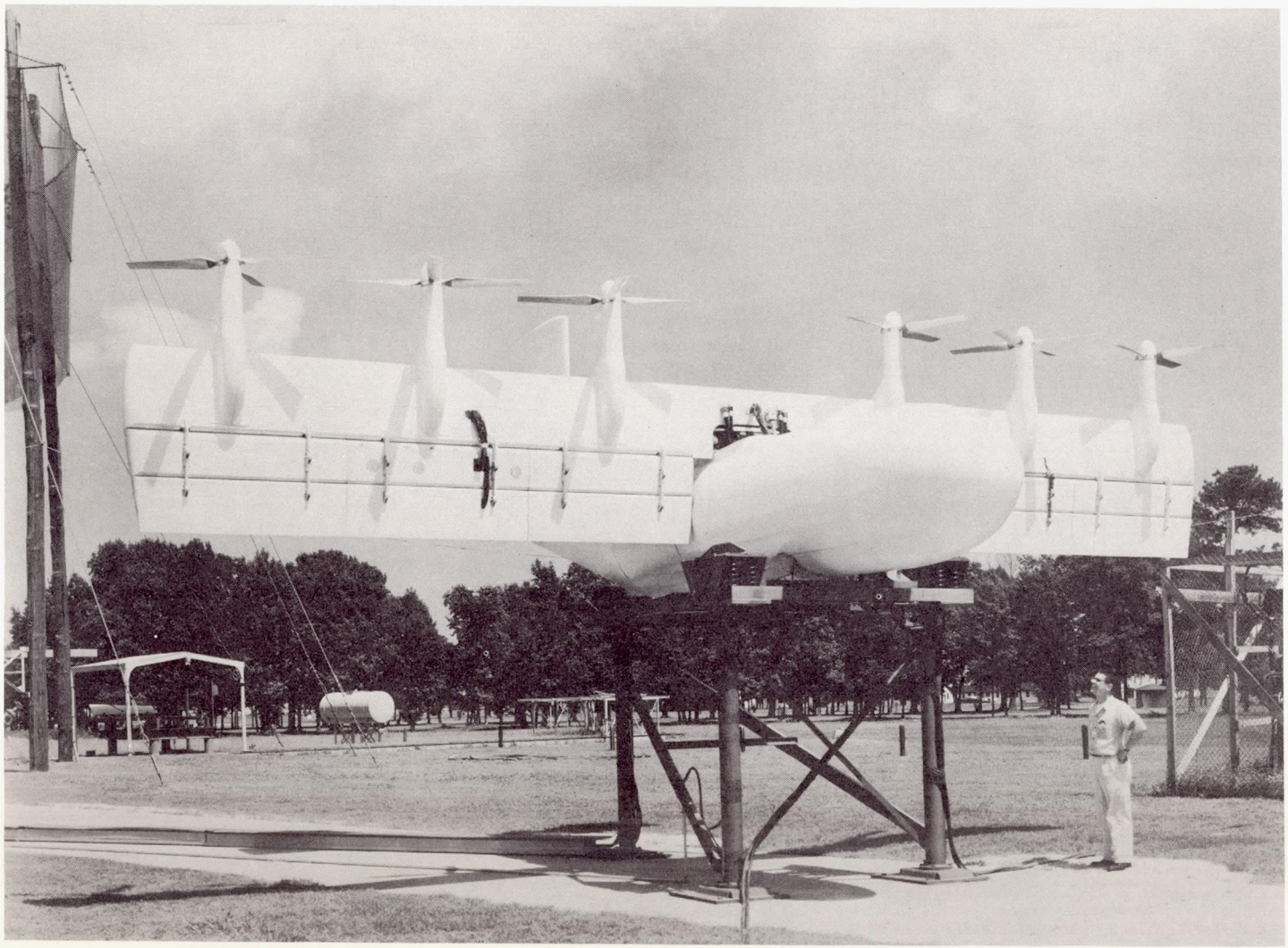

(c) Configuration with wing in vertical position. z/D = 2.4. L-59-4896

Figure 3.- Concluded.

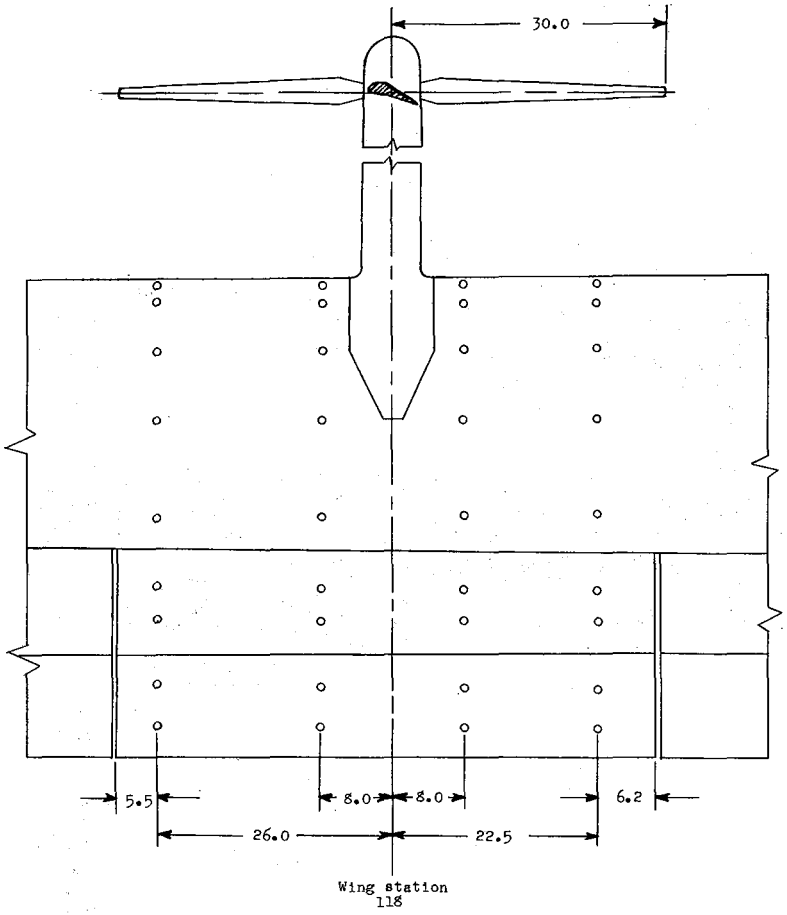

Orifice Locations		
Tube	Station, percent chord	Ordinate, percent chord
1	0	0
2	1.5	2.23
3	5.0	3.96
4	15.0	6.76
5	30.0	8.53
6	50.0	8.19
7	1.5	-1.77
8	5.0	-3.18
9	15.0	-5.14
10	30.0	-6.25
11	45.0	-2.59
12	46.6	1.75
13	50.0	5.41
14	45.0	-2.03
15	50.0	5.26
16	55.0	7.33
17	65.0	6.42
18	71.5	5.41
19	48.3	-5.52
20	55.0	-5.05
21	65.0	-3.92
22	69.9	-0.90
23	73.4	2.50
24	70.0	-0.95
25	72.6	3.26
26	76.5	4.48
27	84.9	3.01
28	93.3	1.37
29	78.5	-2.19
30	89.5	-1.07

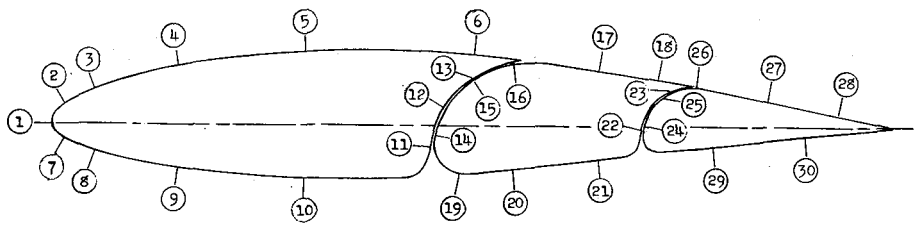

Figure 4.- Locations of pressure orifices on wing and flaps. All dimensions are in inches.

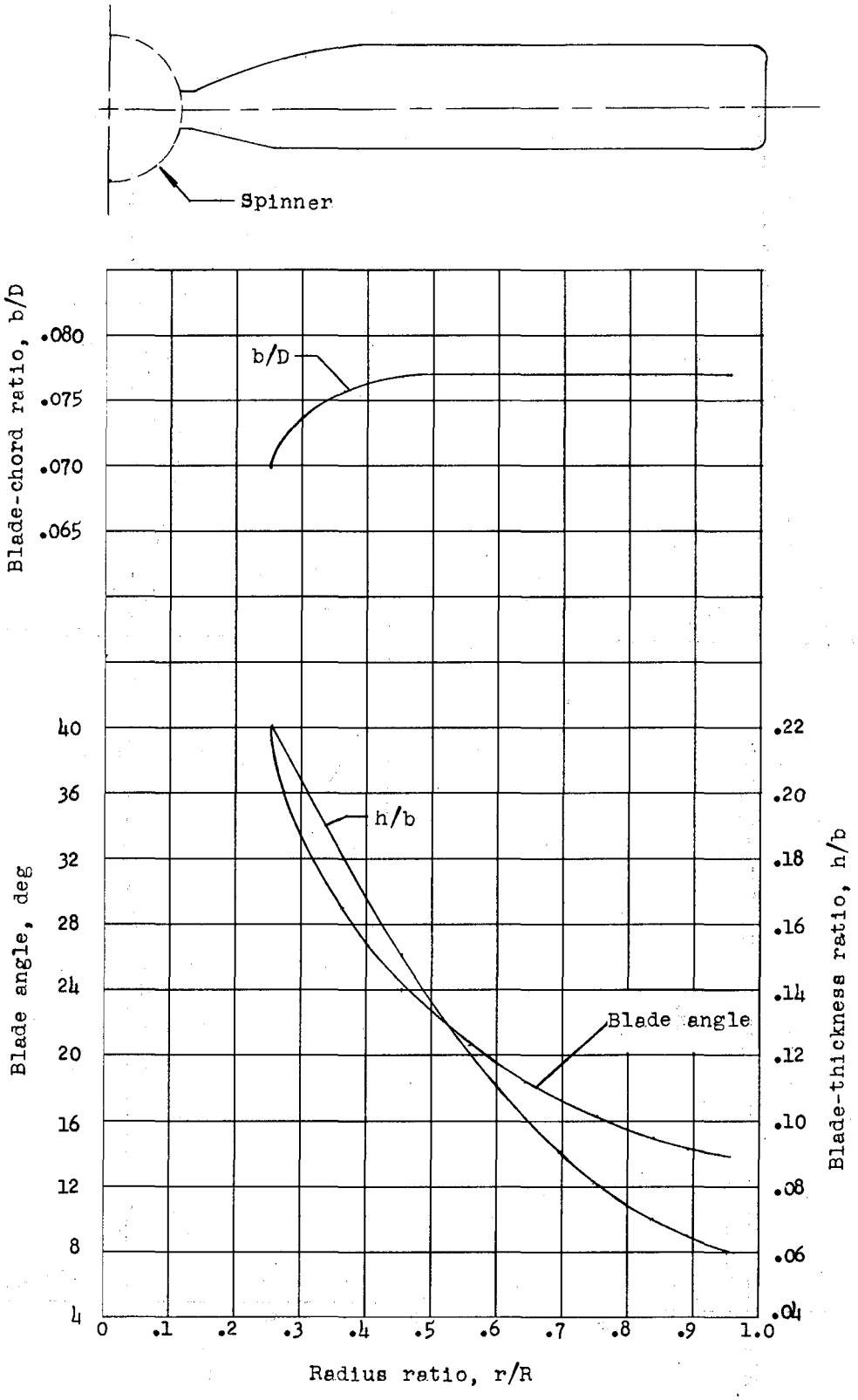

Figure 5.- Propeller-blade-form curves.

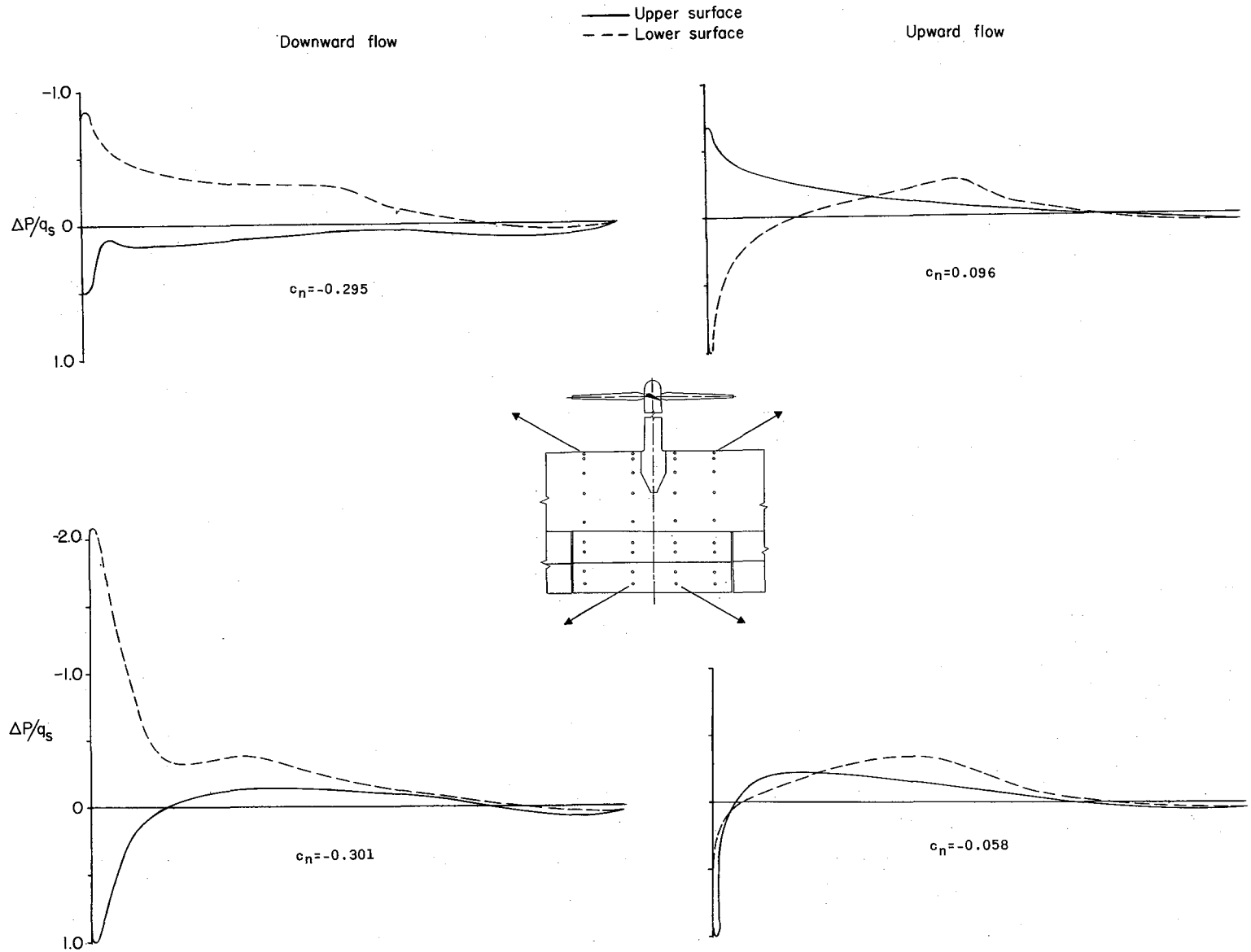

(a) Normal pressure distributions over airfoil length.

Figure 6.- Pressure distributions on wing with flaps neutral. $i_w = 0^o$; $z/D = 1.0$.

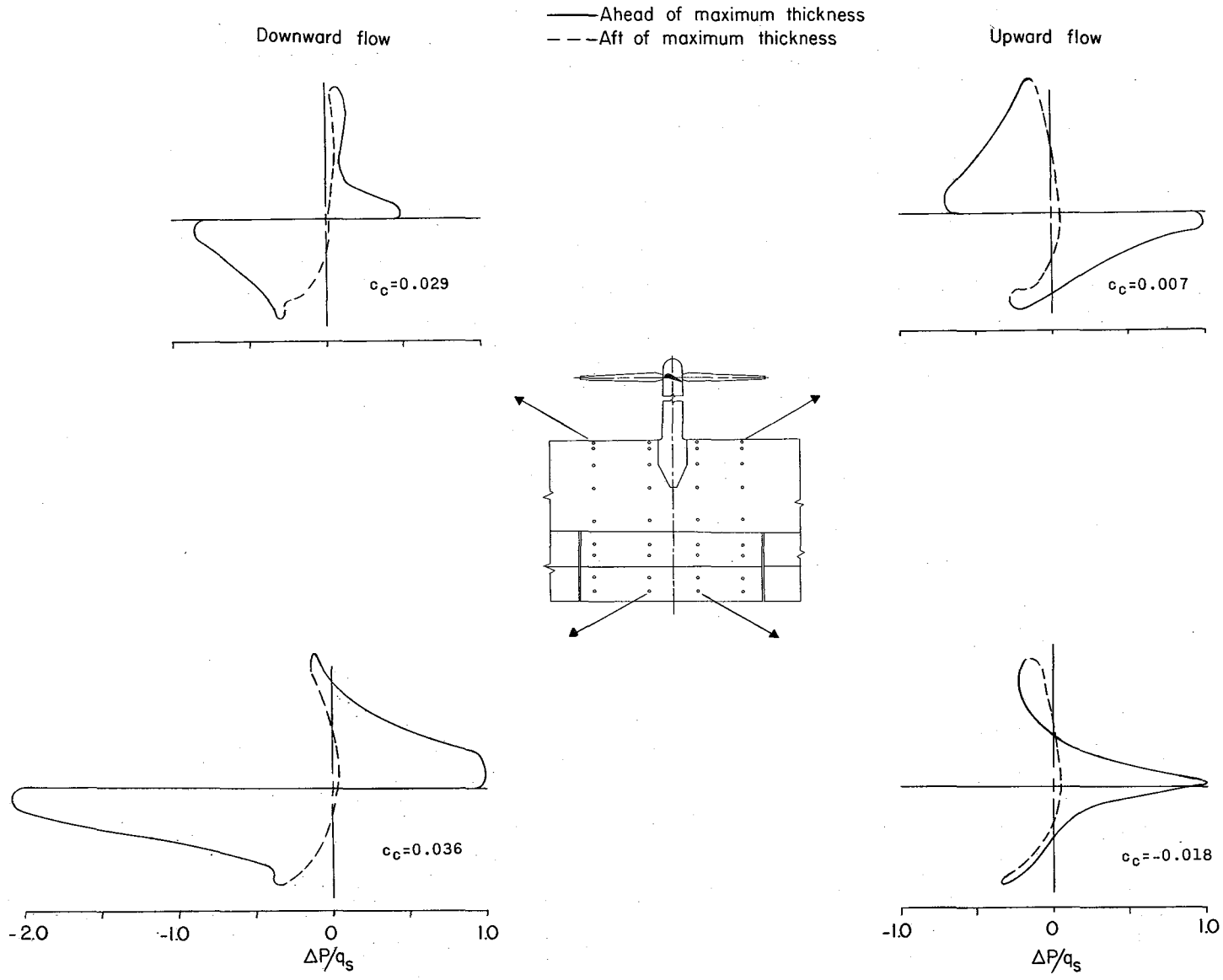

(b) Chord pressure distributions over airfoil thickness.

Figure 6.- Concluded.

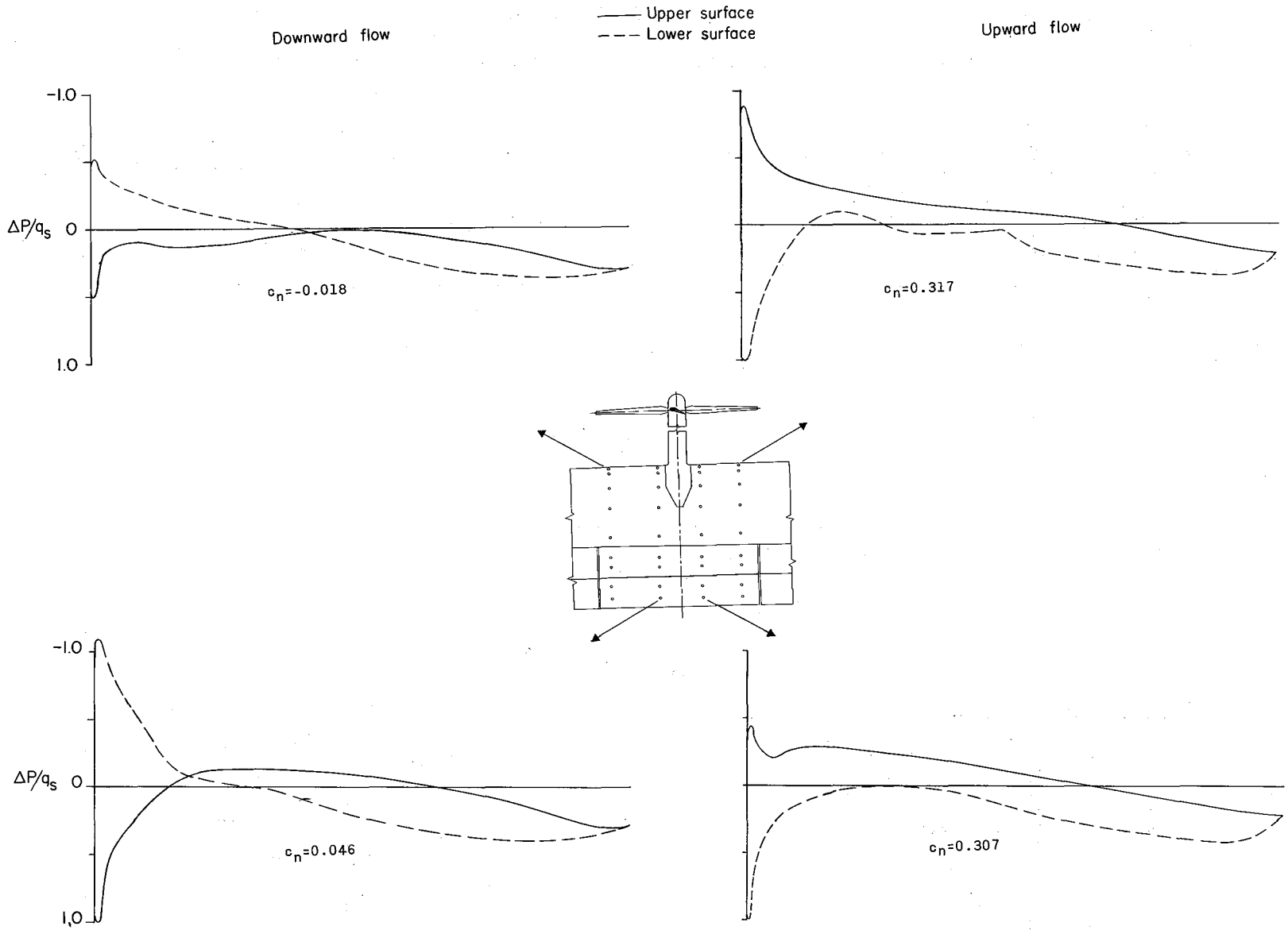

(a) Normal pressure distributions over airfoil length.

Figure 7.- Pressure distributions on wing with flaps neutral. $i_w = 56^o$; z/D = 1.0.

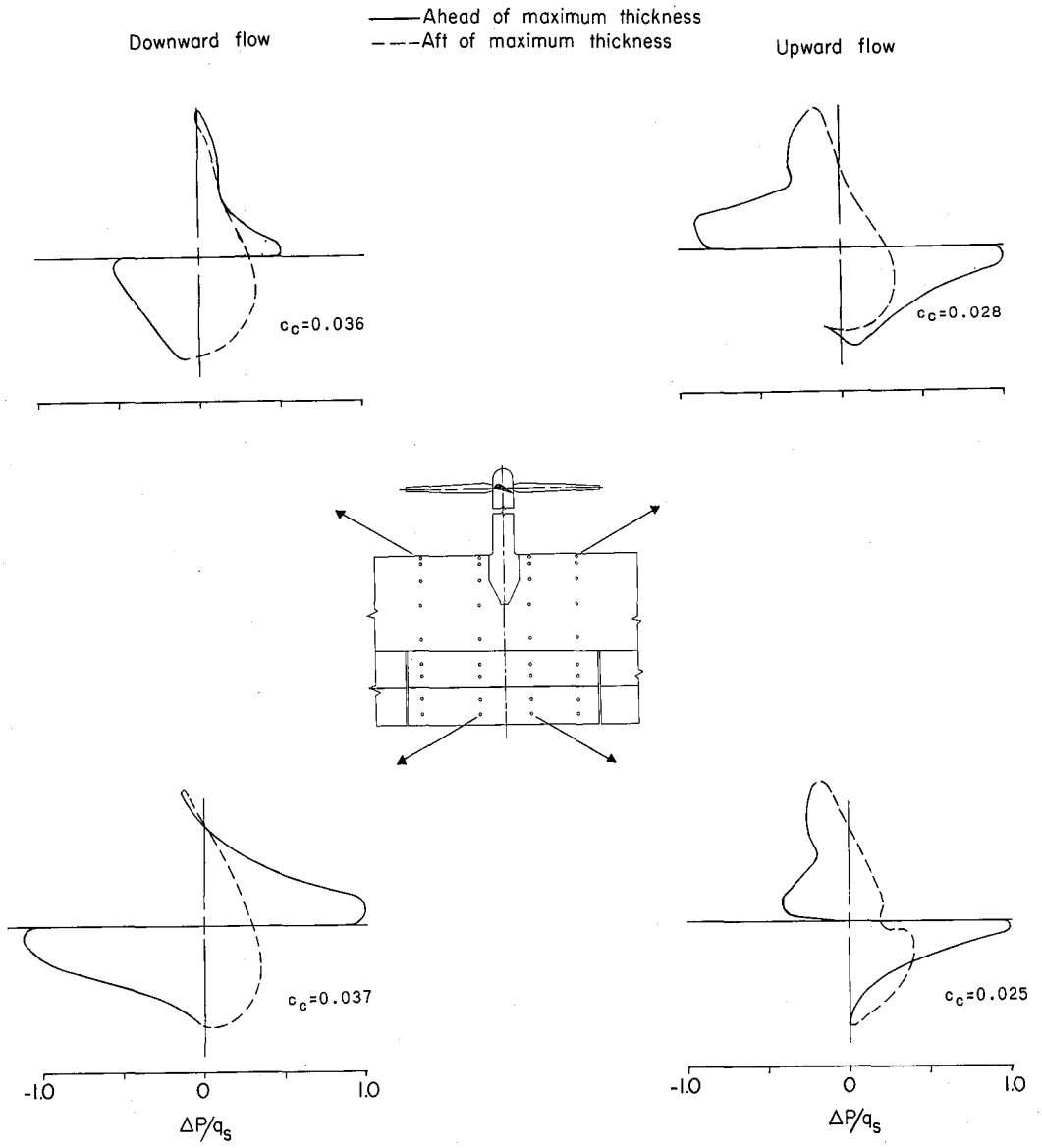

(b) Chord pressure distributions over airfoil thickness.

Figure 7.- Concluded.

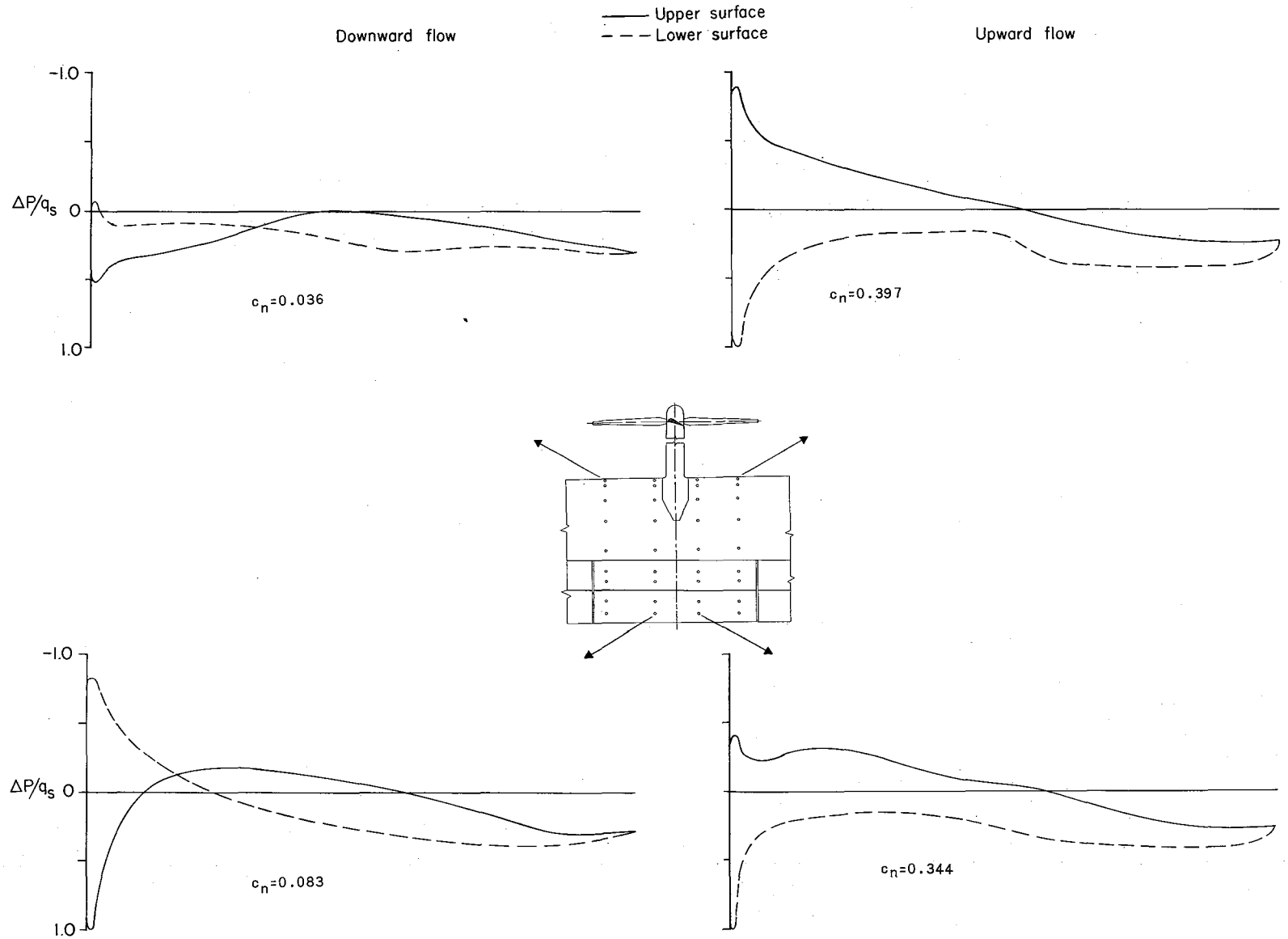

(a) Normal pressure distributions over airfoil length.

Figure 8.- Pressure distributions on wing with flaps neutral. $i_w = 75^\circ$; $z/D = 1.0$.

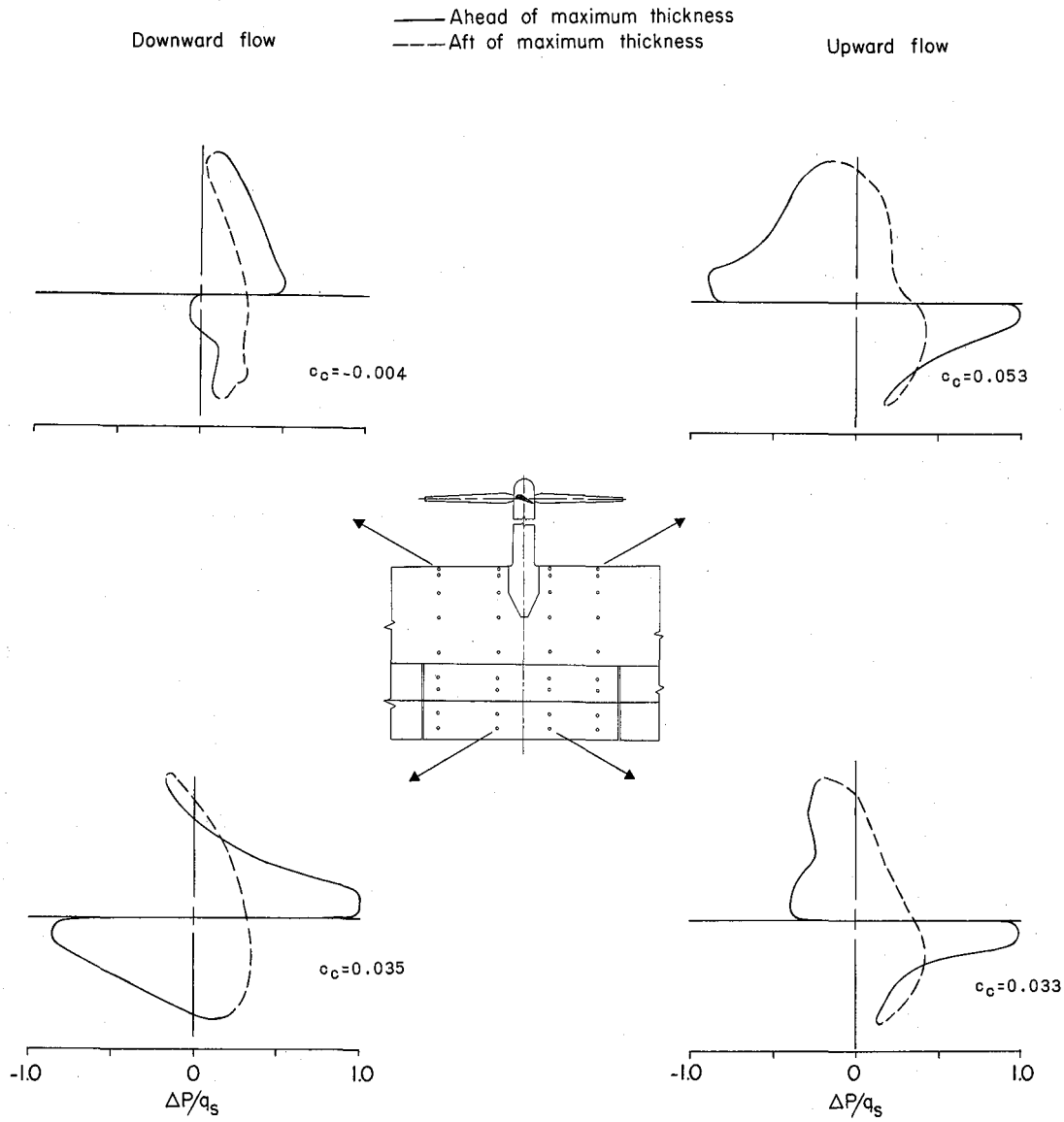

(b) Chord pressure distributions over airfoil thickness.

Figure 8.- Concluded.

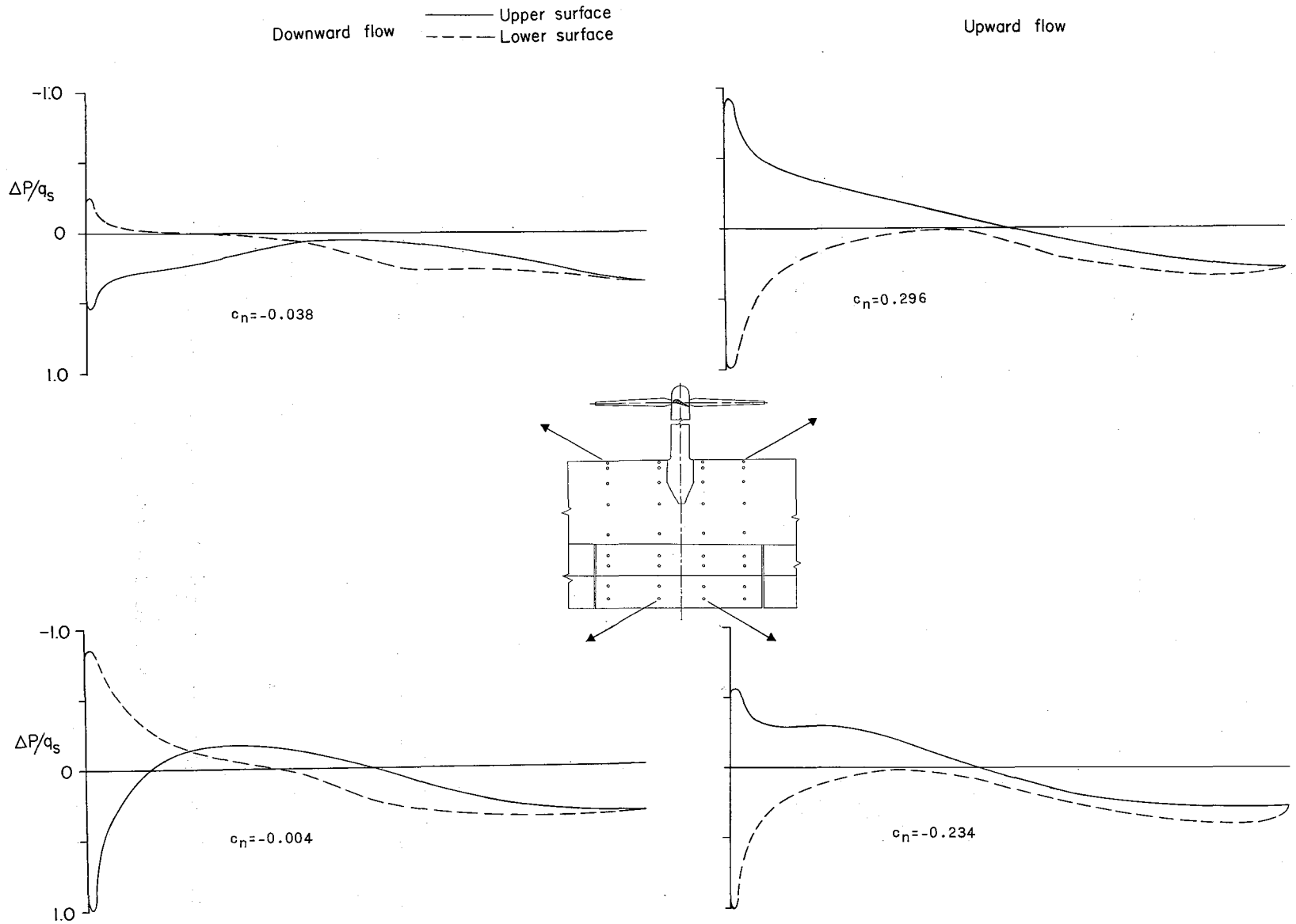

(a) Normal pressure distributions over airfoil length.

Figure 9.- Pressure distributions on wing with flaps neutral. $i_w = 90^o$; z/D = 1.0.

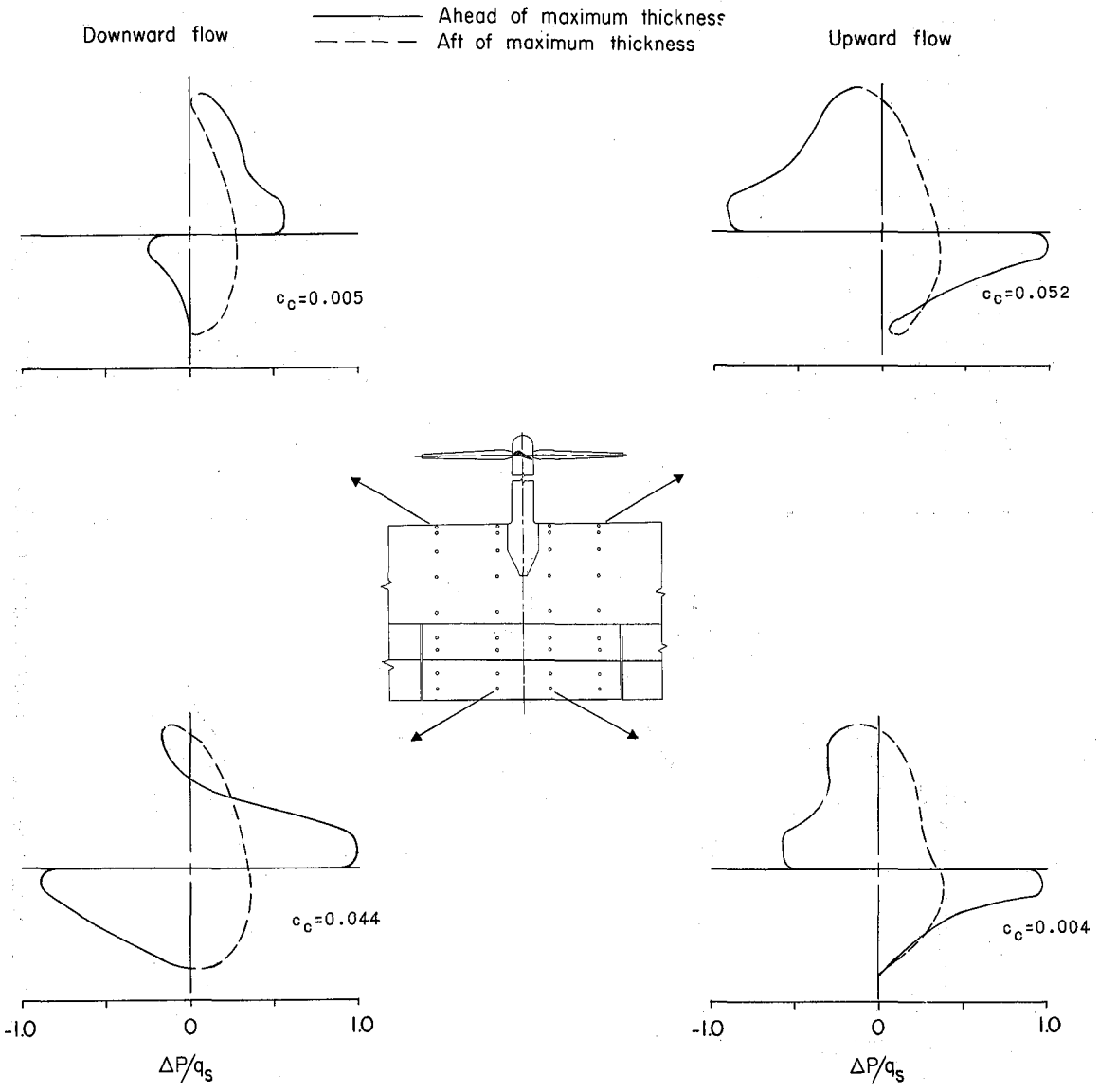

(b) Chord pressure distributions over airfoil thickness.

Figure 9.- Concluded.

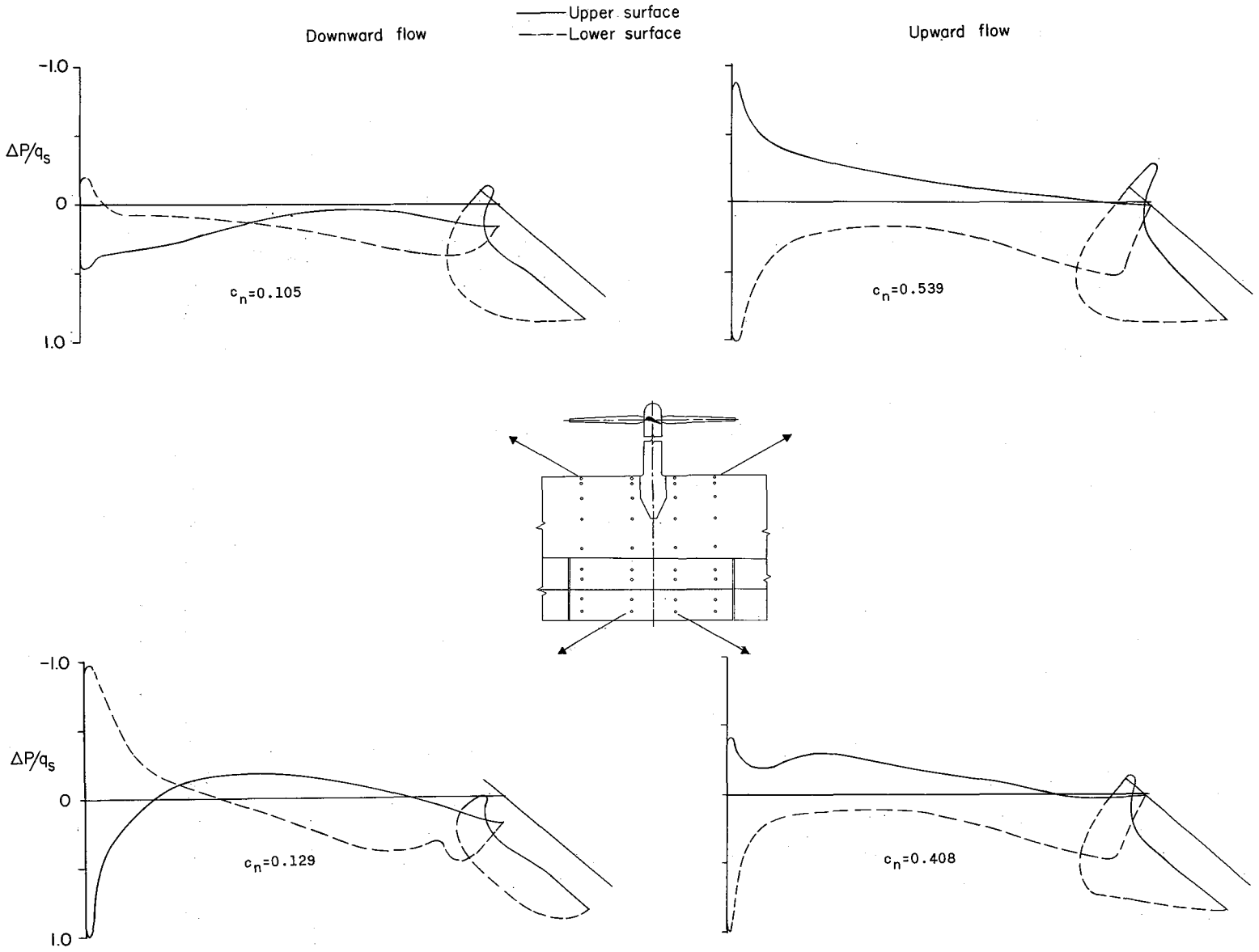

(a) Normal pressure distributions over airfoil length.

Figure 10.- Pressure distributions. $i_w = 7^4{}^o$; $z/D = 1.0$; $\delta_{f,55} = 0^o$; $\delta_{f,30} = 38.6^o$.

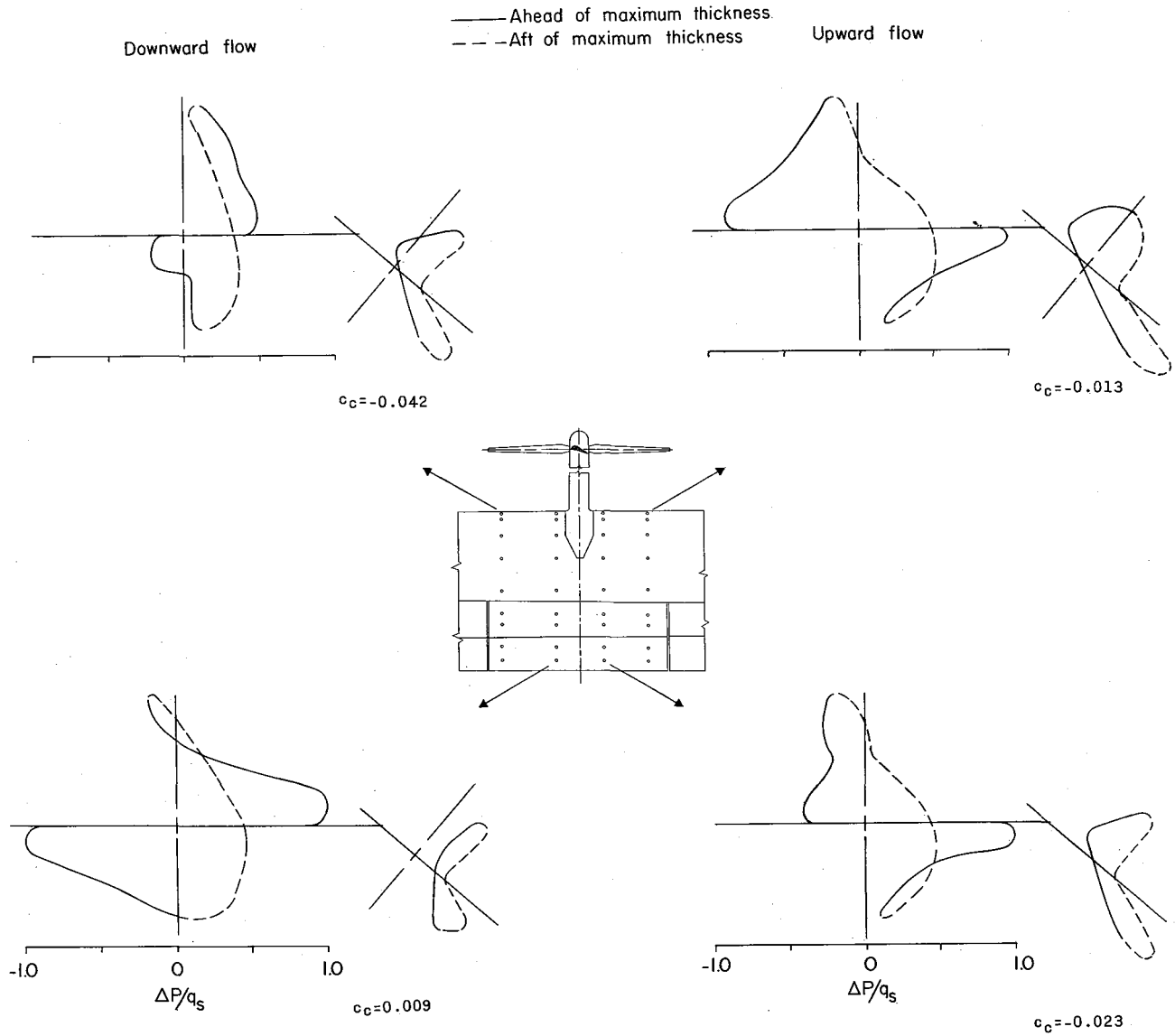

(b) Chord pressure distributions over airfoil thickness.

Figure 10.- Concluded.

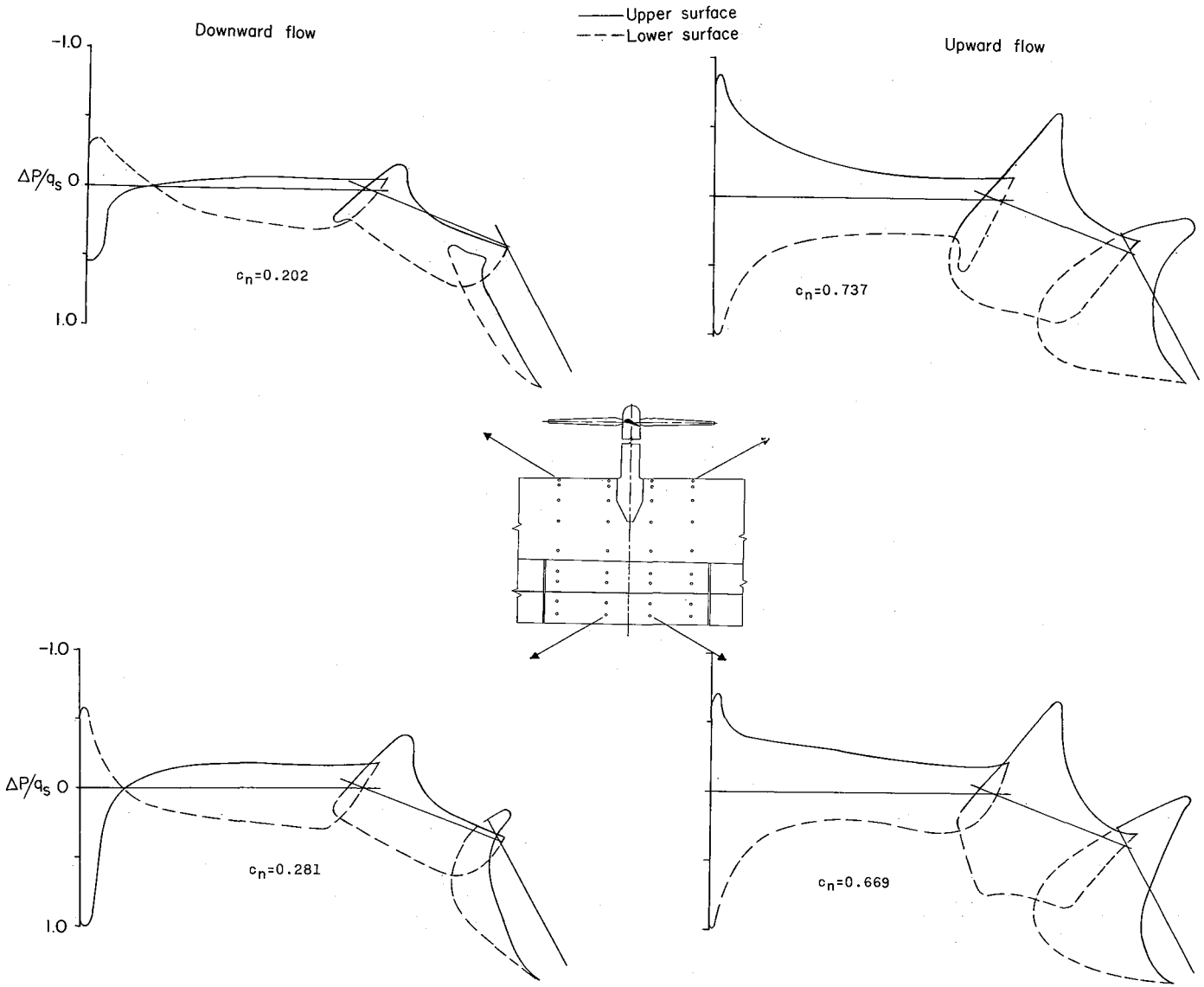

(a) Normal pressure distributions over airfoil length.

Figure 11.- Pressure distributions. $i_w = 64.5^\circ$; $z/D = 1.0$; $\delta_{f,55} = 19.8^\circ$; $\delta_{f,30} = 38.6^\circ$.

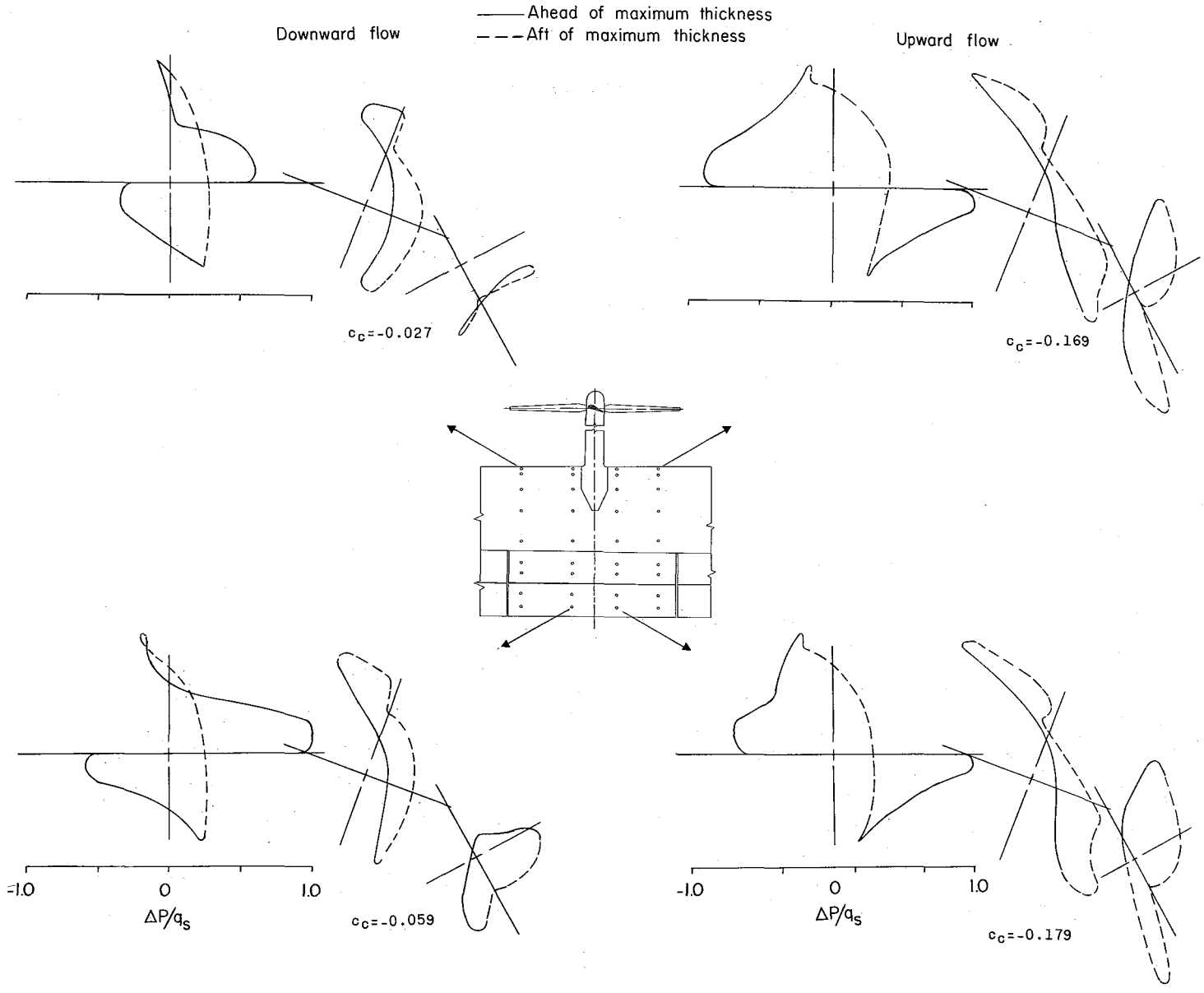

(b) Chord pressure distributions over airfoil thickness.

Figure 11.- Concluded.

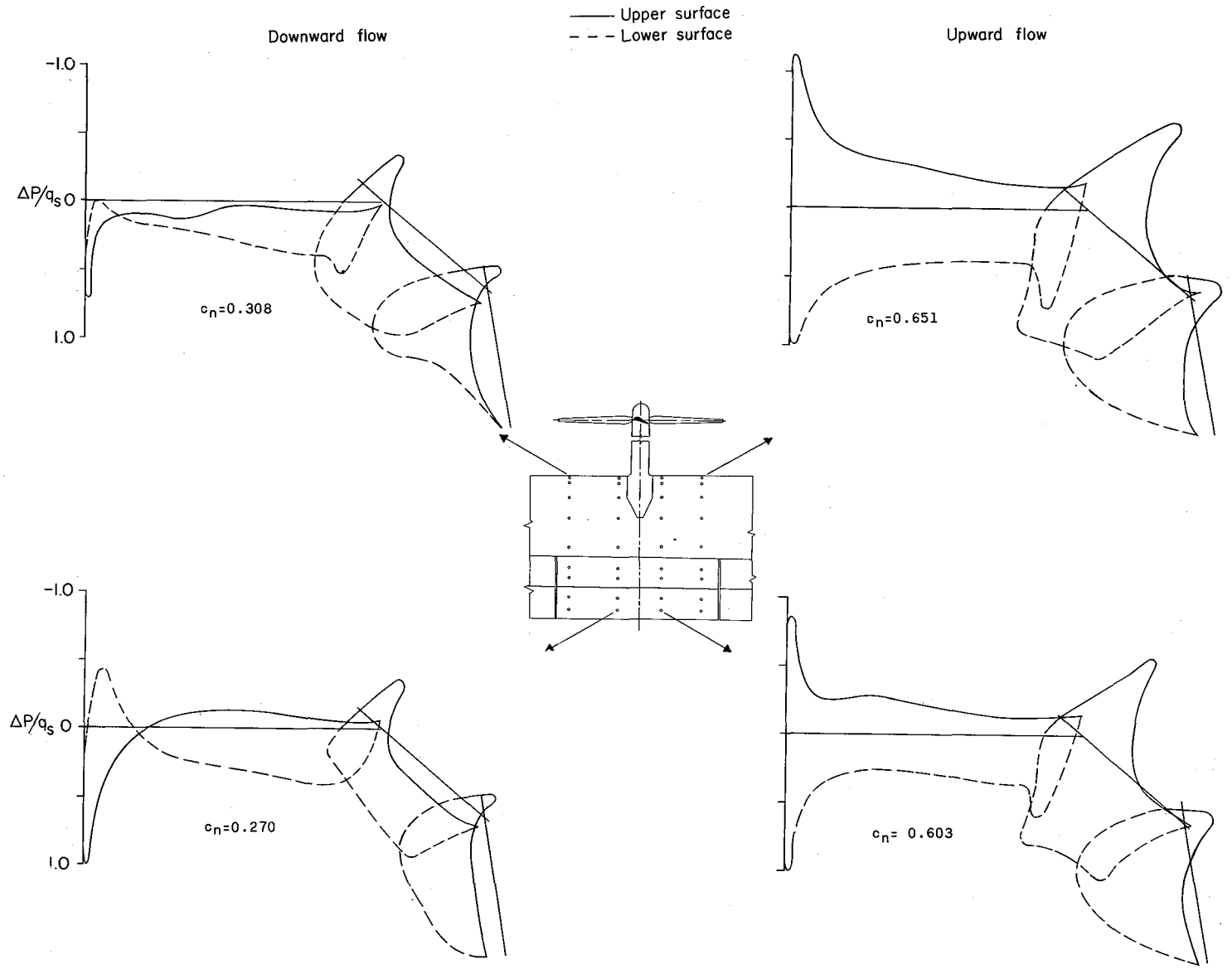

(a) Normal pressure distributions over airfoil length.

Figure 12.- Pressure distributions. $i_w = 61.2^\circ$; $z/D = 1.0$; $\delta_{f,55} = 39.3^\circ$; $\delta_{f,30} = 38.6^\circ$.

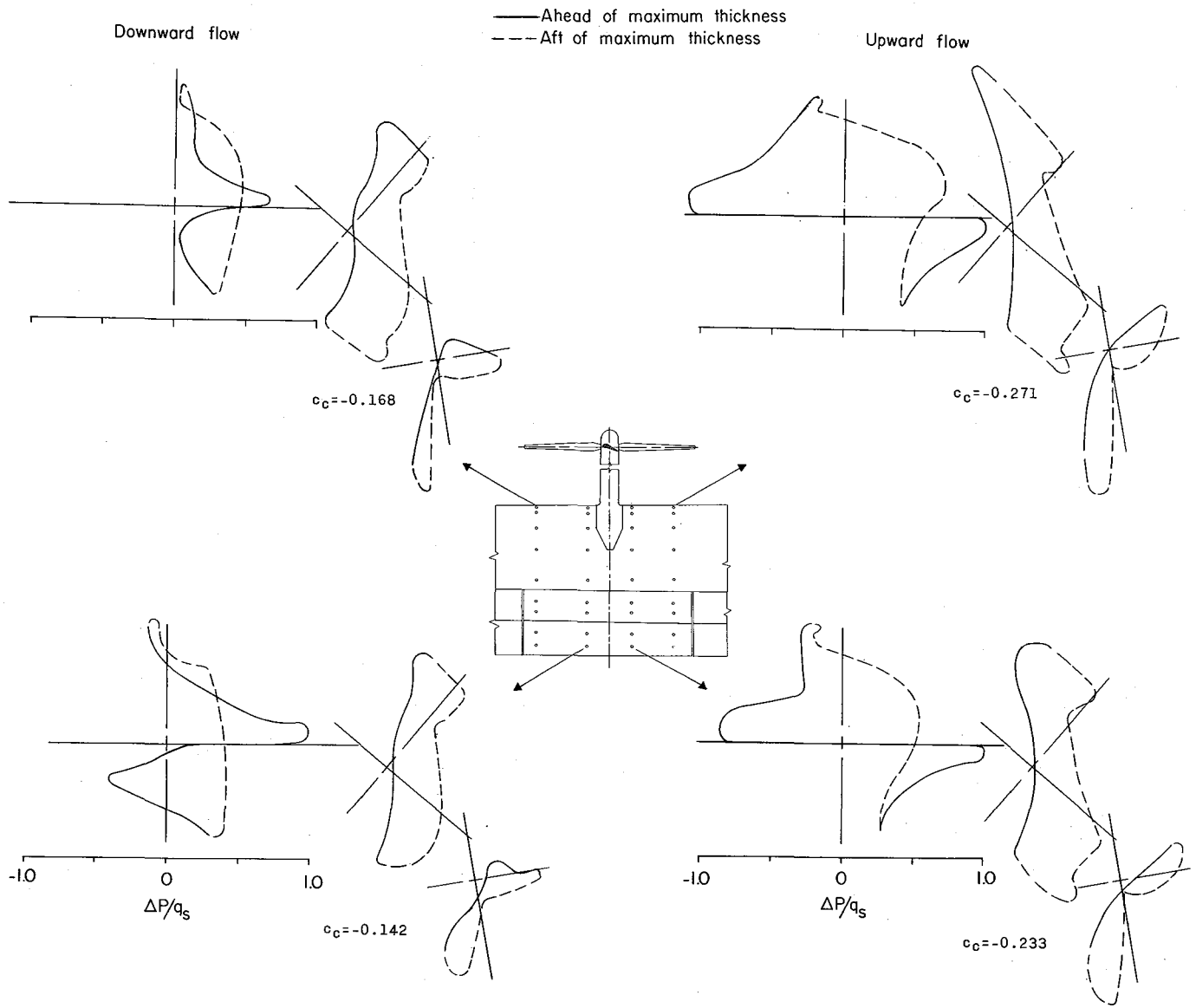

(b) Chord pressure distributions over airfoil thickness.

Figure 12.- Concluded.

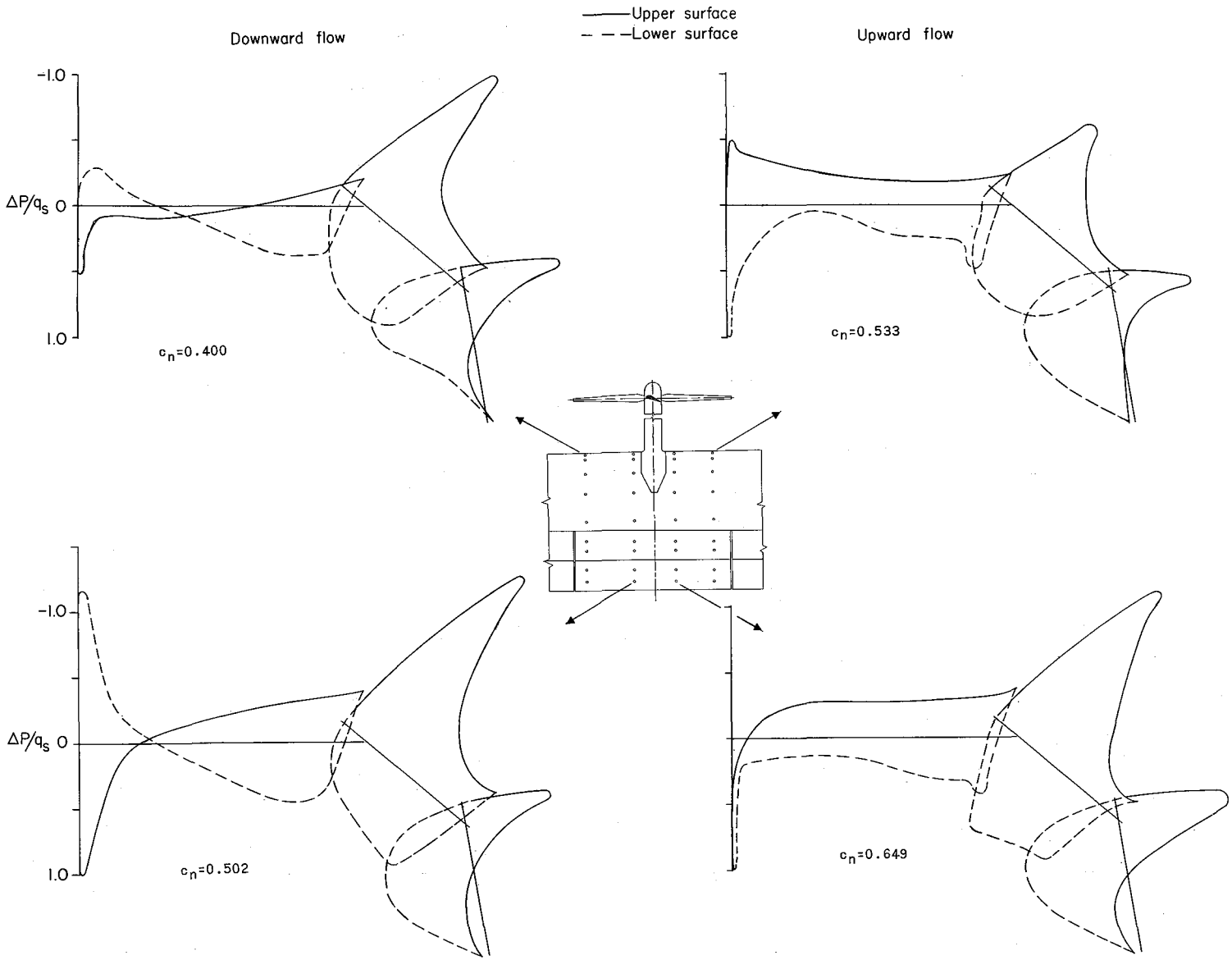

(a) Normal pressure distributions over airfoil length.

Figure 13.- Pressure distributions. $i_w = 0^\circ$; $z/D = 1.0$; $\delta_{f,55} = 39.3^\circ$; $\delta_{f,30} = 38.6^\circ$.

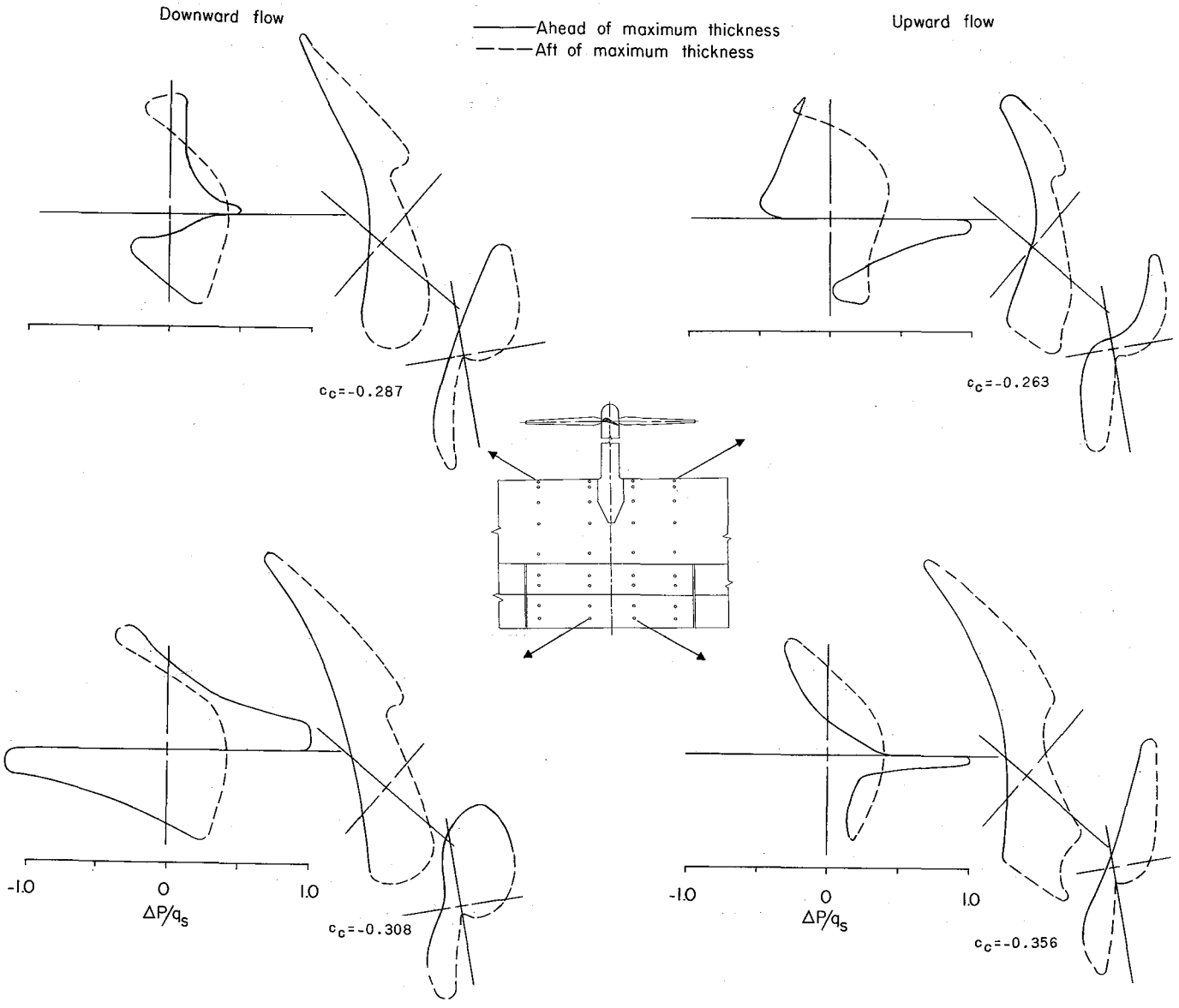

(b) Chord pressure distributions over airfoil thickness.

Figure 13.- Concluded.

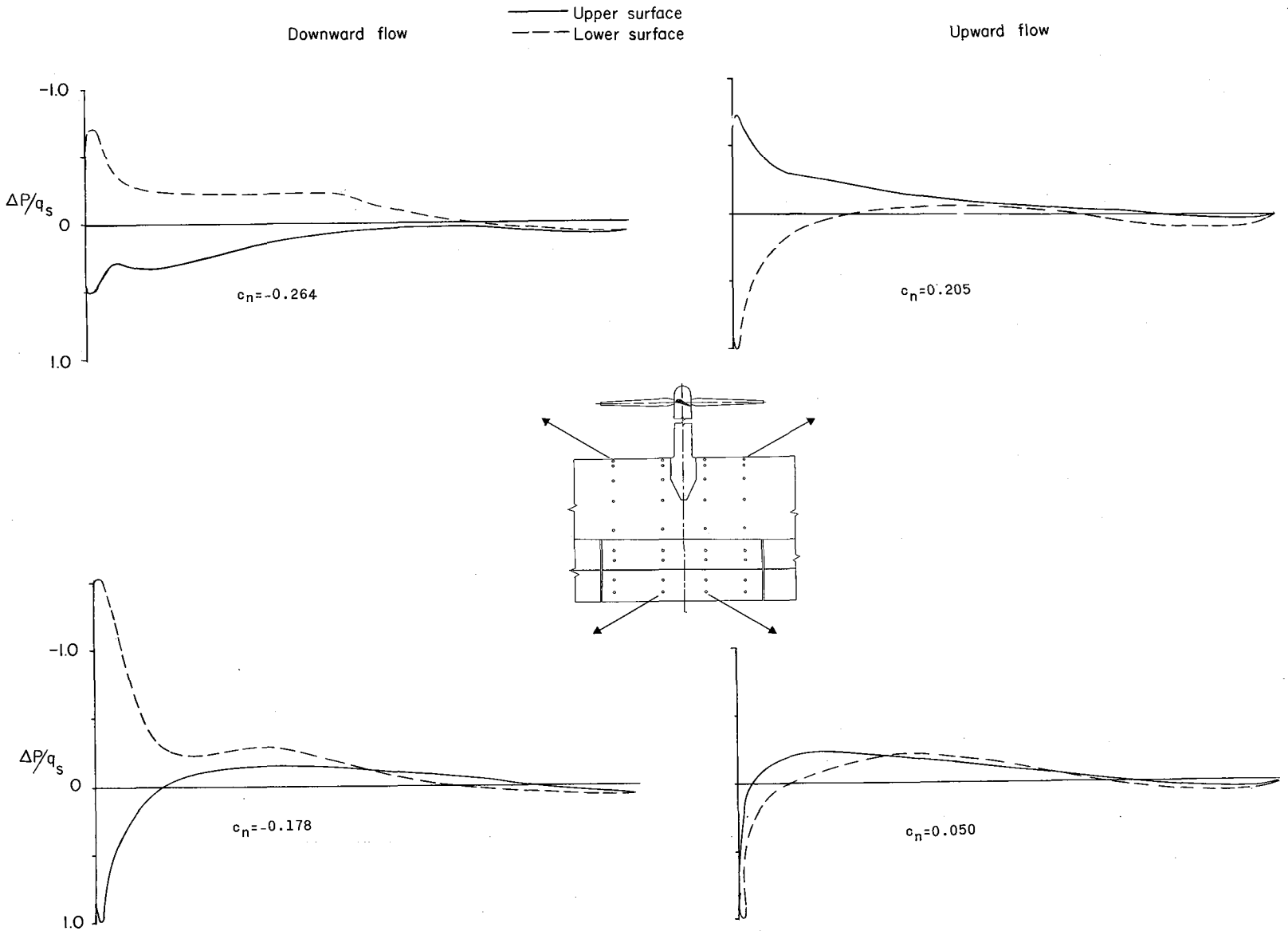

(a) Normal pressure distributions over airfoil length.

Figure 14.- Pressure distributions on wing with flaps neutral. $i_w = 0^o$; $z/D = 2.4$.

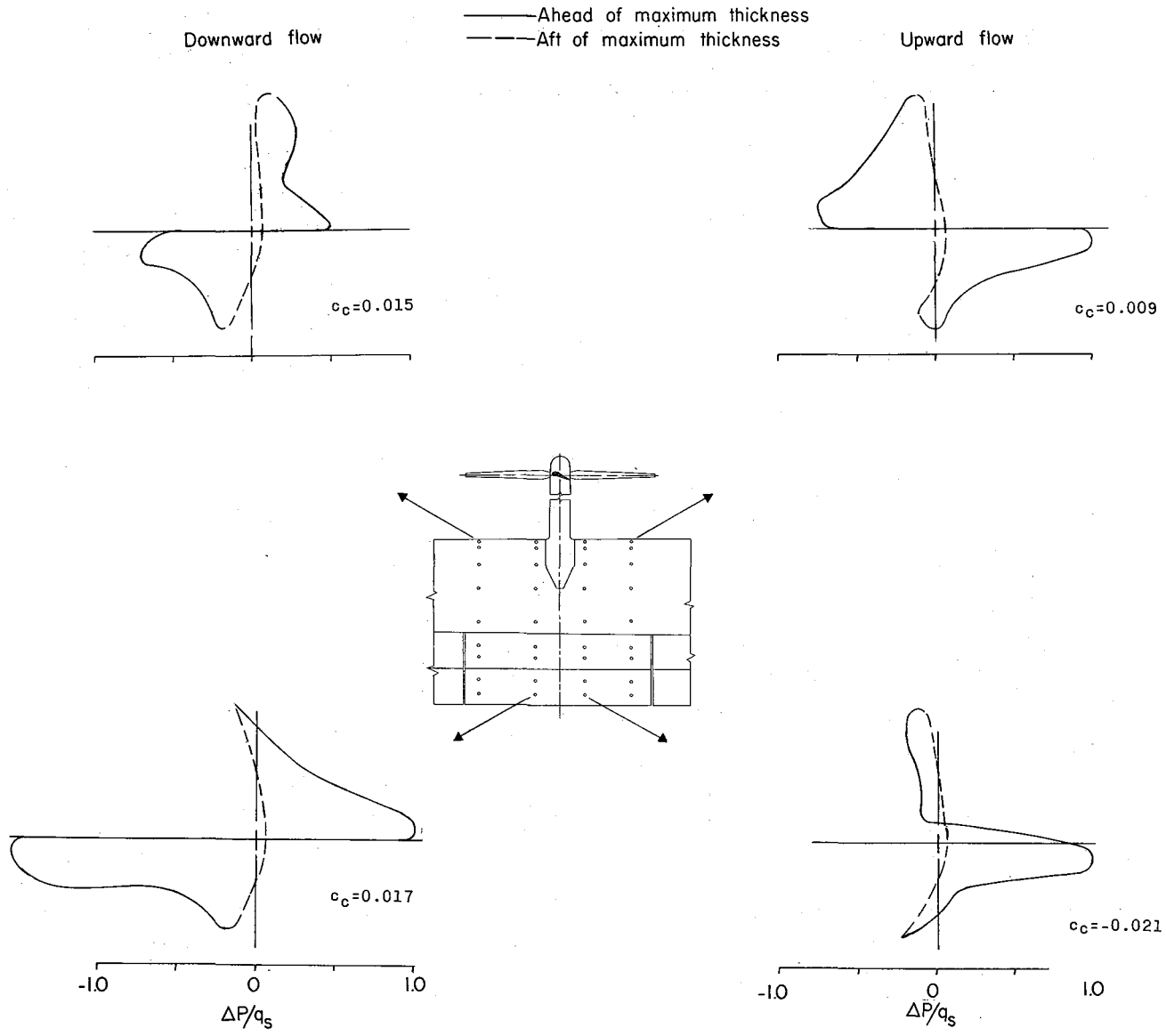

(b) Chord pressure distributions over airfoil thickness.

Figure 14.- Concluded.

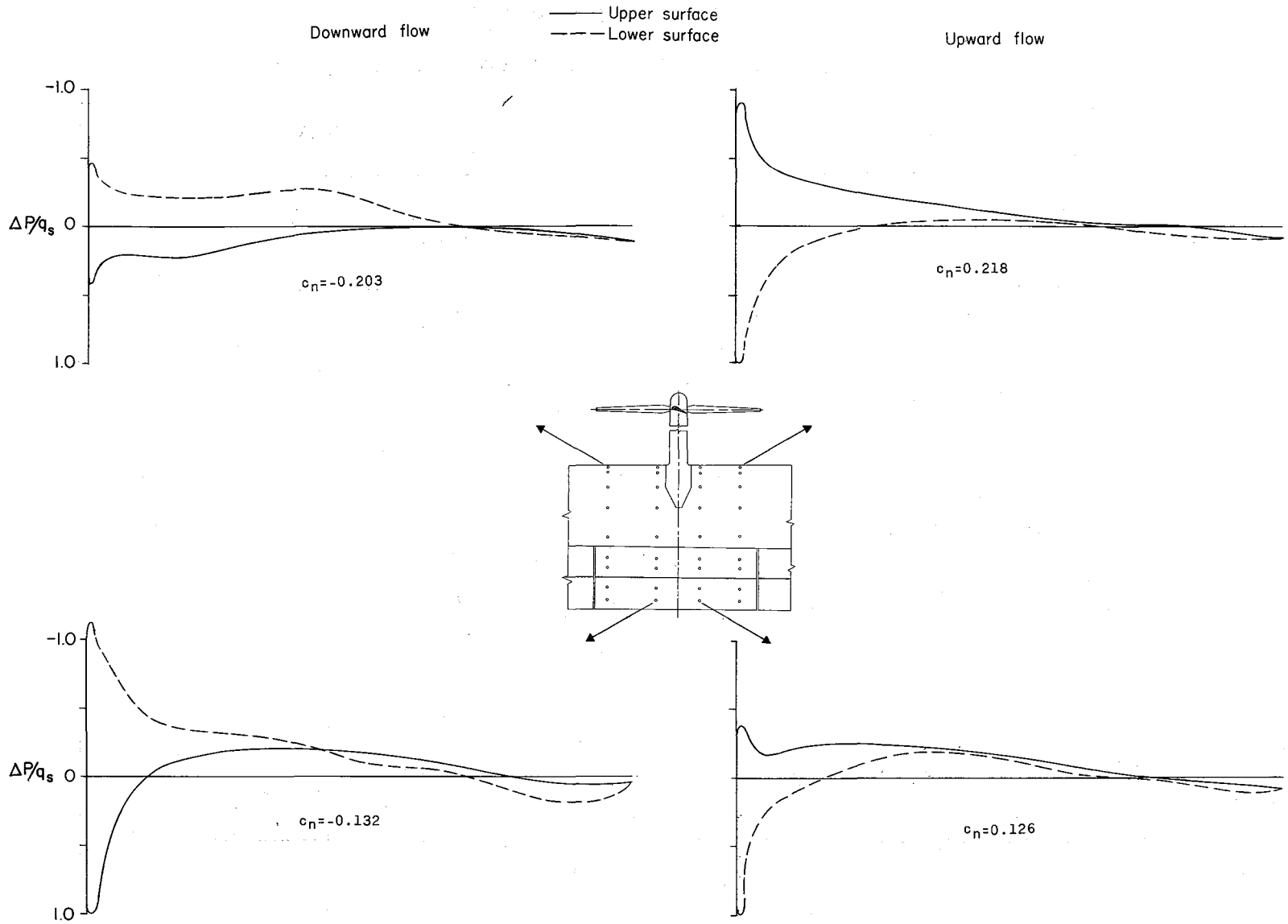

(a) Normal pressure distributions over airfoil length.

Figure 15.- Pressure distributions on wing with flaps neutral. $i_w = 56^\circ$; $z/D = 2.4$.

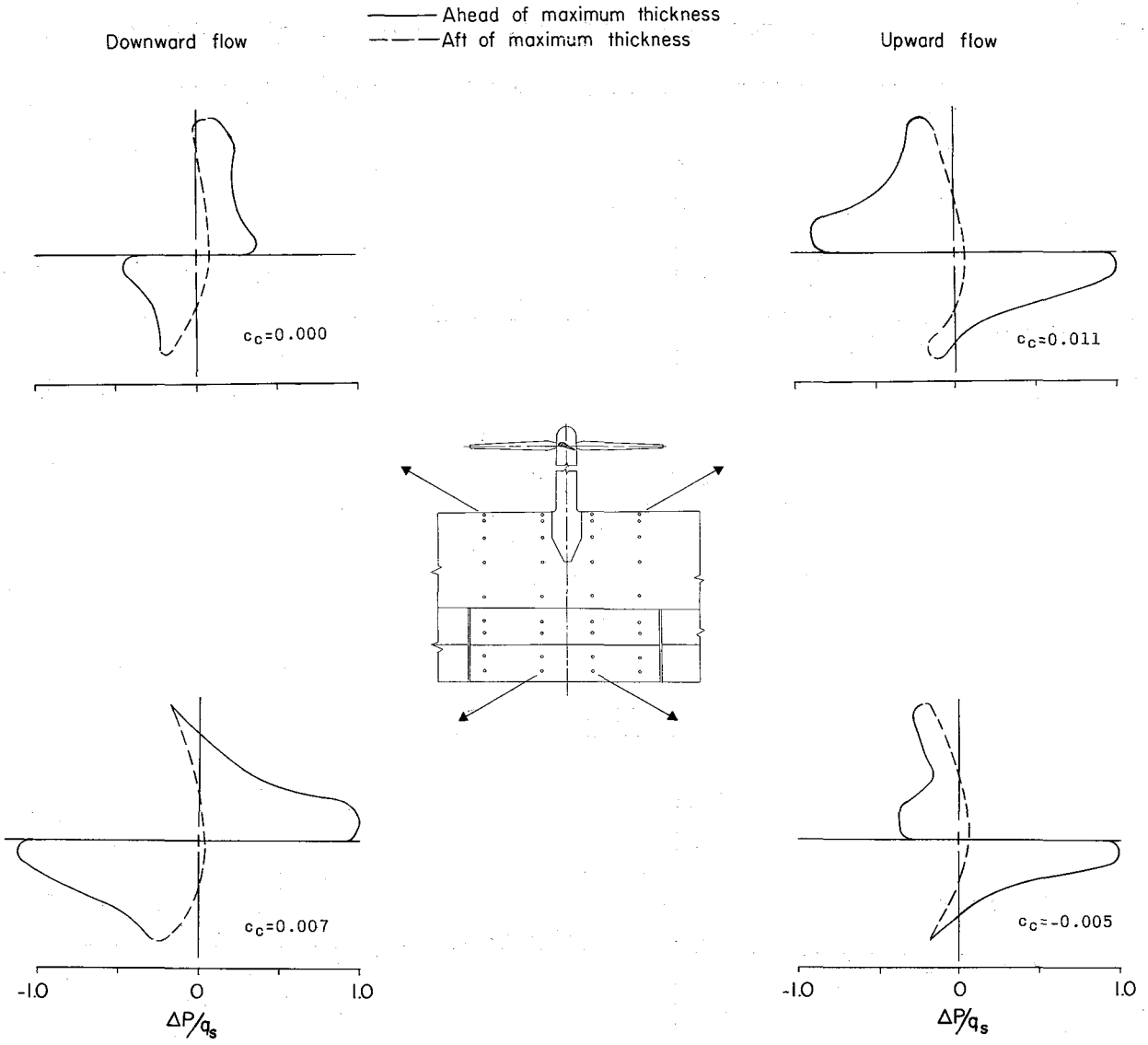

(b) Chord pressure distributions over airfoil thickness.

Figure 15.- Concluded.

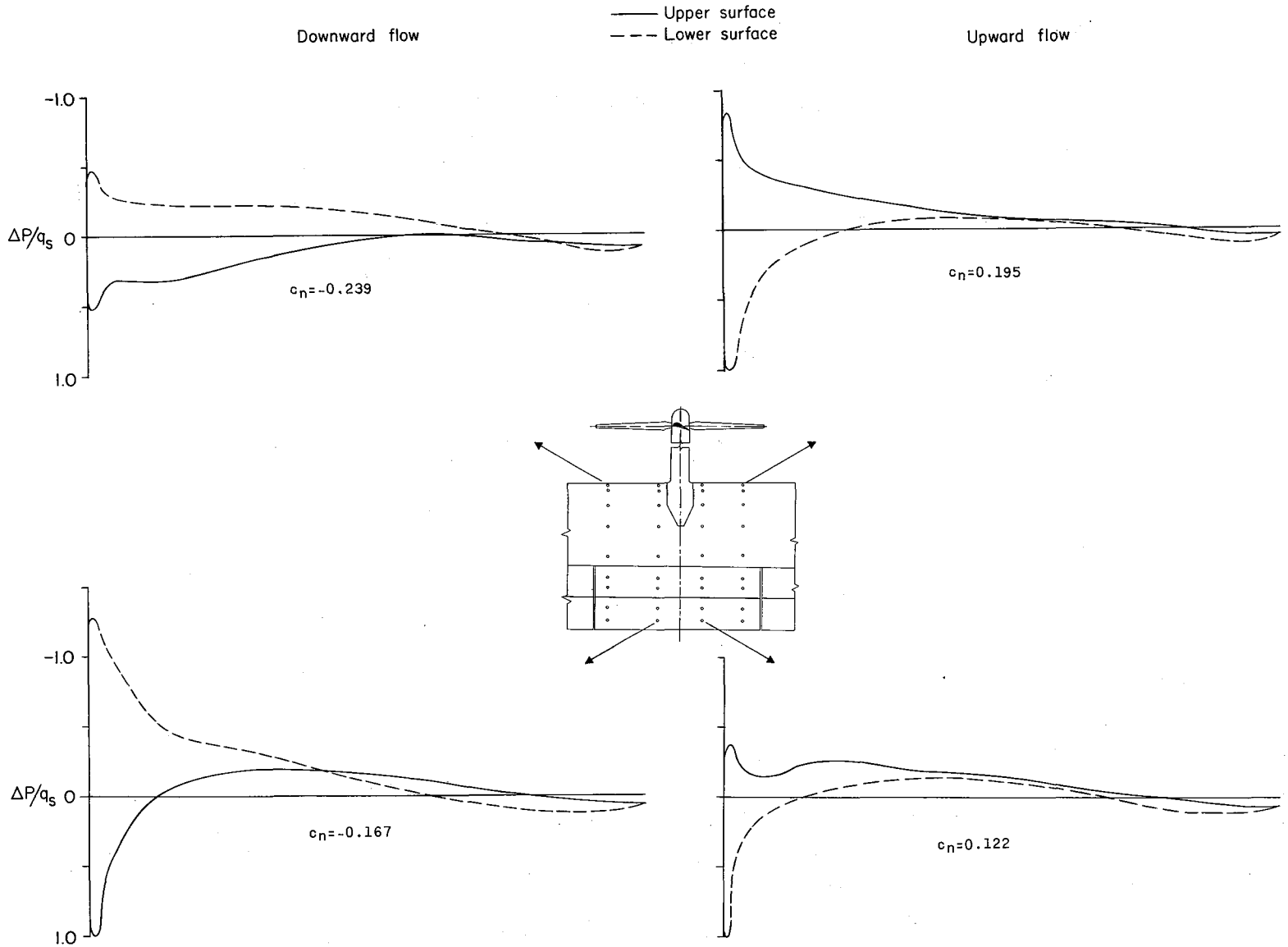

(a) Normal pressure distributions over airfoil length.

Figure 16.- Pressure distributions on wing with flaps neutral. $i_w = 75^\circ$; $z/D = 2.4$.

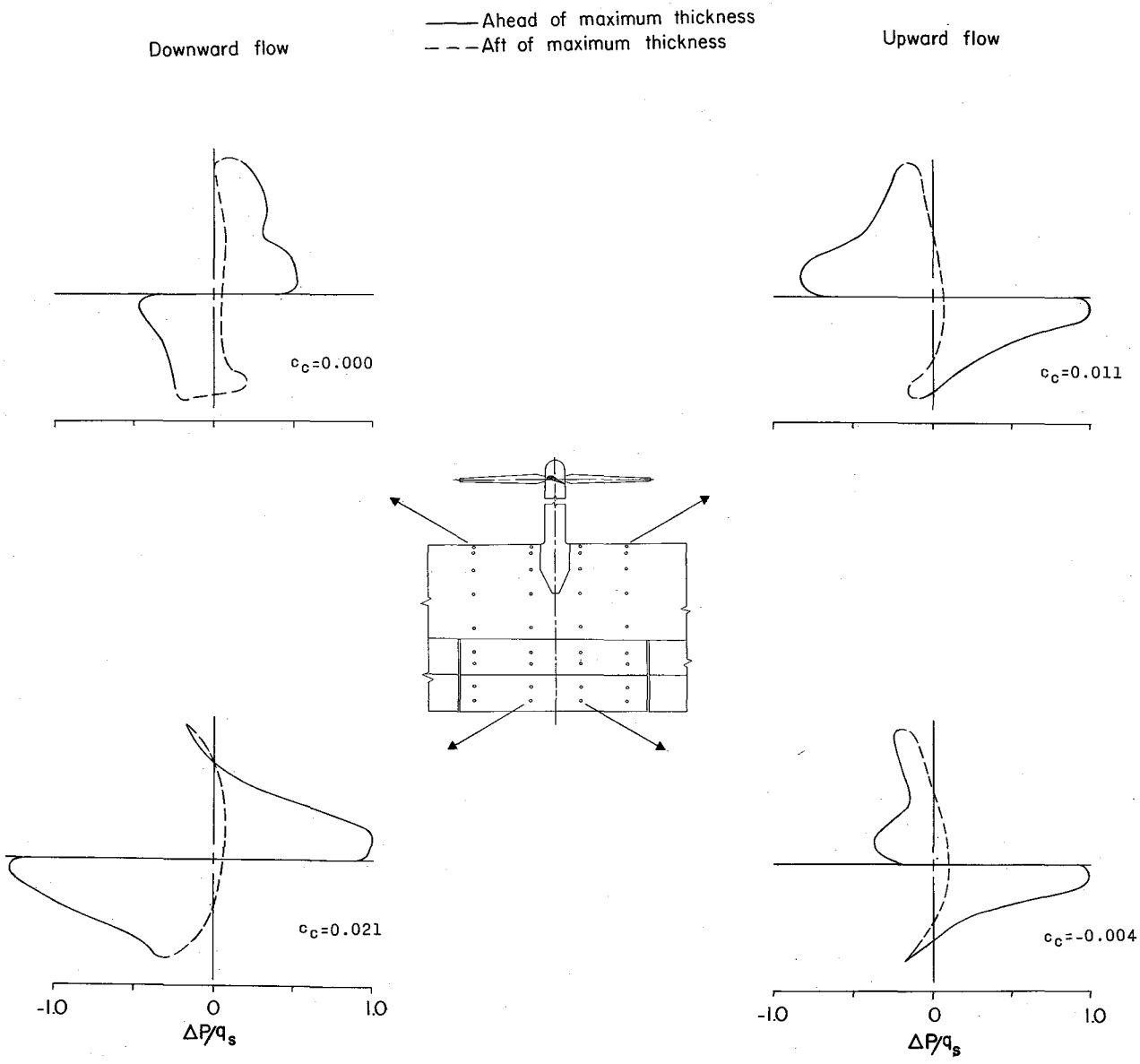

(b) Chord pressure distributions over airfoil thickness.

Figure 16.- Concluded.

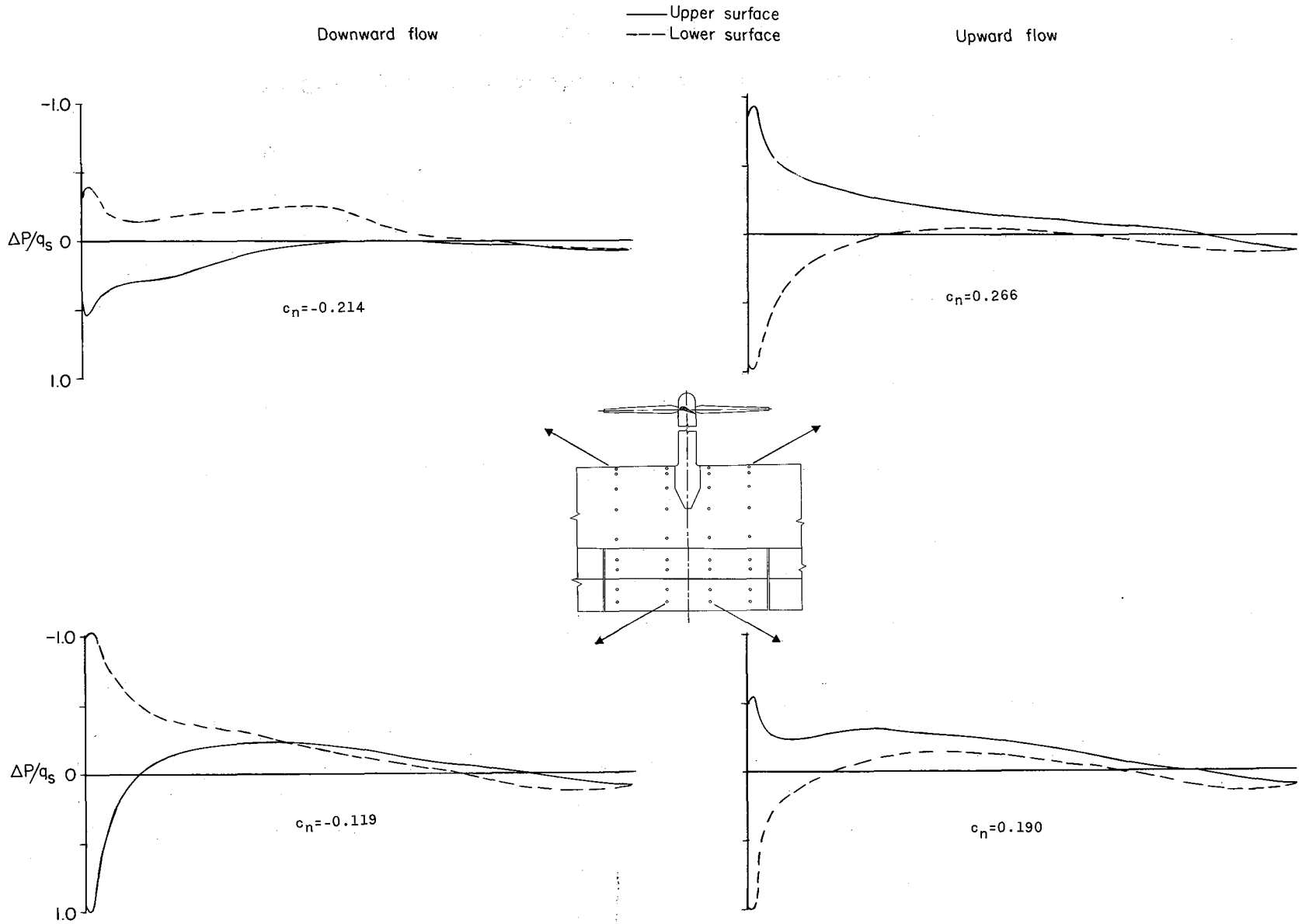

(a) Normal pressure distributions over airfoil length.

Figure 17.- Pressure distributions on wing with flaps neutral. $i_w = 90^o$; $z/D = 2.4$.

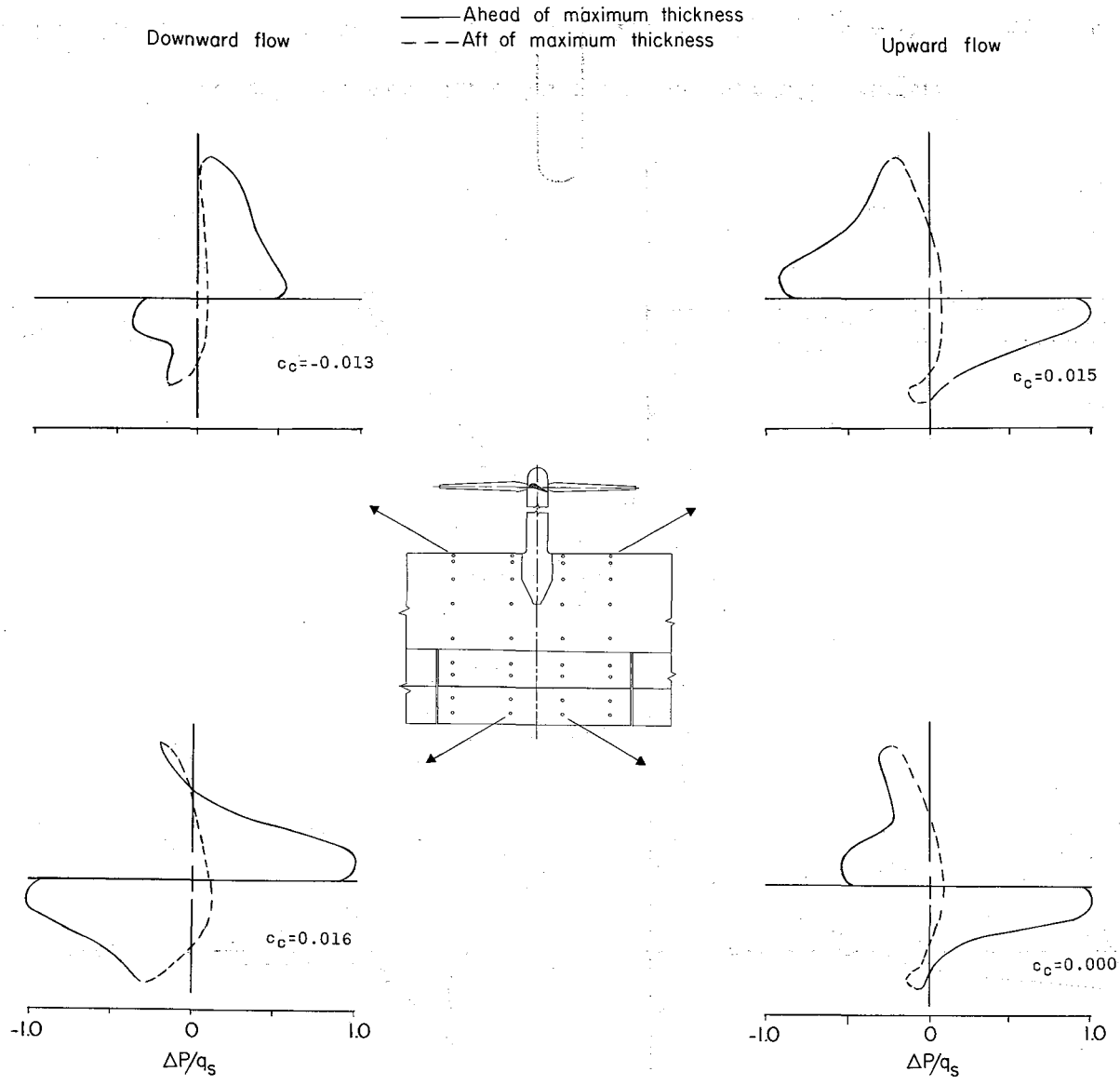

(b) Chord pressure distributions over airfoil thickness.

Figure 17.- Concluded.

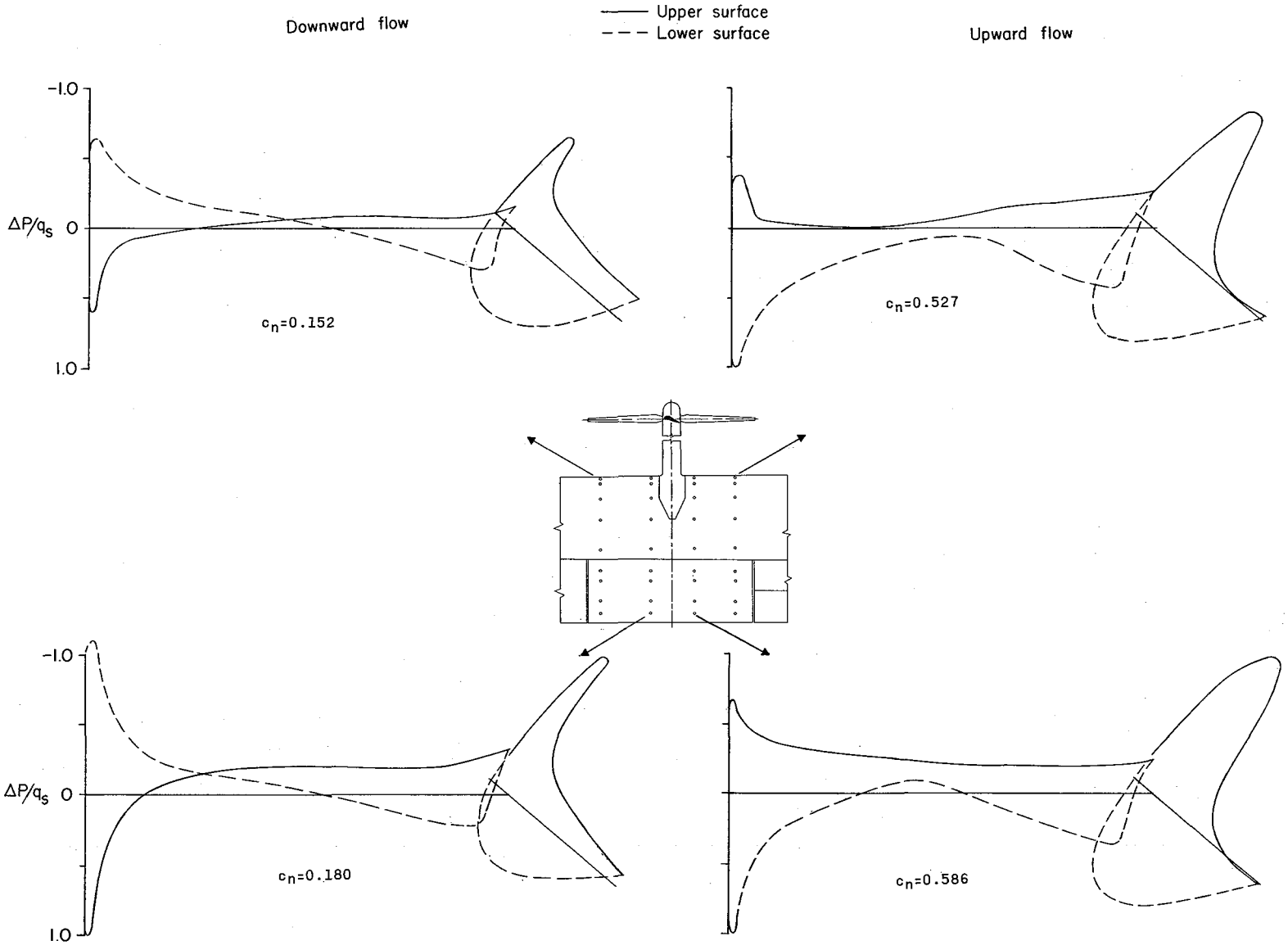

(a) Normal pressure distributions over airfoil length.

Figure 18.- Pressure distributions. $i_w = 68^\circ$; $z/D = 2.4$; $\delta_{f,55} = 0^\circ$; $\delta_{f,30} = 38.6^\circ$.

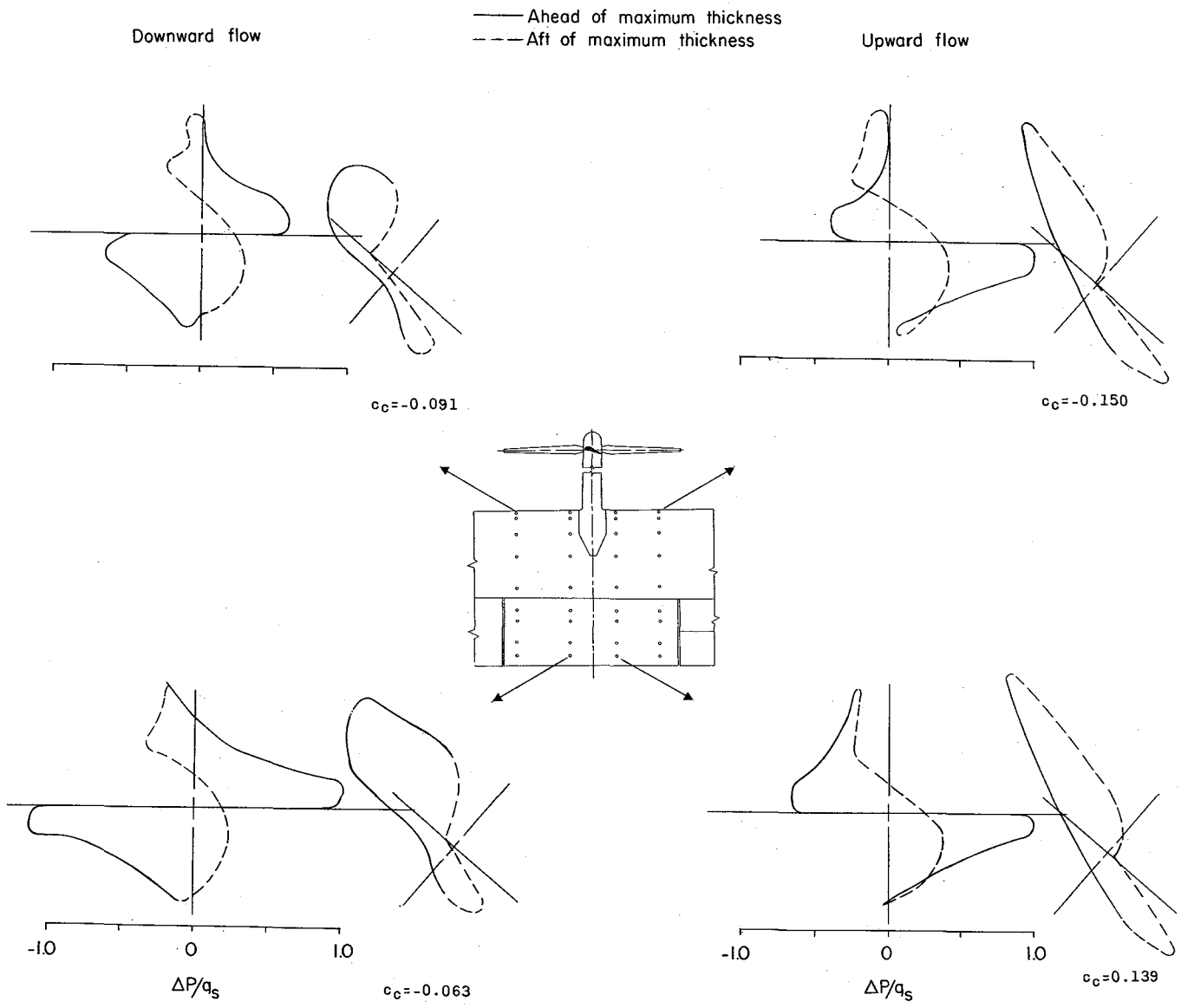

(b) Chord pressure distributions over airfoil thickness.

Figure 18.- Concluded.

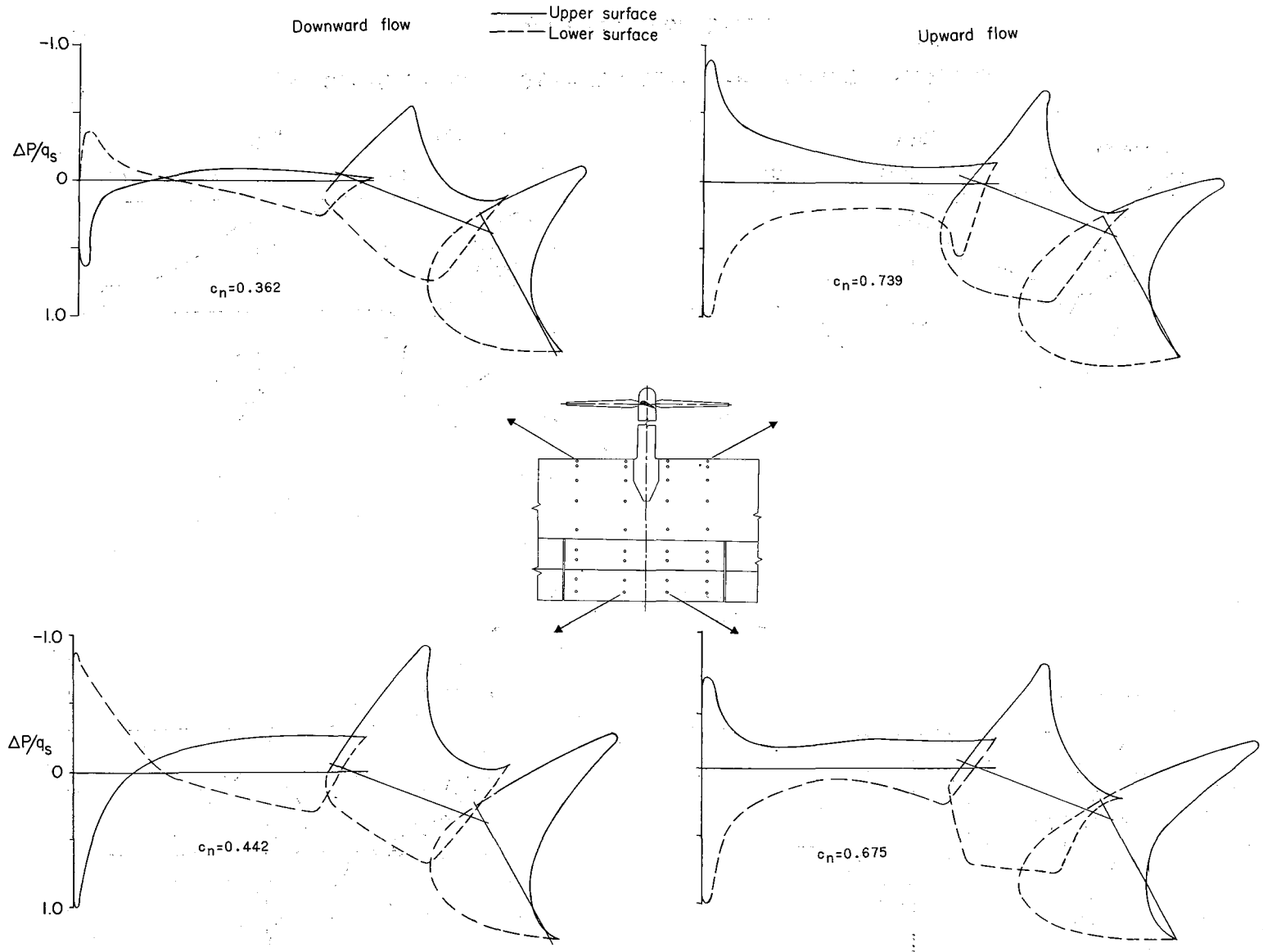

(a) Normal pressure distributions over airfoil length.

Figure 19.- Pressure distributions. $i_w = 57.8^\circ$; $z/D = 2.4$; $\delta_{f,55} = 19.8^\circ$; $\delta_{f,30} = 38.6^\circ$.

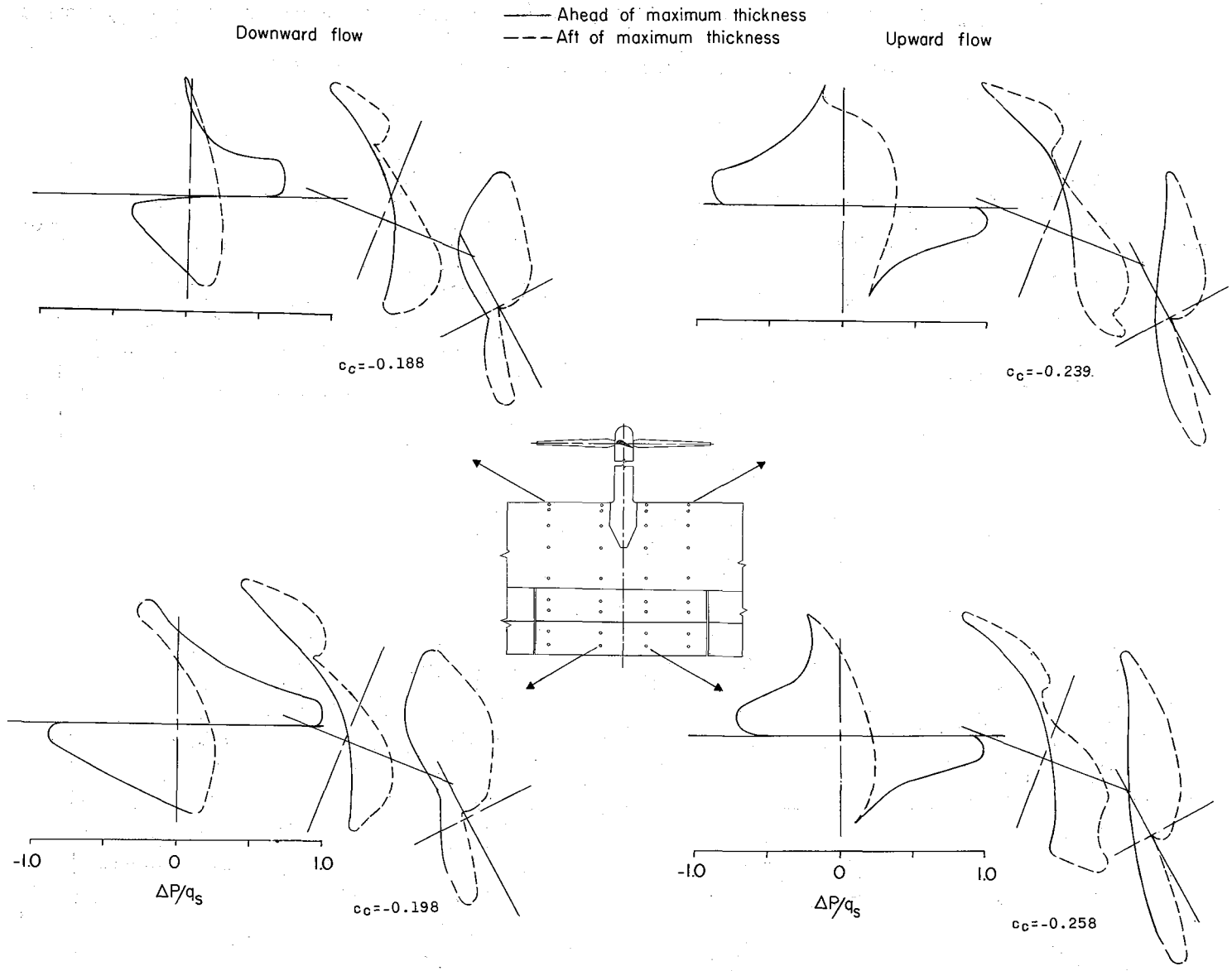

(b) Chord pressure distributions over airfoil thickness.

Figure 19.- Concluded.

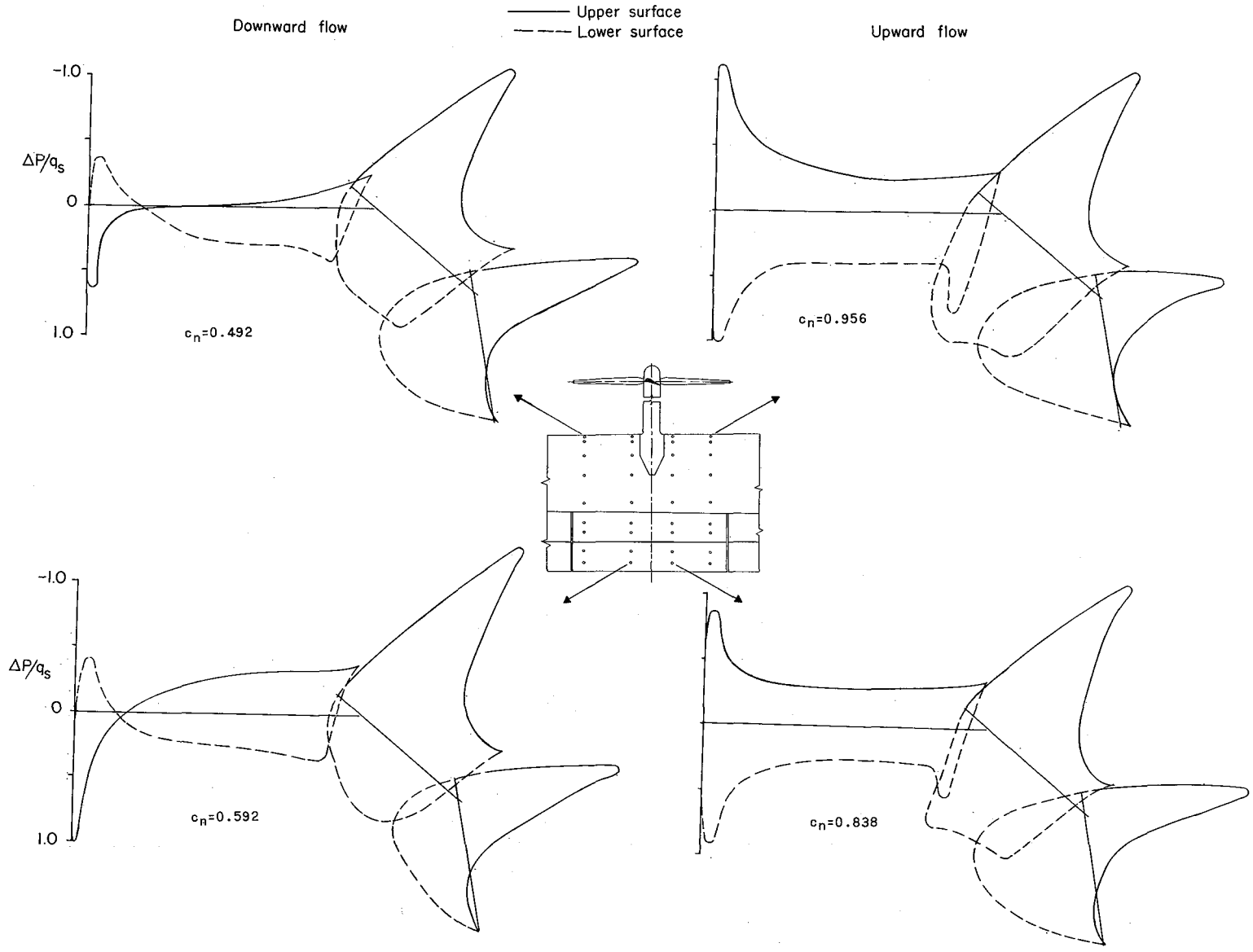

(a) Normal pressure distributions over airfoil length.

Figure 20.- Pressure distributions. $i_w = 43.5^\circ$; $z/D = 2.4$; $\delta_{f,55} = 39.3^\circ$; $\delta_{f,30} = 38.6^\circ$.

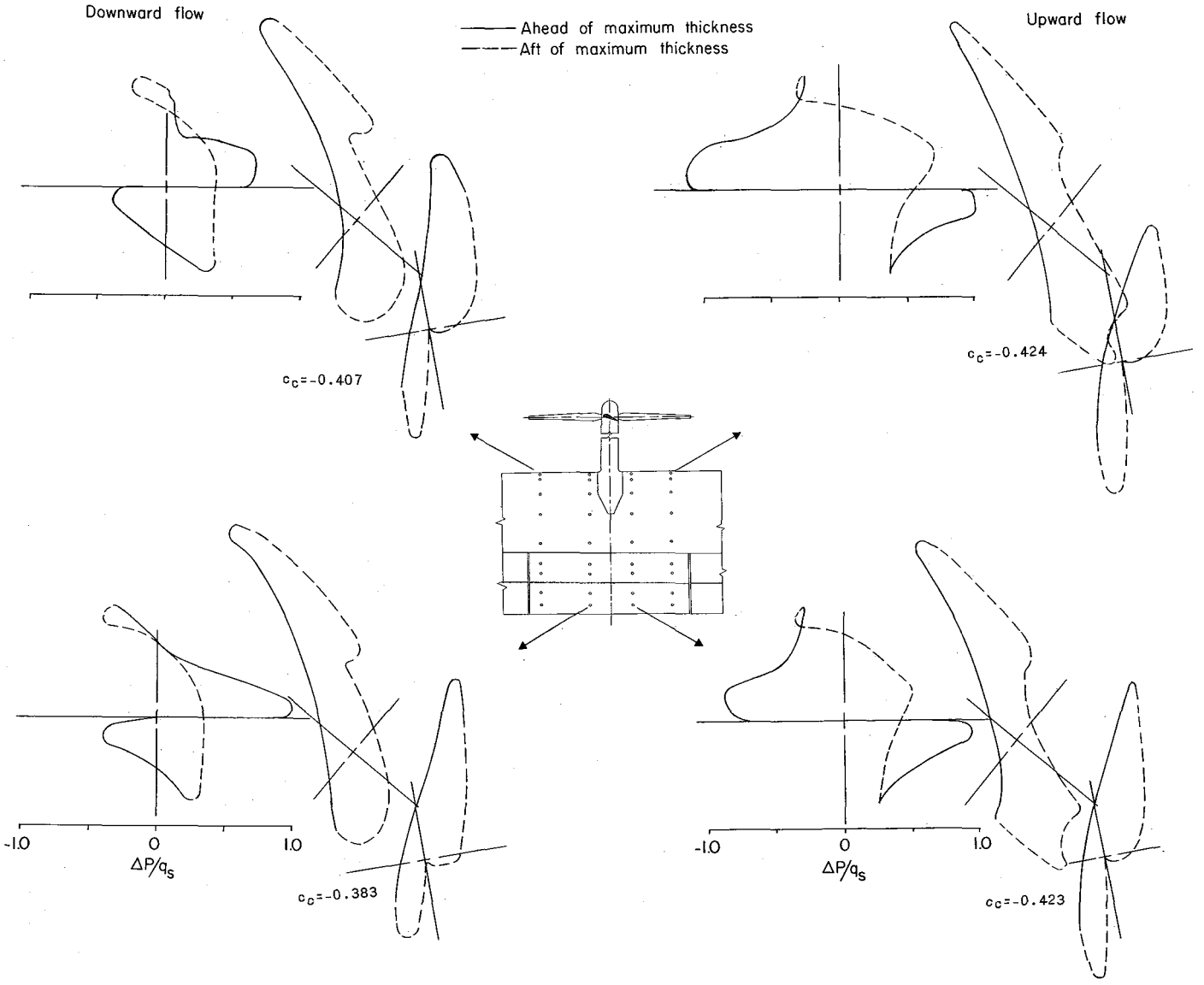

(b) Chord pressure distributions over airfoil thickness.

Figure 20.- Concluded.

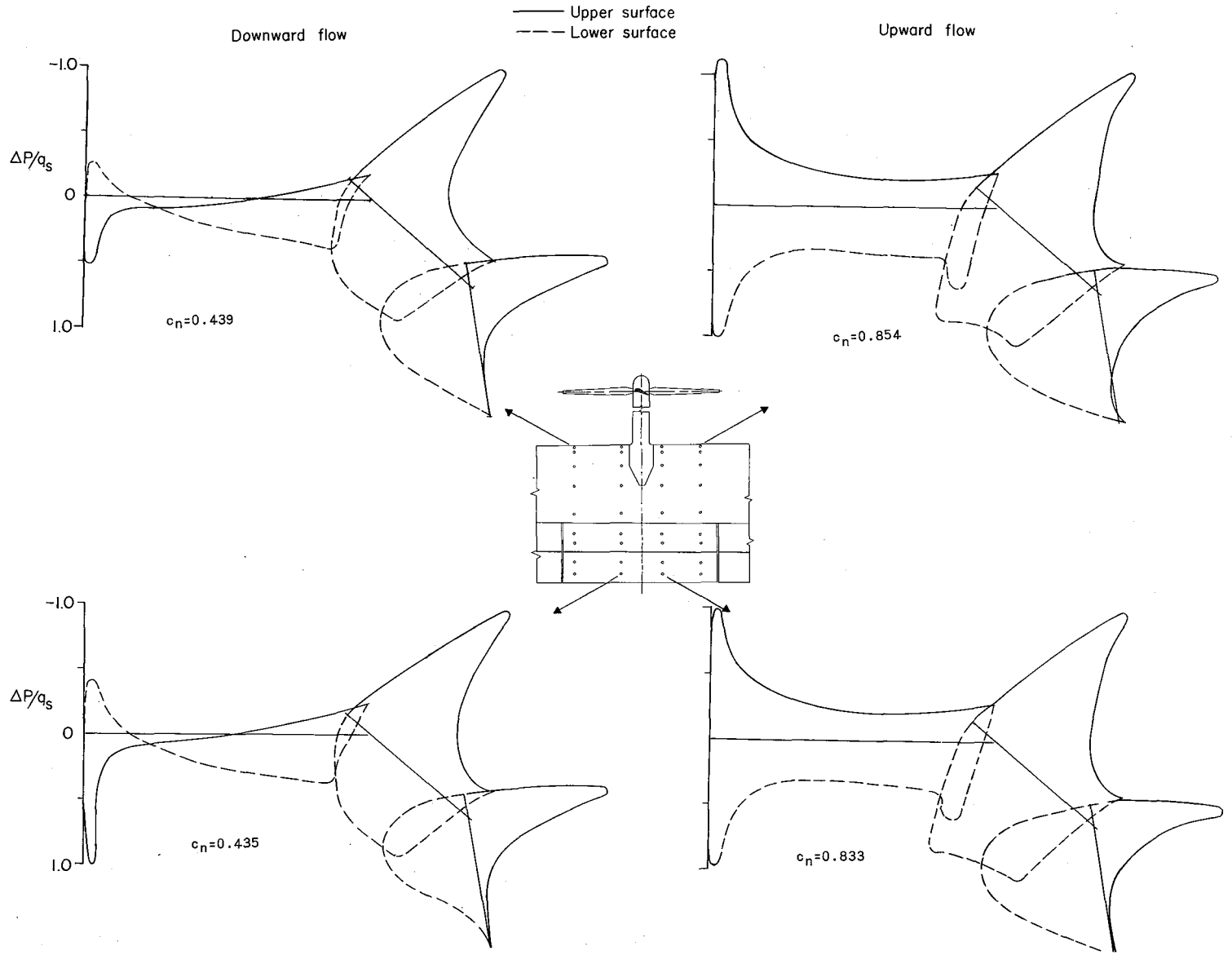

(a) Normal pressure distributions over airfoil length.

Figure 21.- Pressure distributions. $i_w = 0^\circ$; $z/D = 2.4$; $\delta_{f,55} = 39.3^\circ$; $\delta_{f,30} = 38.6^\circ$.

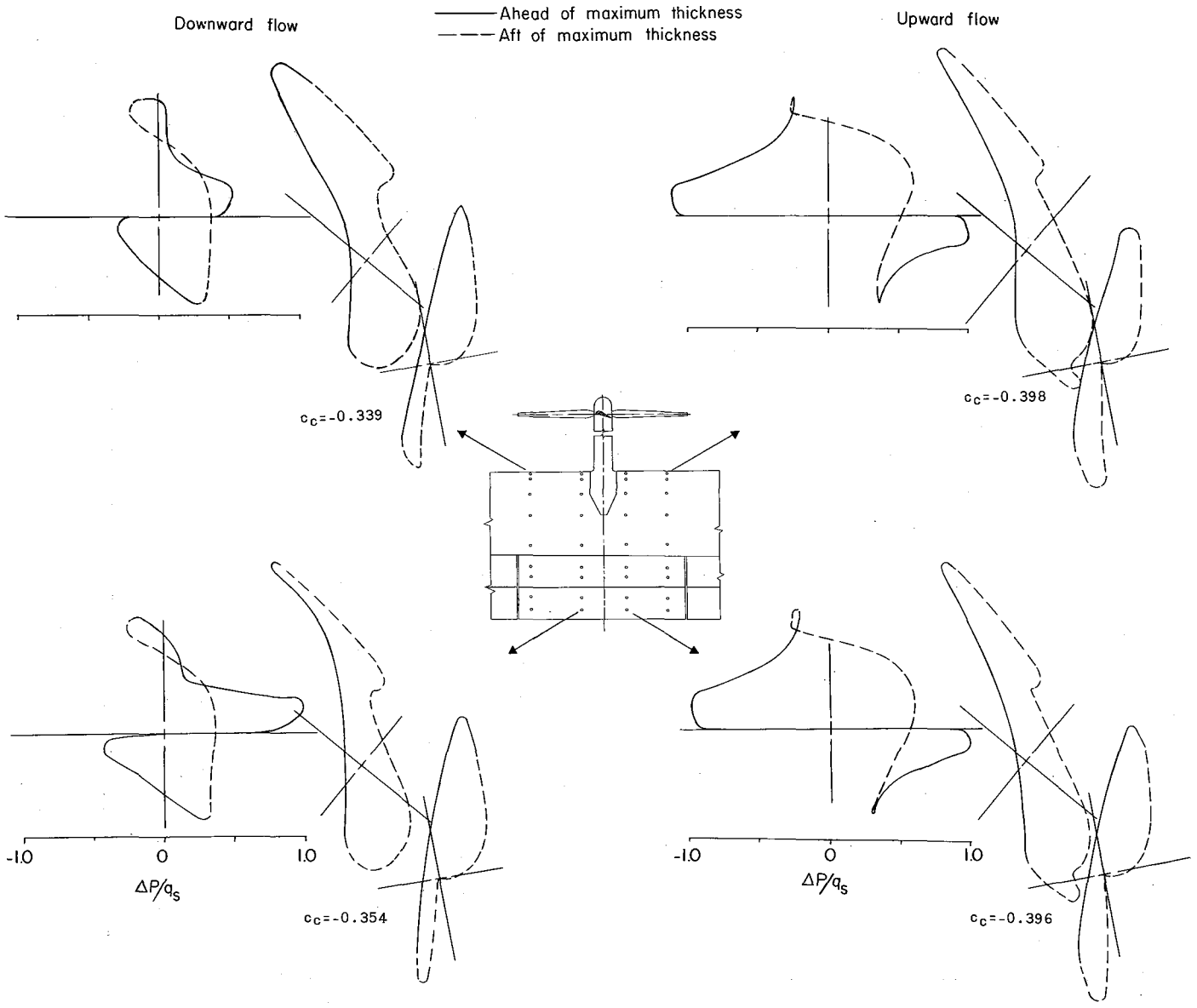

(b) Chord pressure distributions over airfoil thickness.

Figure 21.- Concluded.

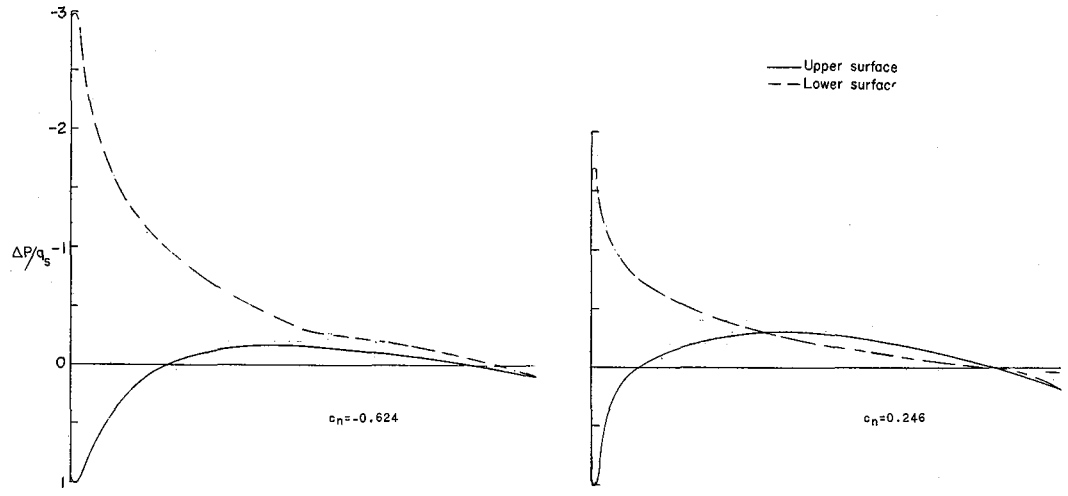

(a) $\alpha = -8.5^{\circ}$.

(b) $\alpha = -4.5^{\circ}$.

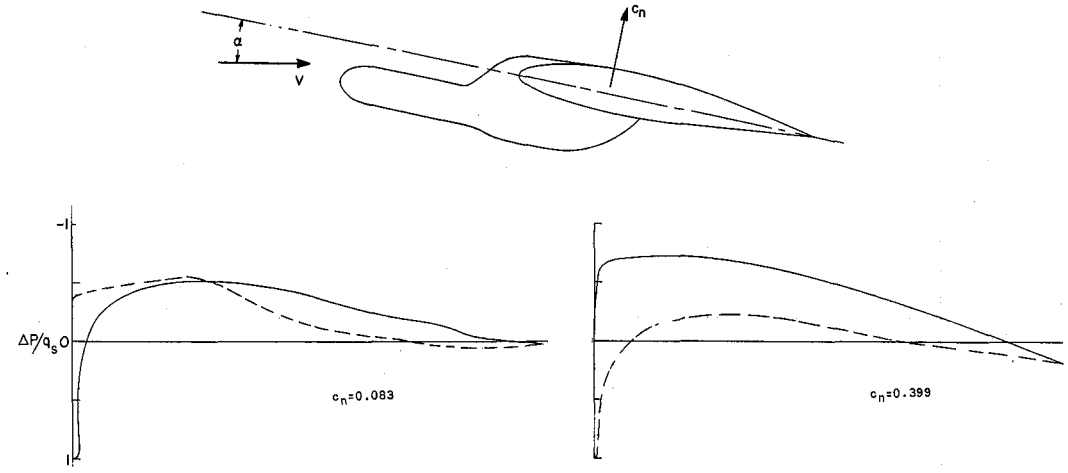

(c) $\alpha = -0.5^{\circ}$.

(d) $\alpha = 3.5^{\circ}$.

Figure 22.- Chordwise pressure distributions in uniform flow on wing without propellers and with flaps neutral.

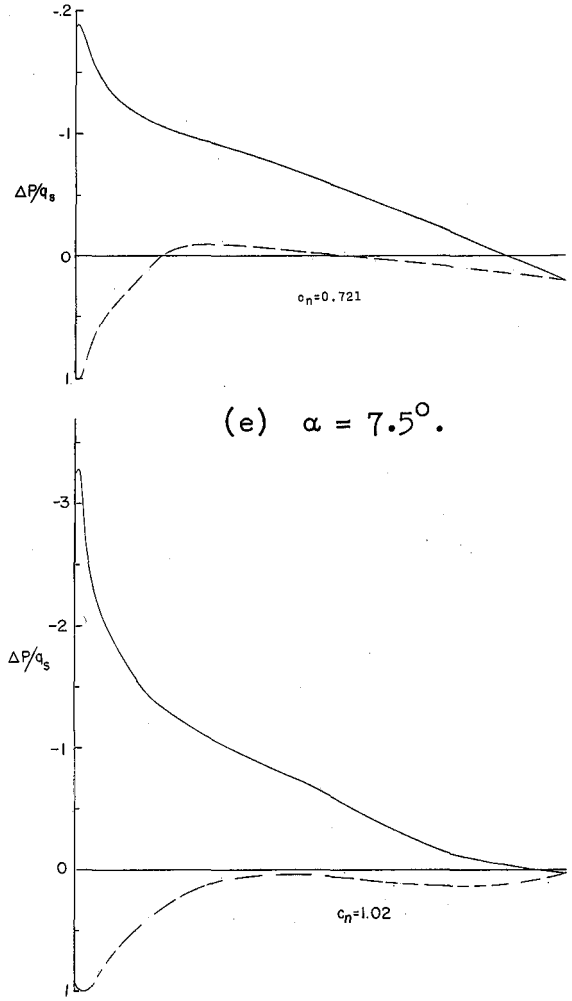

(e) $\alpha = 7.5^{\circ}$.

(f) $\alpha = 11.5^{\circ}$.

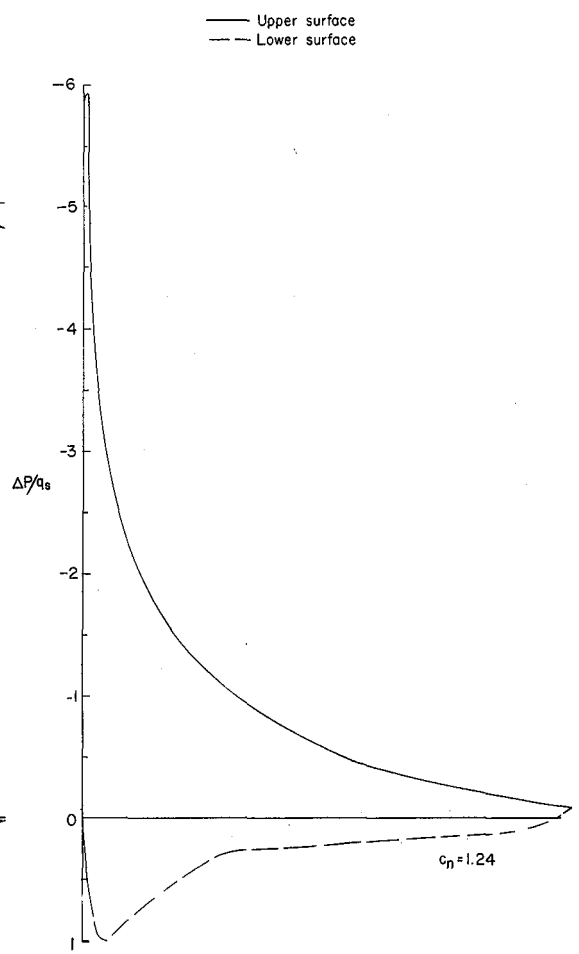

(g) $\alpha = 15.5^{\circ}$.

Figure 22.- Continued.

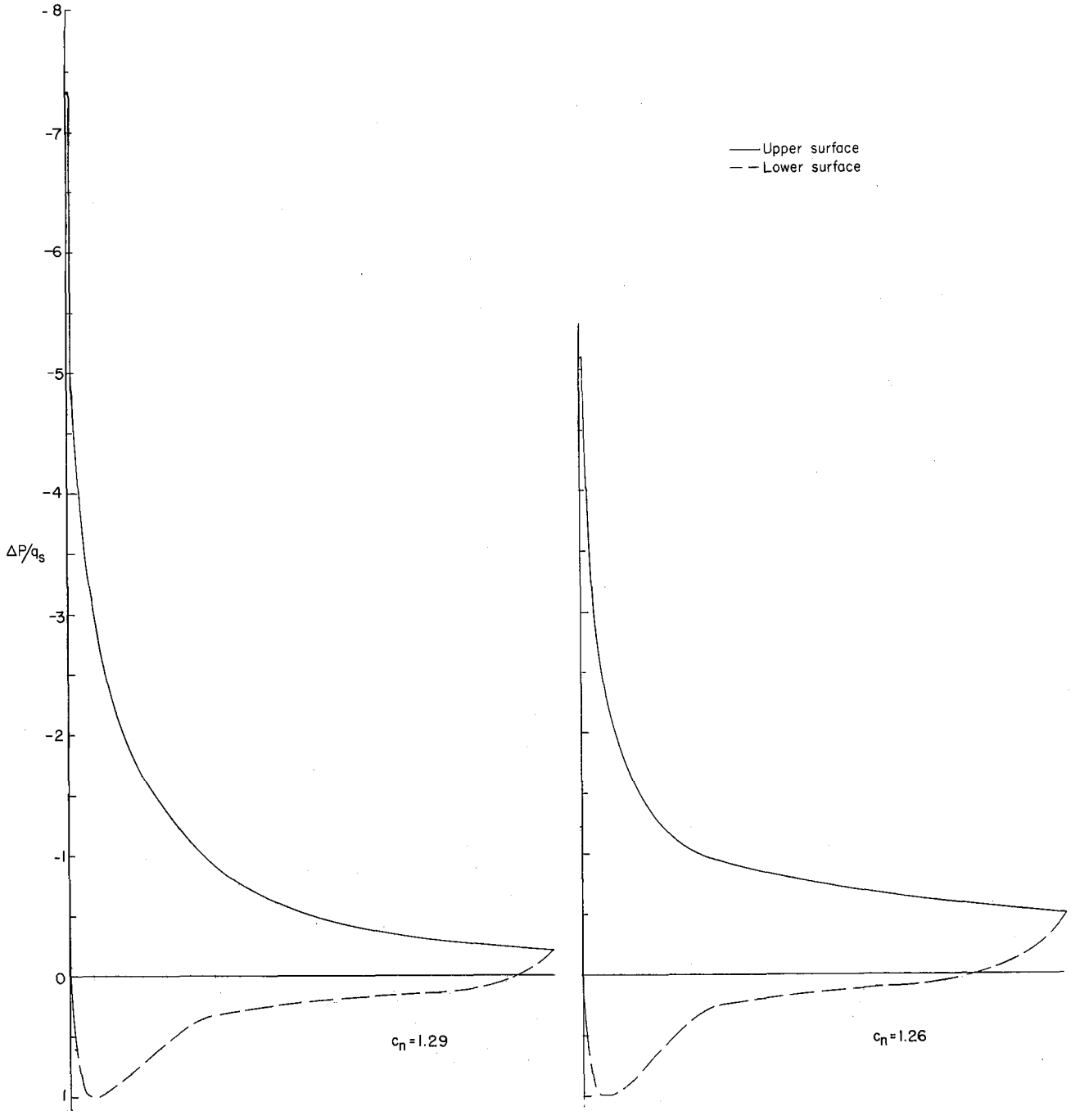

(h) $\alpha = 17.5^{\circ}$.

(i) $\alpha = 19.5^{\circ}$.

Figure 22.- Concluded.

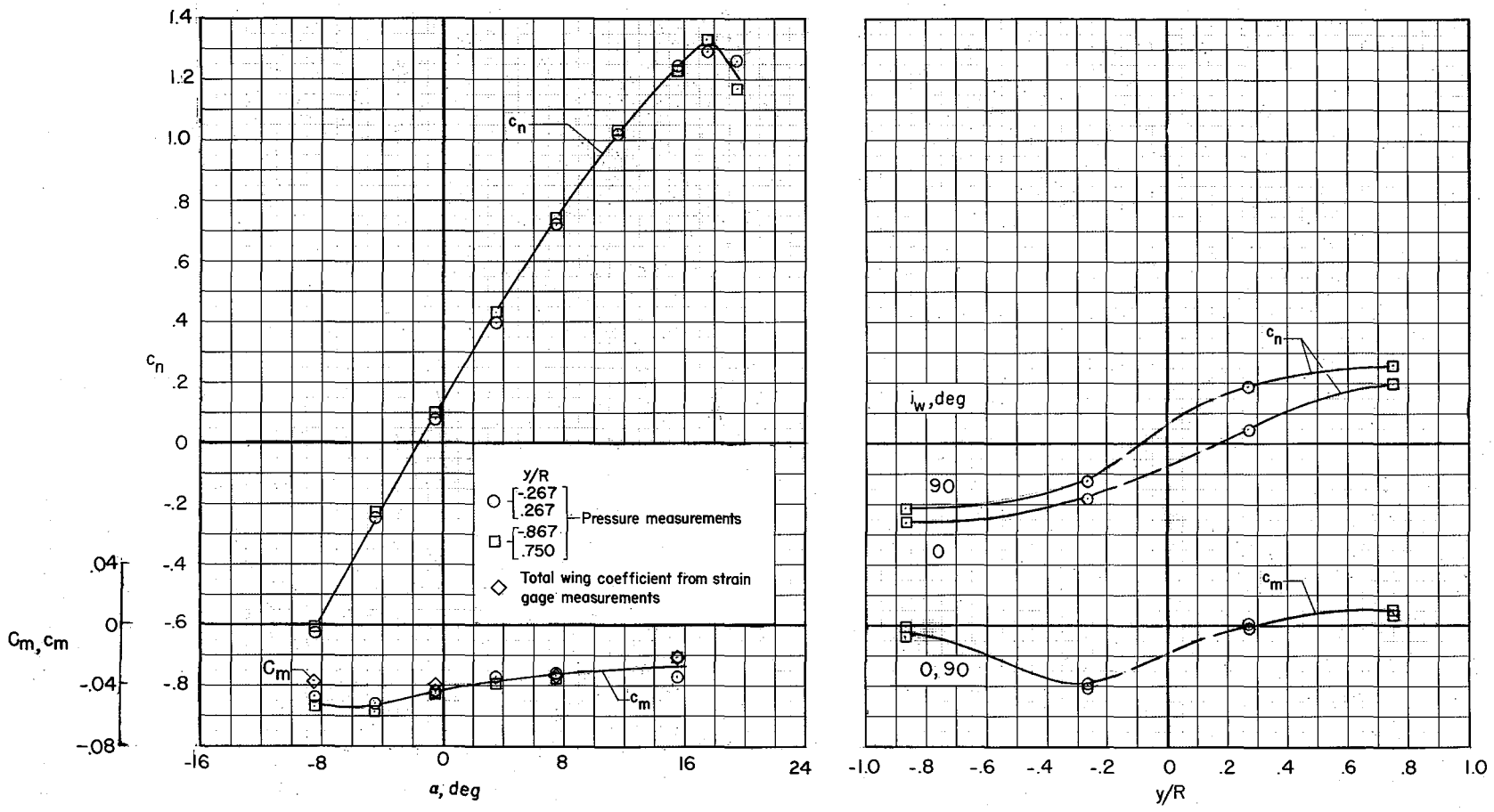

(a) Wing section characteristics in uniform flow for wing without propellers.

(b) Spanwise variations behind propellers in slipstream for wing at static thrust. z/D = 2.4.

Figure 23.- Section-normal-force and moment variations for wing with flaps neutral.

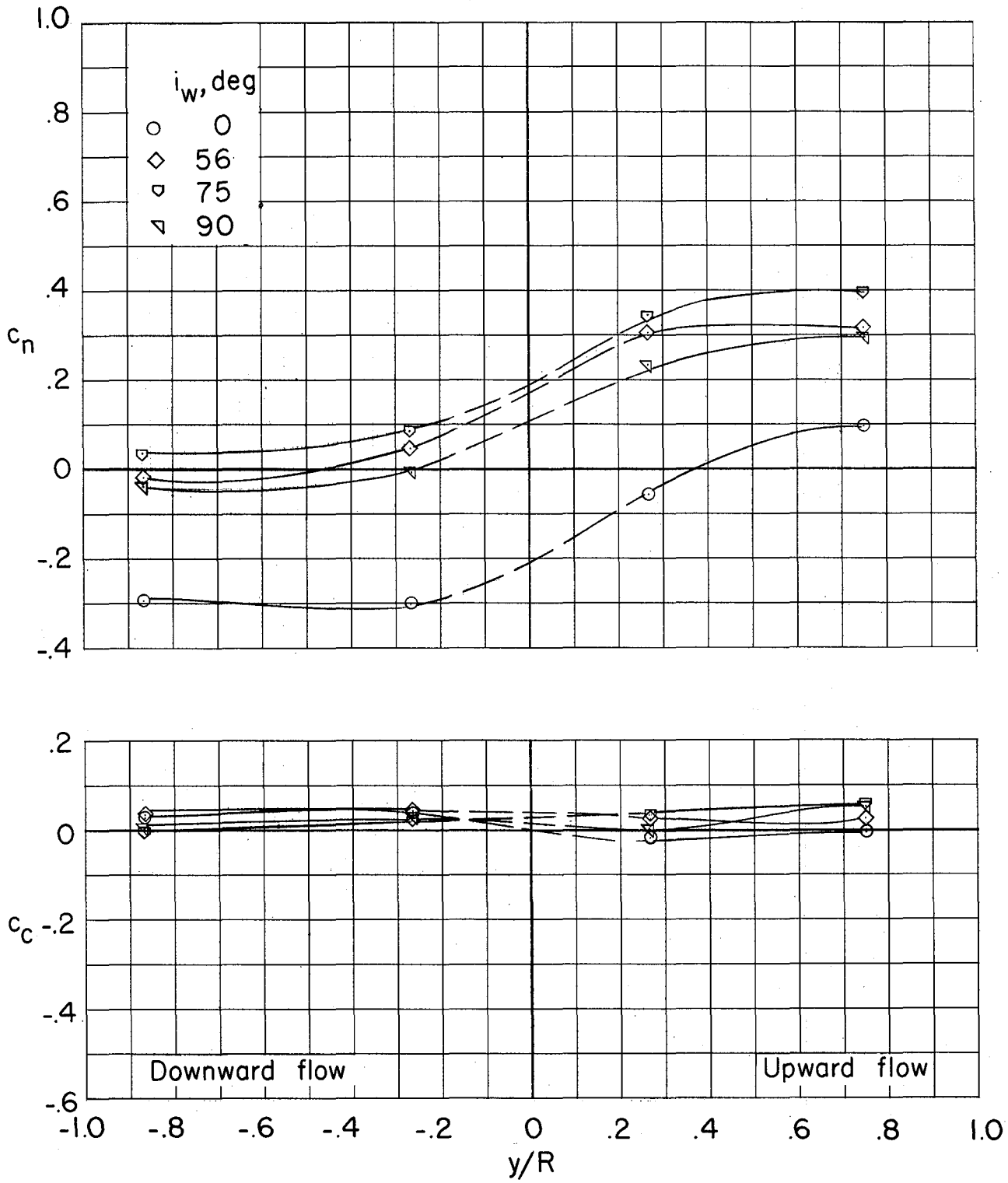

(a) z/D = 1.0.

Figure 24.- Spanwise-force variations with flaps neutral.

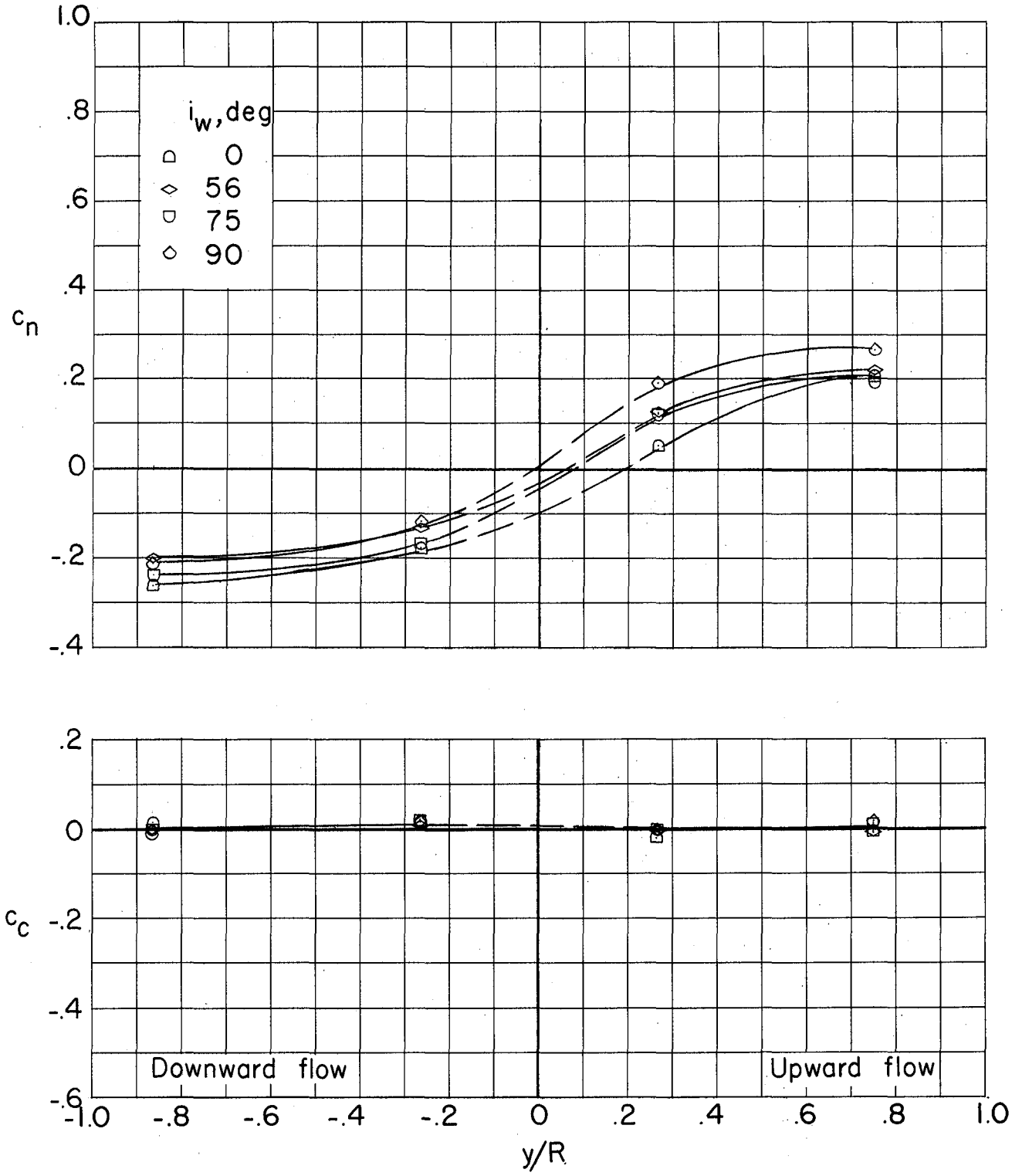

(b) z/D = 2.4.

Figure 24.- Concluded.

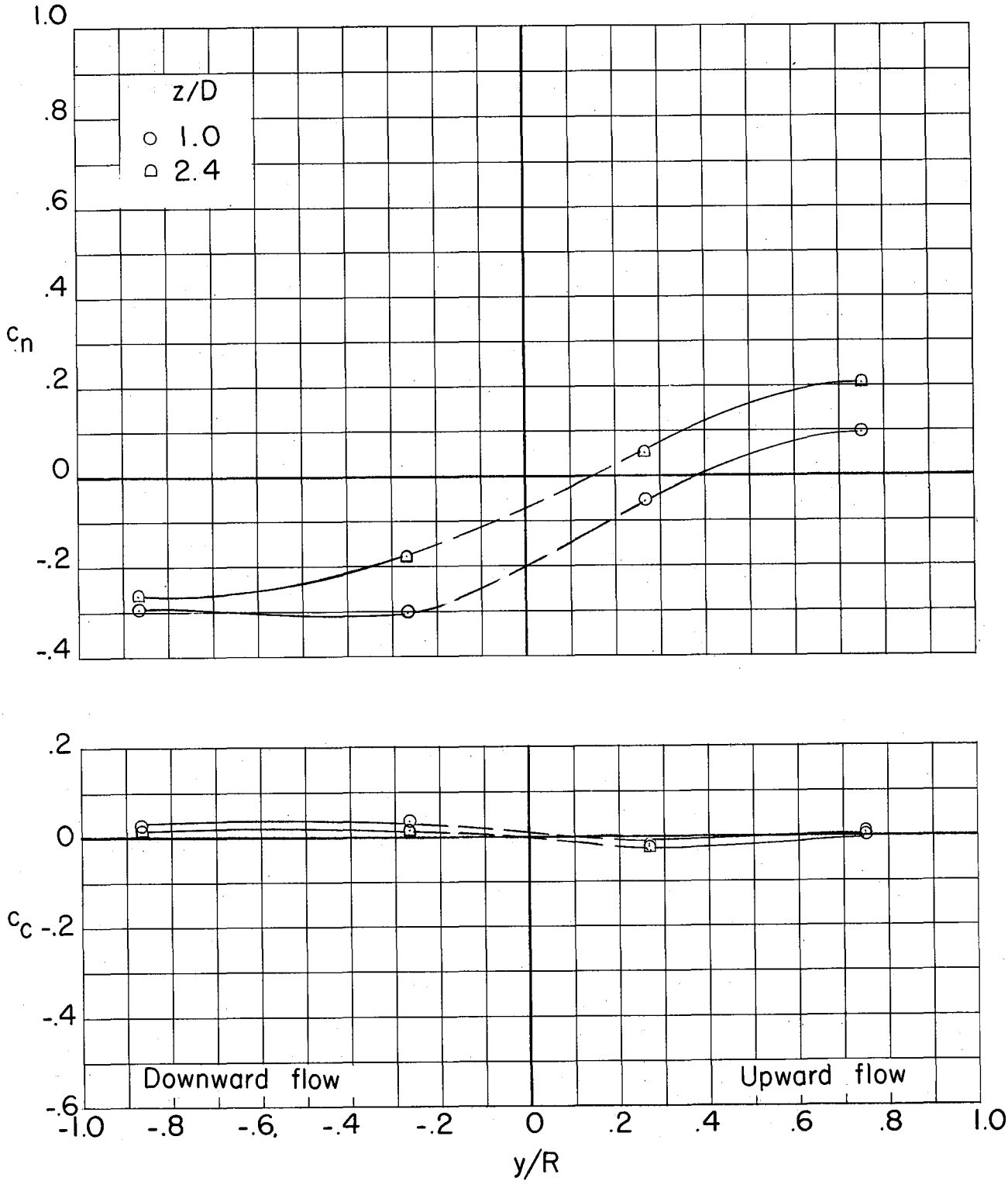

(a) $i_w = 0^\circ$.

Figure 25.- Spanwise-force variations with flaps neutral.

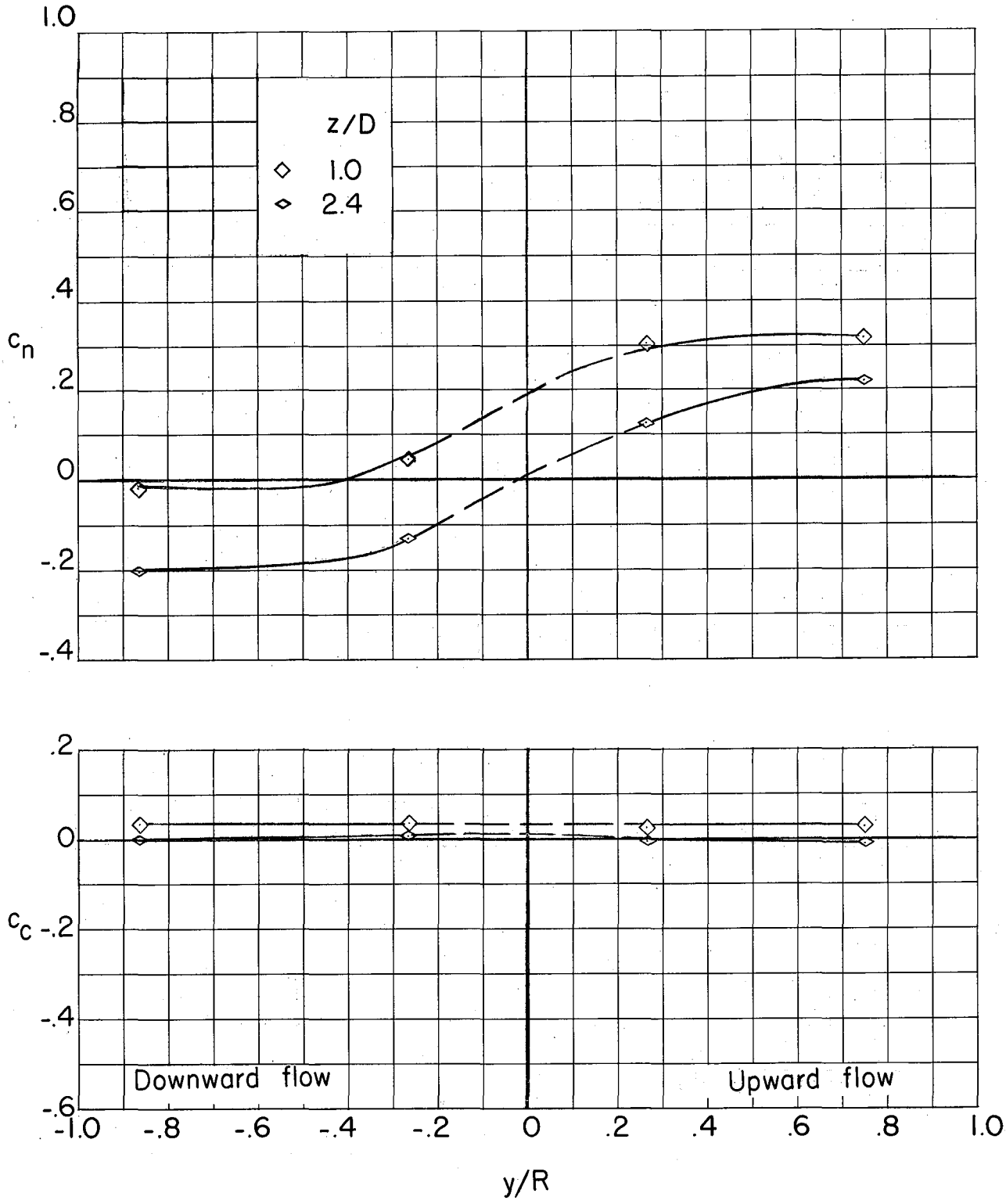

(b) $i_w = 56^\circ$.

Figure 25.- Continued.

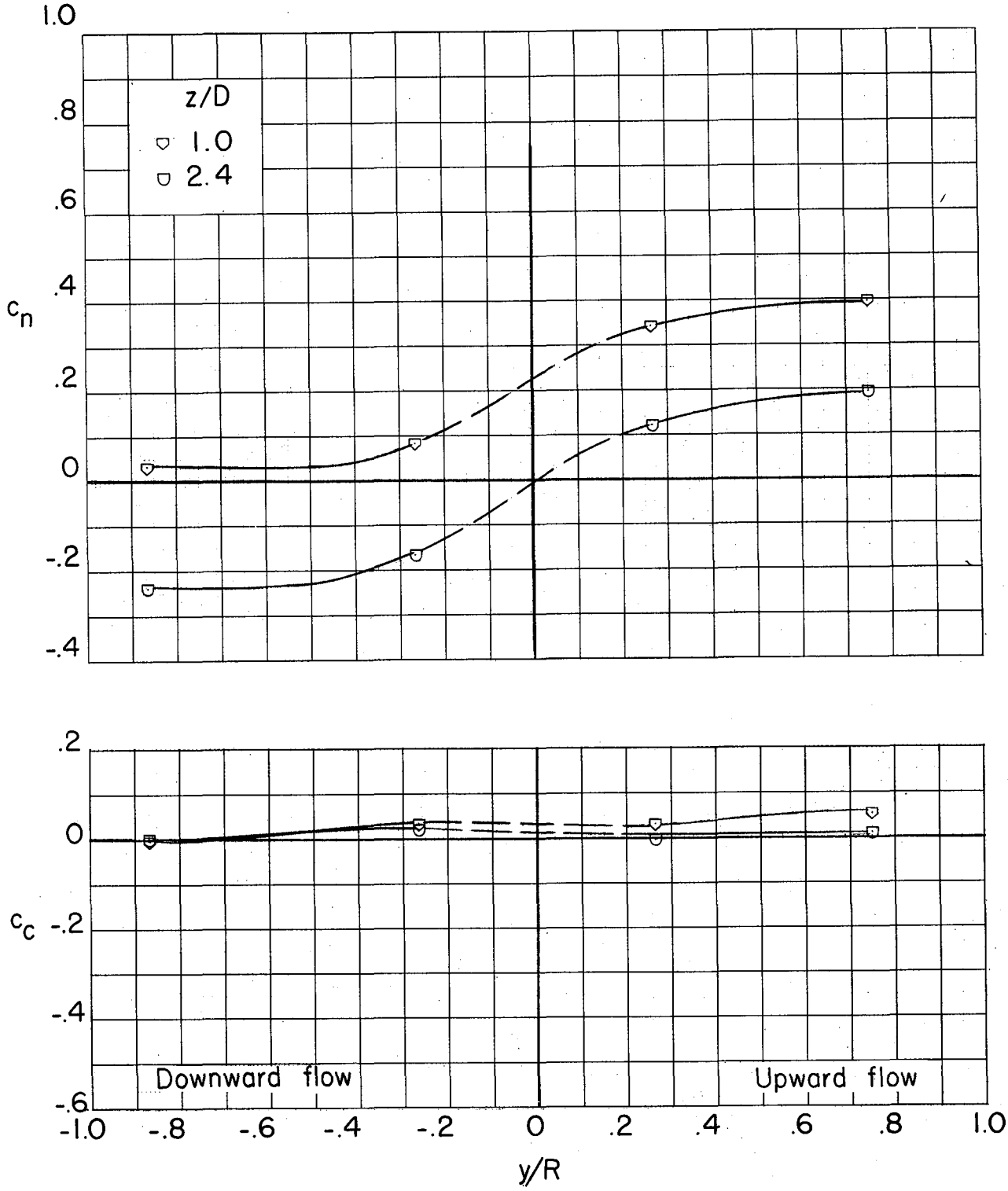

(c) $i_w = 75°$.

Figure 25.- Continued.

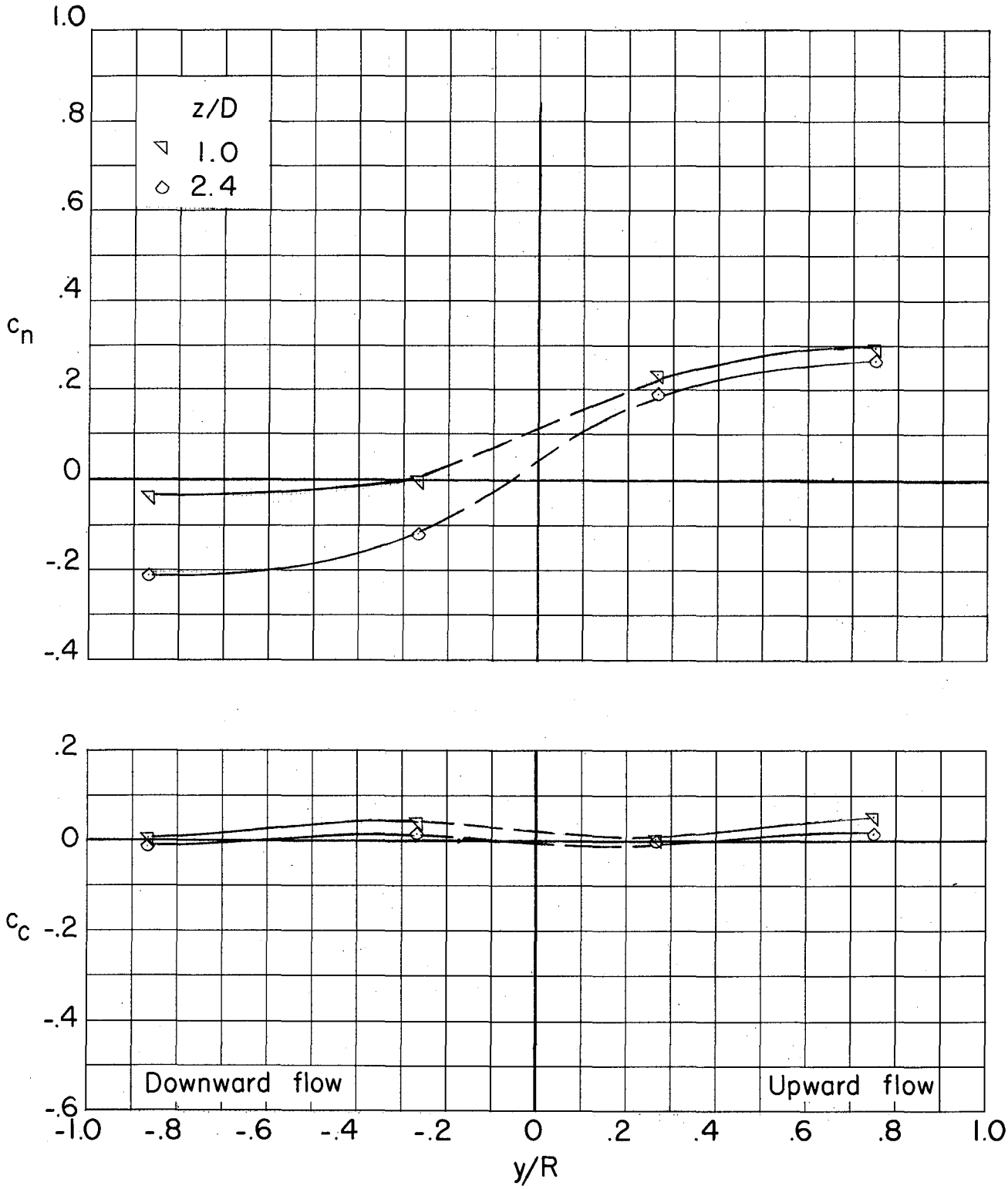

(d) $i_w = 90°$.

Figure 25.- Concluded.

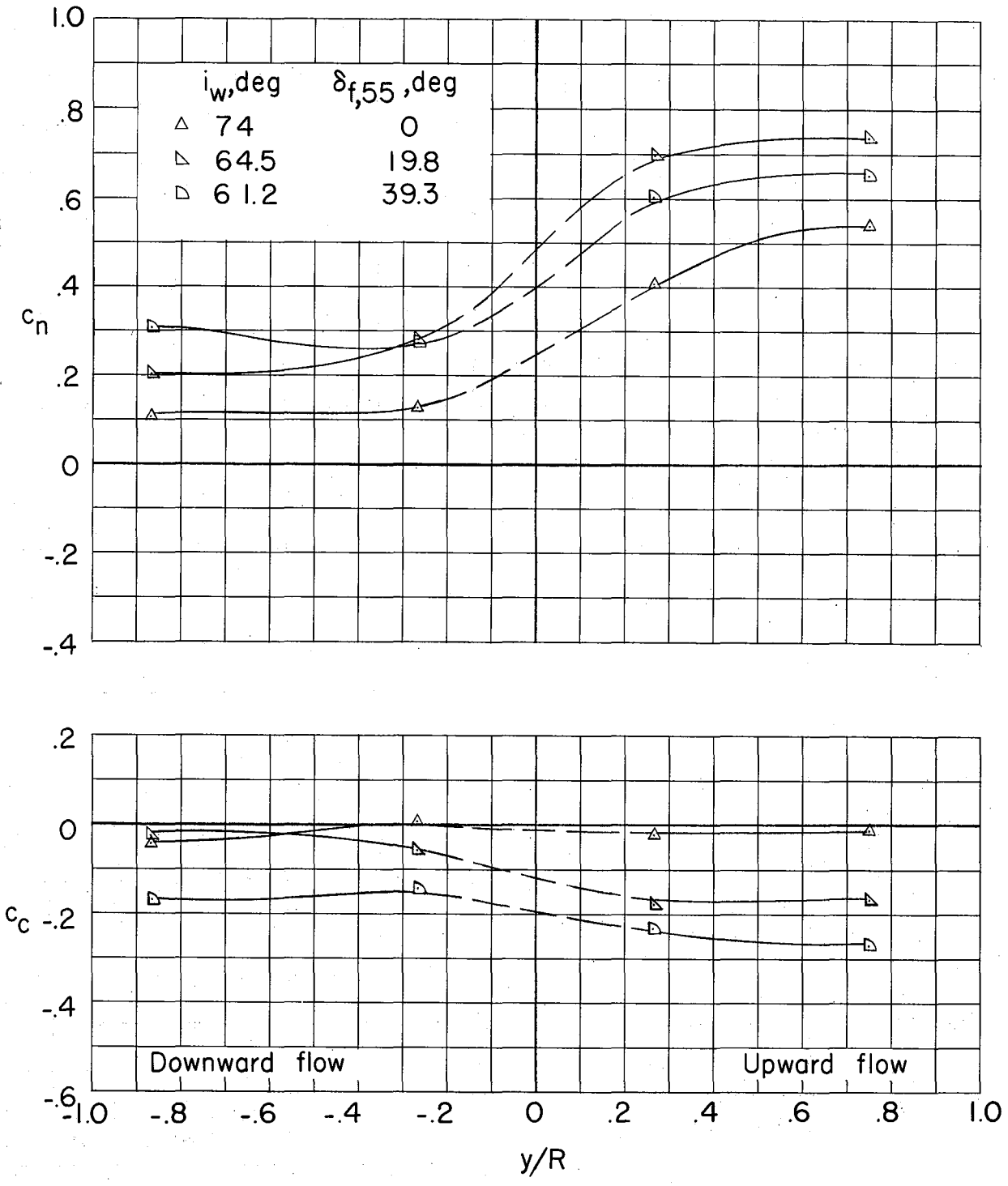

(a) z/D = 1.0.

Figure 26.- Spanwise-force variations for configurations having vertical resultant force and varying i_w and $\delta_{f,55}$. $\delta_{f,30} = 38.6°$.

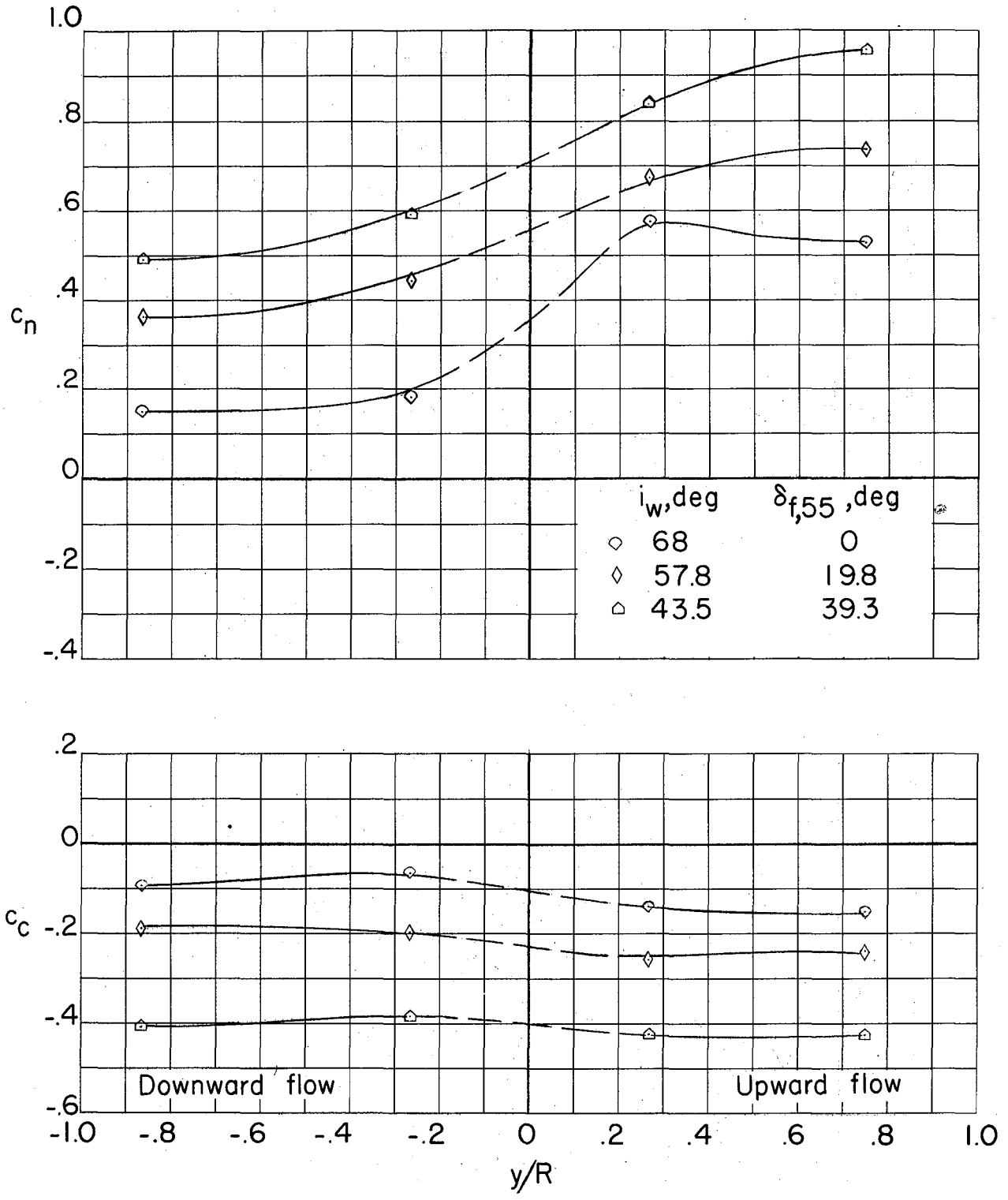

(b) z/D = 2.4.

Figure 26.- Concluded.

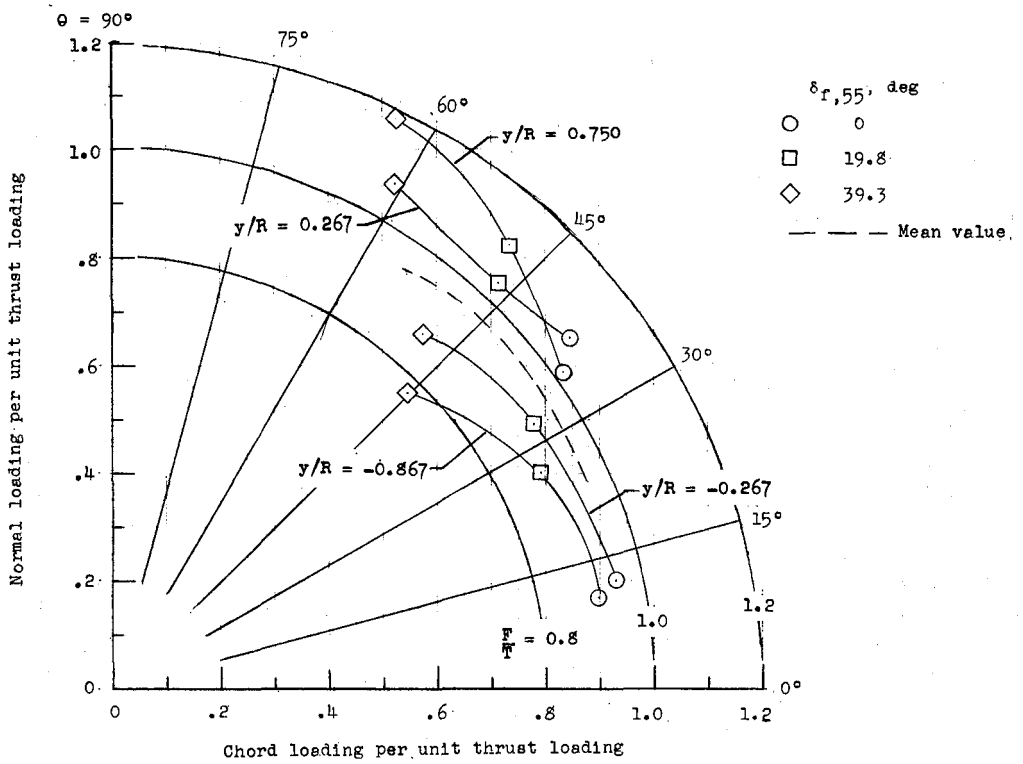

(a) z/D = 2.4.

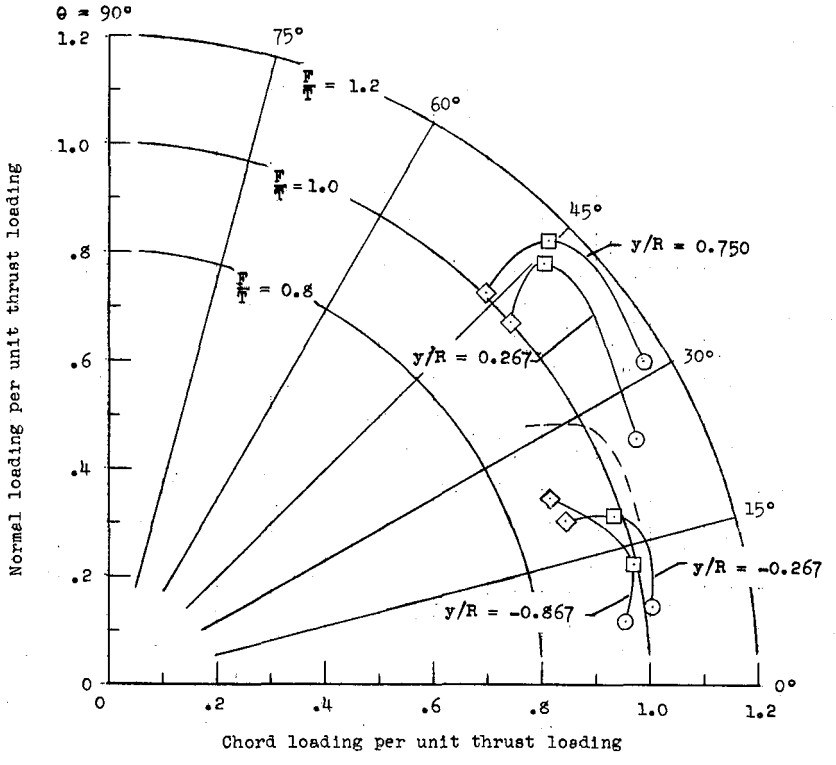

(b) z/D = 1.0.

Figure 27.- Summary of turning effectiveness of wing section behind propeller. $\delta_{f,30} = 38.6^{\circ}$; $\theta + i_w = 90^{\circ}$.

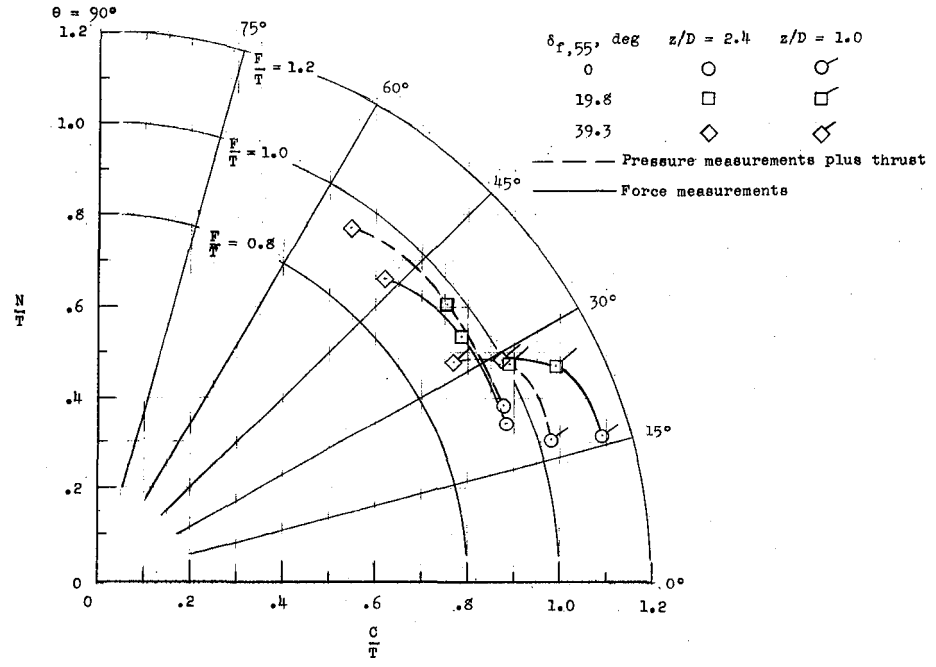

Figure 28.- Summary of turning effectiveness of wing section behind propeller. $\delta_{f,30} = 38.6^{\circ}$; $\theta + i_w = 90^{\circ}$.

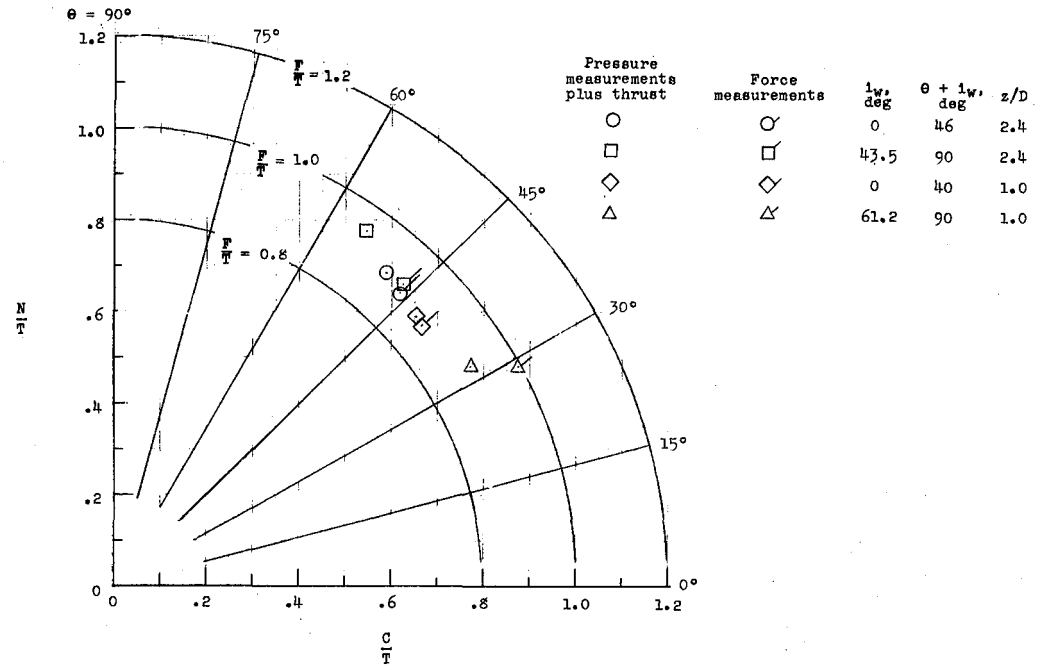

Figure 29.- Summary of turning effectiveness of wing section behind propeller. $\delta_{f,55} = 39.3^{\circ}$; $\delta_{f,30} = 38.6^{\circ}$.